High Range Resolution Profile Alignment

Prepared by:

Vanessa Janse van Rensburg

JNSVAN001

Supervised by:

Dr. Amit Mishra
Department of Electrical Engineering
University of Cape Town

Willie Nel
Radar and Electronic Warfare Systems
CSIR, DPSS

September 2012

A dissertation submitted to the Department of Electrical Engineering,

University of Cape Town,

in partial fulfilment of the requirements for the degree of

Master of Engineering specialising in *Radar and Electronic Defence*.

Declaration

1. I know that plagiarism is wrong. Plagiarism is to use another's work and pretend that it is one's own.
2. I have used the IEEE convention for citation and referencing. Each contribution to, and quotation in, this project report from the work(s) of other people, has been attributed and has been cited and referenced.
3. This project report is my own work.
4. I have not allowed, and will not allow, anyone to copy my work with the intention of passing it off as their own work or part thereof.

Signature of Author .....

Pretoria
26 September 2012

Terms of Reference

The report produced at the end of the project must meet the following requirements:

1. The introductory chapters must create a logical background to highlight the need for range bin alignment
2. The literature survey must include historic and state of the art range bin alignment techniques from reputable sources
3. Discussions and MATLAB® implementations to show understanding of the range bin alignment techniques
4. Quality measures used in range bin alignment must be identified and understood
5. Effects that cause difficulty in range bin alignment must be identified
6. A sensitivity analysis of quality measures to problematic effects must be conducted
7. Sensible conclusions and recommendations for future work finishes the report

Acknowledgements

Firstly, I have to express my gratitude to my employer, the Council for Scientific and Industrial Research (CSIR) for funding the project and providing the facilities needed to complete the research, particularly the use of the MecORT X-band tracking radar testing facility.

The radar data presented in this report is the property of Armaments Corporation of South Africa SOC Ltd (ARMSCOR), who provided permission for the release of the information contained in the project report document [1], without which this work could not have been completed.

Finally, many thanks to my study leaders, Dr. Amit Mishra from the University of Cape Town and Willie Nel from DPSS, REW. Your guidance and support throughout the project is much appreciated.

Abstract

Range bin alignment forms the first step in non-parametric motion compensation for ISAR imaging. Non-parametric techniques have fewer limitations to parametric techniques, which require that the assumption of a signal model is valid. Various range bin alignment algorithms have been developed. The success, or alignment quality, of these algorithms are typically estimated by visual examination of the aligned result.

Measures for quantifying the alignment quality achieved provide a means of comparing performances of different algorithms on a particular data set. Several such measures have been identified. Characteristics in the data, such as target vibration effects, may cause degradation of the quality measures. Common effects found in radar data that could cause quality degradation were simulated. The quality results were analysed to identify trends and sensitivities in the use of quality measures.

The evaluation of existing range bin alignment techniques has led to identifying a set of important design considerations for range bin alignment algorithms.

Contents

List of Figures

List of Tables

List of Symbols

Listed in order of appearance.

ΔR_{rc}	-	Cross range resolution
c	-	Speed of light
f_o	-	Radar operating frequency
Ω_{eff}	-	Modulus of effective rotation vector of the target
T_{obs}	-	Observation time
Y_R	-	Ideal received signal of a single scatterer in free space
$\mathbf{S}$	-	Sum envelope
H	-	Total sum envelope entropy
$p(m,n)$	-	Sample in the n$^{\text{th}}$ range bin of the m$^{\text{th}}$ profile
$\mathbf{P}_m$	-	m$^{\text{th}}$ profile
$\mathbf{R}_m$	-	m$^{\text{th}}$ reference profile
$\mathbf{X}_m$	-	Correlation of the m$^{\text{th}}$ profile envelope
τ_m	-	Range bin shift applied to the m$^{\text{th}}$ profile
$\hat{\mathbf{P}}_m$	-	m$^{\text{th}}$ aligned profile
W_m	-	Weighting applied to the m$^{\text{th}}$ profile
κ	-	Exponential filter factor
γ_m	-	Filter gain applied to the m$^{\text{th}}$ profile
$\mathbf{H}_m$	-	Entropy of the m$^{\text{th}}$ sum envelope
$\bar{\hat{\mathbf{P}}}_{m-1}$	-	Average of all aligned profiles prior to the m$^{\text{th}}$ profile
$\hat{\tau}_m$	-	Optimal shift value for the m$^{\text{th}}$ profile
C	-	Total sum envelope contrast
G	-	Global envelope correlation

$\mathbf{X}(m,l)$	-	Envelope correlation of the m$^{\text{th}}$ and l$^{\text{th}}$ profiles
$\phi(m,l)$	-	Weighting used in the global envelope correlation calculation
$\nu[n_p]$	-	Peak location variance
D	-	Total mean squared envelope difference
B	-	Total burst derivative
A_v	-	Simulated vibration amplitude
τ_v	-	Simulated vibration period
σ_x	-	Gaussian noise variance
W_L	-	Window length when using non-coherent averaging of profiles

List of Abbreviations and Acronyms

AWT	Adaptive Wavelet Transform
BRF	Burst Repetition Frequency
CE	Computationally Expensive
CPI	Coherent Processing Interval
CSIR	Council for Scientific and Industrial Research
DPN	Degraded Performance with Noise and clutter
DPPTV	Degraded Performance with Platform/Target Vibration
DPSS	Defence, Peace, Safety and Security
EA	Error Accumulation
FFT	Fast Fourier Transform
FIR	Finite Impulse Response
FM	Frequency Modulation
HRR	High Range Resolution
ICBA	Image Contrast Based Autofocus
IEBA	Image Entropy Based Autofocus
IFFT	Inverse Fast Fourier Transform
IFT	Inverse Fourier Transform
IRBS	Integer Range Bin Shifts
ISAR	Inverse Synthetic Aperture Radar
LTM	Limited Target Manoeuvrability
NCTR	Non-Cooperative Target Recognition

pdf	probability density function
PRI	Pulse Repetition Interval
RCS	Radar Cross Section
REW	Radar and Electronic Warfare
SAR	Synthetic Aperture Radar
SFE	Scatterer Fluctuation Effects
SNR	Signal to Noise Ratio
SRP	Synthetic Range Profile

Nomenclature

Aspect angle— The angle between the radar line of sight and the longitudinal axis of a target.

Azimuth—Angle in a horizontal plane, relative to a fixed reference, usually north or the longitudinal reference axis of the aircraft or satellite.

Bandwidth— The frequency interval occupied by a signal or passed by a filter or other device. The conventional symbol is B. Several different bandwidths have been defined and used in the literature of radar waveforms and signal processing. From Barton [2].

Beamwidth—The angular width of a slice through the main lobe of the radiation pattern of an antenna in the horizontal, vertical or other plane.

Doppler frequency—A shift in the radio frequency of the return from a target or other object as a result of the object's radial motion relative to the radar.

PRF—Pulse repetition frequency.

Radar Image—The spatial distribution of the scattering sources of an object, obtained as a result of analysis of the electromagnetic field scattered by it. From Barton [2].

Range—The radial distance from a radar to a target.

Range-Doppler image— Two-dimensional radar image of a target that characterizes the distribution of amplitude or RCS in range and Doppler coordinates. From Barton [2].

Synthetic Aperture Radar (SAR)—A signal-processing technique for improving the azimuth resolution beyond the beamwidth of the physical antenna actually used in the radar system. This is done by synthesizing the equivalent of a very long sidelooking array antenna.

Chapter 1

Introduction

1.1 Background to the study

Radar imaging techniques, including Inverse Synthetic Aperture Radar (ISAR) processing have received much attention in recent years. A well-focussed ISAR image provides the ability to extract features from a target of interest for classification and identification. It is important to note that the "cooperativity" of a target, in this context, refers to the knowledge available to the radar operator regarding the target's exact location, class and mission during the observation time. For non-cooperative target recognition, the exact motion of the target is hidden from the processor and needs to be extracted from the radar data in order to create a focussed ISAR image. The translational motion extraction and compensation are performed by parametric or non-parametric techniques. Most non-parametric techniques use two steps, namely range bin alignment and phase conjugation in order to produce a focussed ISAR image.

Many techniques have been implemented to achieve adequate range bin alignment. The performance of the techniques are heavily influenced by the type of target and its movement during illumination, as well as the presence of noise and clutter. Different techniques may provide varying results when applied to the same data, which may indicate that certain techniques are more suited for

alignment of particular data types. Similarly, figures of merit for range bin alignment techniques may be sensitive to data anomalies to varying degrees, yielding suboptimal quantification of the alignment performance of an algorithm.

1.2 Objectives of this study

The objective of this study was to *study*, *implement* and *critically evaluate* range alignment techniques in order to identify shortcomings and to suggest ways of i) improving the results or ii) avoiding common errors found in existing range bin alignment techniques. Methods for quantifying the quality of range bin alignment achieved had to be identified, while taking into account the sensitivity of the quality measures to various anomalies in the data.

Using the knowledge and understanding of range bin alignment algorithm structures, suitable quality measures and related sensitivities, a framework can be suggested for the design of a range bin alignment algorithm tailored to a specific application to achieve the best possible range bin alignment.

1.2.1 Initial investigation

The initial investigation describes the context of the work and includes answering the following questions:

1. What is the purpose of range bin alignment?
2. What types of range bin alignment algorithms exist, what are their differences and how can they be improved?

1.2.2 Problems to be investigated

The problems investigated in this project include:

1. How can the performance of a range bin alignment algorithm be measured?
2. How accurately do quality measures quantify the quality of range bin alignment when subject to interference caused by data anomalies?
3. What are the considerations involved when designing an optimal range bin alignment algorithm?

1.2.3 Purpose of the study

The purpose of the study is to implement and evaluate algorithms that perform accurate range alignment on high range resolution radar data. Such range alignment constitutes the first step in a non-parametric autofocussing technique for the purposes of ISAR imaging.

An analysis of quality measures for range bin alignment provides insight to standardise the measurement of quality in range bin alignment algorithms.

A framework for the considerations in range bin alignment algorithm summarises the findings of this project and can be used for algorithm analysis and design.

1.3 Scope and Limitations

The scope of this project includes the implementation of well-known range bin alignment techniques as presented in the literature, identification, implementation and analysing the sensitivity of quality measures for range bin alignment.

The sensitivity analysis is performed by simulating simplified models of the identified data anomalies. Detailed modelling of clutter, noise and target fluctuation effects are beyond the scope of this study.

Calculation of the cost functions and quality measures are limited to the envelopes, or magnitude of the profiles. Advanced topics such as complex correlation is beyond the scope of this study.

This dissertation is submitted in *partial fulfilment* of the requirements for the degree of Master of Engineering specialising in Radar and Electronic Defence. The time allocation for this project is limited to 60 credits, or 600 hours, which suggests it should be approximately one third of a traditional master's dissertation.

1.4 Project development plan and report layout

The project development can be inferred by considering the report layout. The report is organised as follows:

Chapter 2: Context

Addresses in detail the need for range bin alignment. A brief background on high resolution radar is followed by an introduction to radar imaging, the techniques involved and applications of radar imaging. Motion compensation and autofocus techniques are introduced to highlight the need for range bin alignment. Finally, target feature extraction from high range resolution profiles is briefly discussed.

Chapter 3: Range Bin Alignment Techniques

This chapter includes the first part of the literature survey. Classical and state of the art range bin alignment algorithms are identified, implemented and discussed. Differences between the various techniques are identified. A summary provides the claimed advantages of each technique as found in the literature as well as an initial quality analysis.

Chapter 4: Quality Measures for Range Bin Alignment

In the analysis of various range bin alignment techniques, a figure of merit is required to identify superior techniques based on quantitative results. This chapter identifies measures that can be used to quantify the accuracy or quality of range bin alignment on aligned data. It forms the second part of the literature survey.

Chapter 5: Alignment and Alignment Quality of Measured data

This chapter presents the application of the alignment techniques presented in Chapter 3 to measured data of slow and high speed targets. The quality measures calculated for each aligned result is discussed and characterised.

Chapter 6: Sensitivity Analysis and Recommendations for Quality Measures

The quality measures introduced in Chapter 4 may produce false results when the measure is affected by anomalies in the data that are not related to the alignment quality. This chapter investigates trends that occur in the quality measures when simulated data is corrupted by varying levels of anomalous effects, particularly effects caused by the target (rotation, vibration, fluctuation, etc.) and effects caused by the environment (noise, clutter, etc.).

Chapter 7: Mitigation of range bin alignment errors caused by algorithm parameters

Some errors found in the results produced by the range bin alignment algorithms identified in Chapter 3 are consequences of limitations on the algorithm. These limitations improve the computational efficiency and complexity of the algorithms, with decreased range bin alignment capabilities. This chapter identifies ways of mitigating these range bin alignment errors.

Chapter 8: Conclusions

Considering all the factors above, considerations are presented on how a range bin alignment algorithm may be designed to achieve optimal alignment of a data set with particular characteristics.

Chapter 2

Context

This chapter discusses the context of range bin alignment, namely radar imaging and target feature extraction.

Different types of radar imaging techniques exist, each with unique processing steps, limitations and requirements. Some relevant processing steps appear in Figure 2.1.

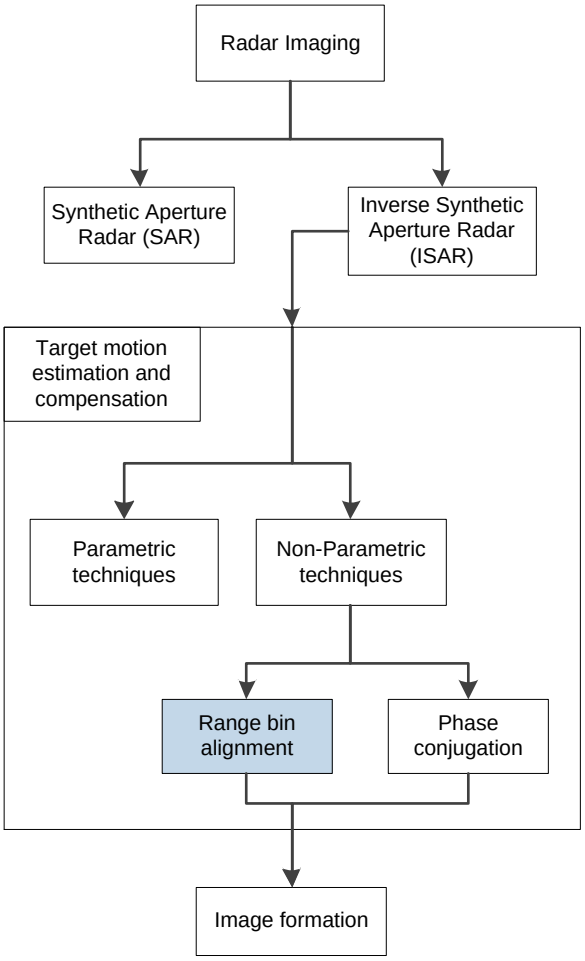

Figure 2.1: Contextual flow diagram of the processing steps in radar imaging. The flow diagram highlights the main topic of this study, namely the *Range Bin Alignment* step.

The research presented in this report focuses on the range bin alignment step (translational motion compensation).

2.1 High Resolution Radar

Advances in the development of radars that operate at higher centre frequencies with increased bandwidth, while maintaining phase stability have created

a specialised group of radar applications, namely *High Resolution Radar*. The resolution of a radar contain a) *range resolution* and b) *angular resolution*.

Range resolution defines the minimum radial distance between two targets that are simultaneously illuminated by a radar that would result in data where the targets can be resolved in range. For high resolution radar, the range resolution is considered to be in the magnitude order of one meter or less.

Popular waveforms used for high resolution radar imaging applications include (depicted in [3]):

- Short pulse
- Linear FM pulse
- Stepped frequency waveform

A *stepped frequency waveform* was used in the measurements presented in this study. The stepped frequency waveform consists of a train, or *burst* of pulses, each at a centre frequency increased by a predetermined step size. The bandwidth of the resulting signal is increased by the inclusion of the pulses at various frequencies and can be calculated as the product of the number of pulses per burst and the frequency step size. The number of pulses in a burst determines the number of range cells per profile. The increase in bandwidth results in an improvement of the achievable down range resolution.

The azimuth resolution of a radar imaging system can also be termed the *cross range resolution* of the system. A fine cross range resolution is achieved by *synthesizing* a large antenna with a narrow beamwidth by suitably processing multiple measurements made by a small antenna with a wider beamwidth. This forms the basic principle of *Synthetic Aperture Radar*. Due to the improvement in angular and down range resolution, high resolution range profiles can be formed, as shown in Figure 2.2.

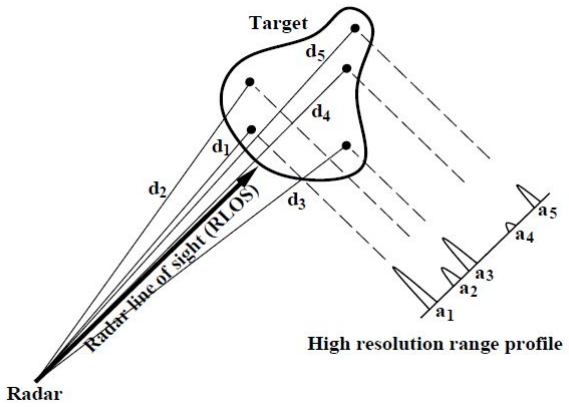

Figure 2.2: Figure indicating the formation principle of a high resolution profile. The return signals from scatterers on the target are depicted by d_x and the corresponding peaks in the range profile are presented by a_x. This image was taken from Zyweck [4].

The measurements used in this study were obtained using the MecORT measurement facility at the Council for Scientific and Industrial Research (CSIR). MecORT is a pencil beam tracking radar that operates at X-band. The data is presented in [1] and used in this study with permission from the owner.

2.2 Radar Imaging

One goal of radar imaging is to create a picture of an area or *object* (referred to the *target*) that highlights distinctive physical features of the target, or is recognisable when compared to an optical photograph of the target. Various differences exist between an optical image and an image generated using radar technology. Radar imaging has advantages over optical and infrared remote imaging sensors due to its all-weather, day or night and long range imaging capability.

Carl Wiley of the Goodyear Aircraft Corporation was the first person who stated, in June 1951, that the Doppler frequency in the backscattered signal from a target could be used to obtain fine cross range resolution for radar imaging [5]. He

argued that if a relative speed exists between the radar and target, each component of the target would have a slightly different speed relative to the antenna. Precise analysis of the Doppler frequency (velocity) of the reflections through the use of the Fourier Transform, modern spectral estimation or time-frequency representations [6] will allow for the construction of a detailed image of the target. This is the fundamental principle of coherent radar imaging, specifically Synthetic Aperture Radar (SAR) and Inverse SAR (ISAR), which provide significant benefits over non-coherent imaging such as amplitude-only tomography.

2.2.1 SAR

Synthetic Aperture Radar (SAR) imaging was initially developed as a military reconnaissance tool. The operational concept of SAR involves a radar, fixed on a moving, often airborne, platform with the antenna beam illuminating the surface of interest during a flight path. Data is gathered and processed to obtain a focussed SAR image of the terrain. An example of a SAR image of a section of farmland is shown in Figure 2.3.

The first fully focussed SAR map was produced in August 1957 by a U.S. Army summer study started in 1953 and was codenamed "Project Wolverine" [5]. Since then, SAR has been used in a wide array of military, scientific and industrial applications. Some applications of SAR include [5]:

- Military reconnaissance
- Imaging of landscapes and terrain mapping
- Detection of subsurface geological structures
- Oceanography
- Ice studies of polar regions

Two common SAR techniques exist, namely *side-looking* or *stripmap* SAR and *spotlight* SAR. Stripmap SAR images is obtained when the platform is moving

Figure 2.3: Example of a SAR image of farmland, generated with a resolution of one foot. Taken from Stimson [7].

in a straight line, and spotlight SAR when the platform is moving in a circular pattern, focussing the radar beam on a 'spot' of the terrain.

Another SAR mode exists, named *scan* SAR, which is typically used at high altitudes in order to obtain a swath width that is wider than the ambiguous range [8]. The basic processing principle remains similar for all the techniques.

2.2.2 ISAR

ISAR processing can be considered as SAR processing where the radar remains stationary and the target is in motion. An example of an optical and ISAR image of a sailing yacht appears in Figure 2.4.

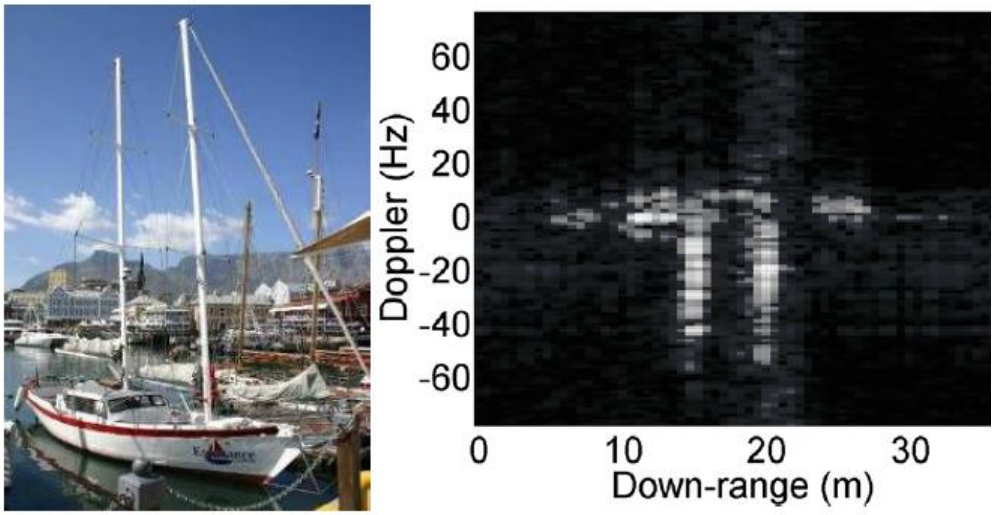

Figure 2.4: Photograph (left) and ISAR image (right) of a sailing yacht. From Anderson [9].

Although similar/reciprocal in concept, one major difference exists between SAR and ISAR. This difference relates to the *cooperativity* of the target. In this context, the target cooperativity is determined by the level of detail available regarding the *exact* translational and rotational motion of the target during the illumination time. In a controlled ISAR turntable experiment, the target motion parameters can be known in great detail. The importance of the exact knowledge of the target's motion is due to the fact that the target translational motion causes blurring in the ISAR image.

In practice, however, the target's translational movement can be acquired by tracking, often with variable accuracy, and the target's rotational information can be acquired from sensors on the target, such as accelerometers. For Non-cooperative Target Recognition (NCTR) the latter is obviously not available. Another problem regarding the non-cooperativity of the target, specifically in maritime targets, is the target movement as a result from external factors, such as the roll an pitch caused by waves on the ocean surface.

The rotational movement of the target relative to the radar causes the formation

of a synthetic aperture which is used to form the radar image. Note that this is analogous to the apparent rotation of objects in SAR processing due to the relative movement between the platform and the target. Therefore, the effective aperture size, or more importantly, the cross range resolution is a function of the change in angle, or *rotation rate* of the target [10] during the processing time. This relationship is given by Equation 2.1 [11] .

$$\Delta R_{rc} = \frac{c}{2f_0\Omega_{eff}T_{obs}} \tag{2.1}$$

Where c is the wave propagation speed, f_0 is the radar operating frequency, T_{obs} is the observation time, or CPI and Ω_{eff} is the modulus of the effective rotation vector of the target. *Roll*, *pitch* and *yaw* form the main components of the rotation vector and thus influence the resulting ISAR image view as shown in Figure 2.5 from Ozdemir [8].

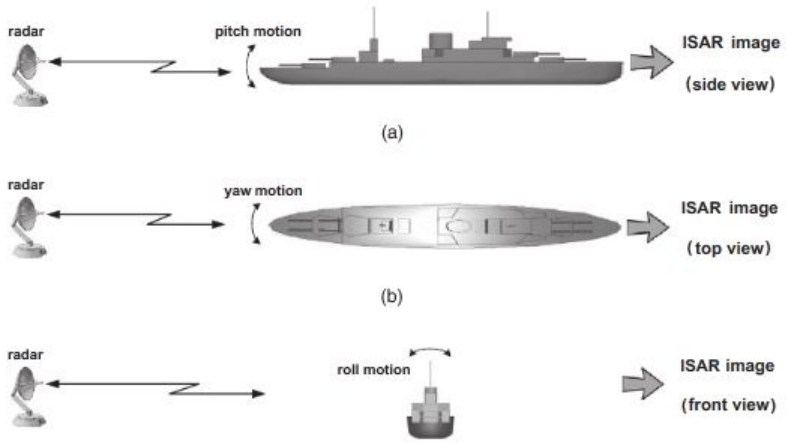

Figure 2.5: The figure indicates the isolated effects of each of the components (*roll, pitch* and *yaw*) on the resulting ISAR image orientation. From [8].

The ideal received signal of a single scatterer in free space, $Y_R(f,t)$, can be modelled by Equation 2.2 [12].

$$Y_R(f,t) = Y(f,t)exp[-j2\pi f(t + \frac{2R_0(t)}{c})] \\ \times \iint \xi(x_1,x_2)exp\{-j2\pi[X_1x_1 + X_2x_2]\}dx_1dx_2 \tag{2.2}$$

where

$$R_0(t) = \alpha_0 + \sum_{k=1}^{N} \alpha_k t^k \tag{2.3}$$

In Equation 2.3, the term α_0 represents the *shifting term* and $\sum_{k=1}^{N} \alpha_k t^k$ represents the *focussing parameters* that are associated with the radial motion of the target, where:

1. α_0 - radial position of the phase centre of the target
2. α_1 - radial velocity of the phase centre of the target
3. α_2 - radial acceleration of the phase centre of the target

If the focussing parameters listed above where known, the effect of the radial movement of the target could be compensated completely, leaving only the target point spread function ($\iint \xi(x_1,x_2)exp\{-j2\pi[X_1x_1+X_2x_2]\}dx_1dx_2$), of which the 2-dimensional Inverse Fourier Transform (IFT) produces the desired focussed complex image of the target, assuming some conditions[1] are met. This form of ISAR image formation is termed the *Range-Doppler technique*. The steps involved in the Range-Doppler image reconstruction are a) deconvolution, b) motion compensation and c) 2-dimensional Inverse Fourier Transform.

2.3 Motion Compensation and Autofocus

As discussed in previous sections, a key element to ISAR imaging is knowledge of the relative motion of the target with respect to the radar. Since the exact

[1] a) The data samples need to be evenly spaced and b) the data grid must be rectangular

motion is rarely known, but required for producing focussed images, motion compensation and autofocussing techniques have been developed [10] [13] [3] [14]. These techniques can be grouped into *parametric* and *non-parametric* techniques, depending on whether a parametric signal model is used in determining the target motion.

The influence of the target radial motion on the ISAR data is twofold, it a) causes misalignment of the range profiles and b) introduces an error in the measured phase of the scatterers. Since two separate effects exist, some non-parametric motion compensation techniques incorporate two separate steps, namely a) *range alignment* and b) *phase conjugation* [15].

2.4 Target Feature Extraction

A second application where aligned high range resolution (HRR) profiles are required for target classification is target *feature extraction*. The aligned profiles can be used to create an average profile, which provides an increase in signal to noise ratio for improved feature identification and extraction. An example of HRR data recorded [1] of a King Air 200 aircraft is shown in Figure 2.6.

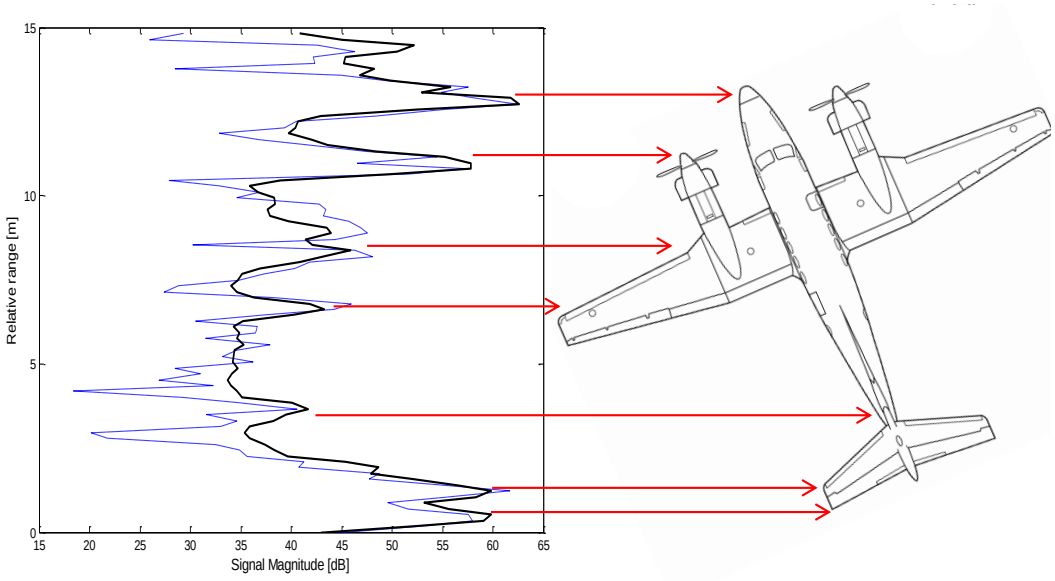

Figure 2.6: The use of HRR profile envelopes for target feature extraction. The blue line indicates a single profile envelope and the black line shows the average profile envelope of 176 *aligned* profiles.

Figure 2.6 provides an example of making use of aligned HRR profile envelopes to extract target features. Provided the target does not undergo major aspect angle changes, a set of aligned profiles may be averaged to create more distinct peaks and improved feature location clarity. Misalignment of the profiles would cause spreading of the peaks in the average profile, so the accuracy of alignment is of great importance when this technique is used for target feature extraction.

Another consideration in the use of aligned HRR profiles is the *association* of HRR profiles between different scans and possibly between different targets, for classification. The use of quality measures (discussed in Chapter 4) may aid in this regard.

Chapter 3

Range Bin Alignment Techniques
a critical review

This chapter presents a critical review of classical and state-of-the-art range bin alignment techniques found in the literature. The purpose of this work is to *study*, *implement* and *critically evaluate* range alignment techniques in order to identify shortcomings and to suggest ways of improving the results or avoiding common errors found in range bin alignment.

Various range bin alignment techniques have been developed. A selection of popular techniques are discussed and implemented on the unaligned data shown in Figure 3.1. The data was measured using the MecORT X-band measurement facility at the Council for Scientific and Industrial Research (CSIR). The data was presented in a CSIR technical report [1] and is used in this study with permission.

The data shown in Figure 3.1 was selected to illustrate the performance of various range bin alignment algorithms due to the following characteristics:

- it contains dominant scatterers
- it is long enough with ample angle variation that the profiles decorrelate towards the end

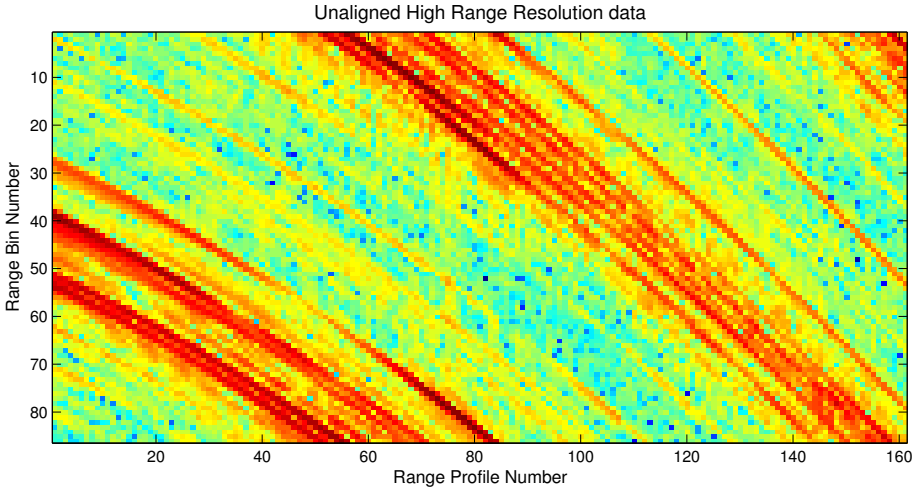

Figure 3.1: An example of unaligned high range resolution data. The data is of a King Air propeller aircraft, measured with a fine range resolution of 17.42cm. Data used with permission [1].

- it requires one to address most of the issues, such as amplitude fluctuations, noise, etc. to achieve good alignment

Apart from the quality of alignment which can be determined visually, a quantitative measure of range bin alignment quality is desirable. The derivation and characteristics of various quality measures for range bin alignment techniques are discussed in Chapter 4. In this chapter, the *sum envelope entropy* will be used as presented in Wang [6].

A single range profile represents a one dimensional projection of the reflectivity function of the a target, distributed over one coarse range bin, with respect to the radar. If the reflectivity function is considered as a random variable, the motion of the scatterers together with the change in aspect angle due to the motion as well as change in interaction with the sea surface[1] from one profile to the next causes variance/fluctuations in the average range profile. The entropy of a random variable is related to the variance (or the standard deviation squared), the proof for a Gaussian random variable is provided in Appendix A. Higher variance/fluctuations produces increased entropy.

[1] with maritime targets

The sum envelope, denoted by $\mathbf{S}$, and sum envelope entropy, H, used in this chapter is defined[2] in Equation 3.1 and Equation 3.2, respectively [6]. More details on the derivation of the sum envelope entropy appears in Section 4.2.

$$S(n) = \sum_{m=1}^{M} |p(m,n)| \tag{3.1}$$

where n denotes the range bin number, m is the profile number, M is the total number of profiles in the data and $p(m,n)$ is the amplitude sample in the n^{th} bin of the m^{th} profile.

$$H = -\sum_{n=1}^{N} S(n) \ln S(n) \tag{3.2}$$

The average of the normalized profiles of the unaligned data shown in Figure 3.1 appears in Figure 3.2.

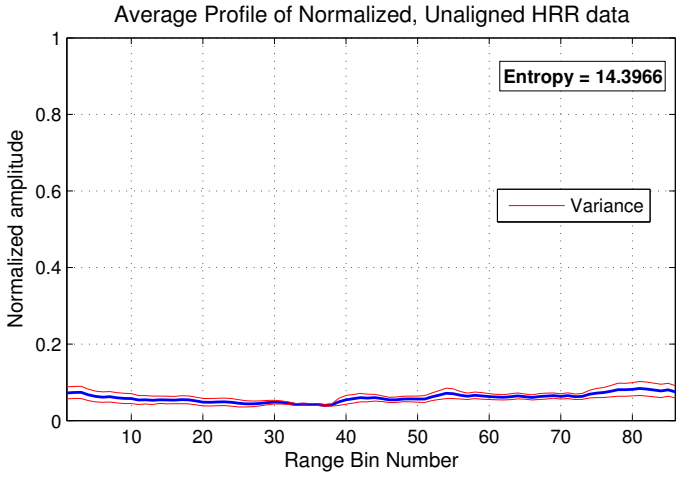

Figure 3.2: The sum envelope of the normalized, unaligned profiles calculated using Equation 3.1 as well as the entropy of 14.3966 calculated using Equation 3.2.

In cases where the profiles are properly aligned, prominent, sharp peaks will appear in the average profile, providing a smaller variance, which would render a

[2]Note that the implemented algorithm uses a counting index starting at 1 and not 0 as stated in the original equation.

small entropy value. Therefore, the smaller the entropy, the better the alignment quality and the higher the probability is of accurately determining the scatterer location based on the locations of the peaks in the amplitude of the average profile. The actual value of the entropy is dependent on the data, which implies that the entropy values for different data sets cannot be used to compare the alignment of one data set with another without first performing some form of normalization on the data.

The sum envelope entropy value of the unaligned data will provide a means of presenting the improvement in range bin alignment by using an alignment technique. The sum envelope entropy value calculated for the data shown in Figure 3.1 using Equation 3.2 is $H = 14.3966$.

A selection of the range bin alignment methods are applied to the data shown in Figure 3.1 to indicate the alignment capabilities of each. Common problems encountered in each of the techniques are summarized at the end of this section. Note that the shifting values obtained in each technique *has not been interpolated*, which causes the aligned data to appear jerky. The "raw" form of the techniques are implemented in this chapter and Chapter 7 presents simple methods for improving the results by using, for example, interpolation.

3.1 Peak alignment

Peak alignment is the simplest range alignment technique. It assumes that a dominant and stable scatterer is present in the data and is used as reference point for the alignment. As the name suggests, the technique simply aligns the peak of adjacent profiles to form its aligned profiles. The peak in each profile is assumed to represent the return from a single dominant scatterer. An example of range alignment using this technique for the unaligned profile shown in Figure 3.1 appears in Figure 3.3

The entropy of the average of the normalised profiles was calculated using Equation 3.2. Figure 3.4 shows the average of the normalized profiles for the data

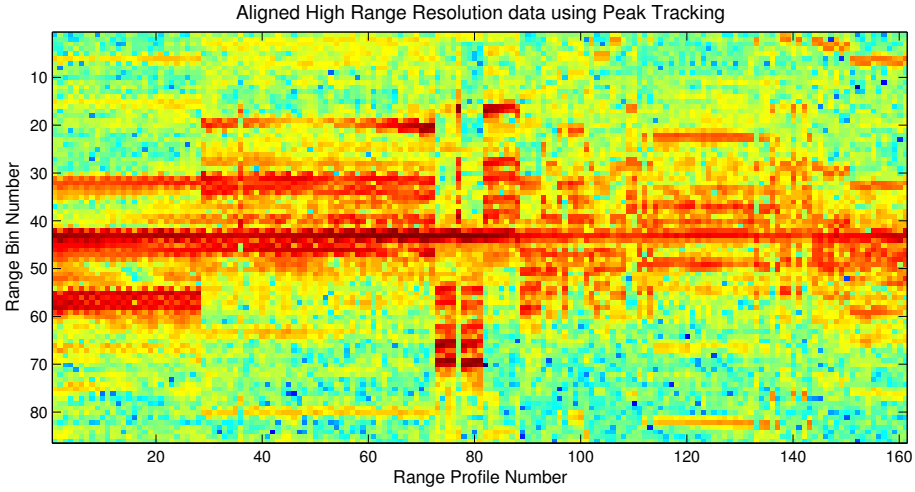

Figure 3.3: An example of aligned high range resolution data using the peak tracking method. Note the errors caused by target scintillation effects. Data used with permission [1].

aligned using peak alignment.

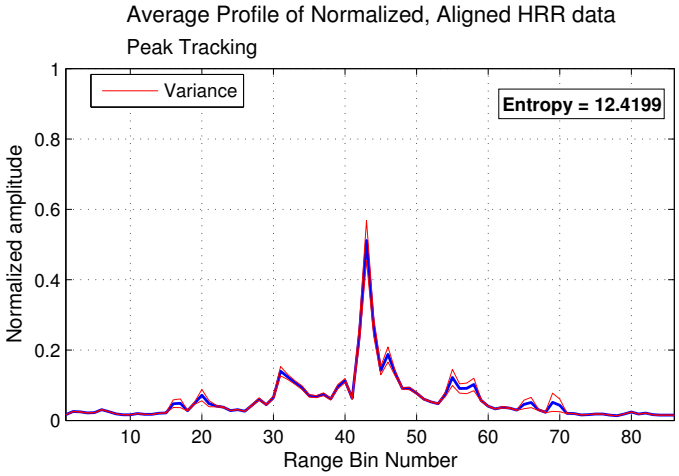

Figure 3.4: This figure shows the average of the normalized profiles that were aligned using the peak of each profile. The calculated entropy of this profile is 12.4199.

The average of the aligned result has an entropy value of 12.4199, which is an

improvement[3] of almost 16% over the unaligned data.

The misalignment caused by using this technique is evident from Figure 3.3. The misalignment is a direct consequence of the unrealistic assumptions that a) only a single dominant scatterer is present throughout the data and b) the largest amplitude return represents this dominant scatterer. Any target fluctuation effects could cause the misalignment seen in the figure. Another observation is the apparent "vibration" of the dominant scatterer returns. This effect is caused by limiting the range bin shifts to integer values. The target return straddles two range bins and at certain points the return folds over and appear as a sub-integer jump or vibration. Interpolating the required shift values to sub-bin accuracy has been shown to alleviate this problem. For the illustrative examples in this chapter, interpolation will not be used. Interpolation of shift values as well as other techniques to mitigate range bin alignment errors are discussed in Chapter 7.

3.2 Envelope correlation

Envelope correlation is a widely used range bin alignment technique. It involves finding the number of shifts, denoted by τ, required to obtain the maximum cross correlation between the profile to be aligned, $\mathbf{P}_m$, and a suitable reference profile, $\mathbf{R}_m$. The cross correlation, $\mathbf{X}_m$, obtained when $\mathbf{P}_m$ is shifted by varying τ_m, can be written as Equation 3.3 [16].

$$X_m(\tau_m) = \sum_{n=1}^{N} R_m(n) \cdot P_m(n - \tau_m) \tag{3.3}$$

Note that complex correlation will not be considered in this study and therefore $\mathbf{P}_m$ and $\mathbf{R}_m$ are the real *envelopes* of the profiles.

Variants of this technique involves the choice of reference profile used [6] [17] [18] and some techniques make use of non-integer shifts in the cross correlation [16].

[3]Smaller entropy is assumed to indicate improved alignment.

3.2.1 Correlation of adjacent profiles

This variant of the envelope correlation method uses the previously aligned profile envelope, denoted as $\hat{\mathbf{P}}_{m-1}$, as the reference profile. Equation 3.3 can be rewritten in this case as Equation 3.4.

$$X_m(\tau_m) = \sum_{n=1}^{N} \hat{P}_{m-1}(n) \cdot P_m(n - \tau_m) \tag{3.4}$$

The cross correlation defined in Equation 3.4 for adjacent profiles is calculated for each of the M profiles. The optimum bin shift that produces the maximum cross correlation value is used to align the profiles. Note that only integer bin shifts are considered here. The aligned data appears in Figure 3.5

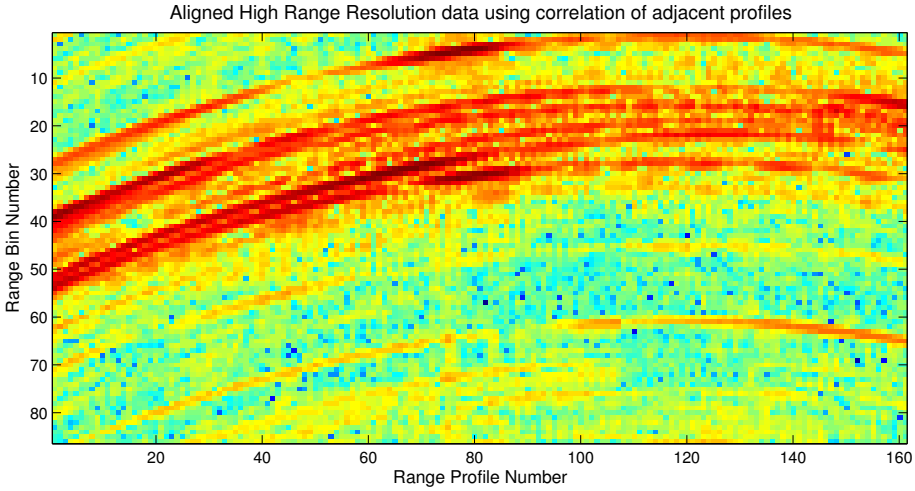

Figure 3.5: An example of aligned high range resolution data using the correlation of adjacent profiles method. Note the very prominent error propagation effect. Data used with permission [1].

Using the preceding aligned profile as reference profile for the cross correlation calculation causes the alignment vector to contain a propagating error throughout the aligned data, as shown in Figure 3.5. The overall nature of the aligned profiles does present improved smoothness when compared to the data that was aligned using the peak alignment method. The average of the normalized profiles is given in Figure 3.6.

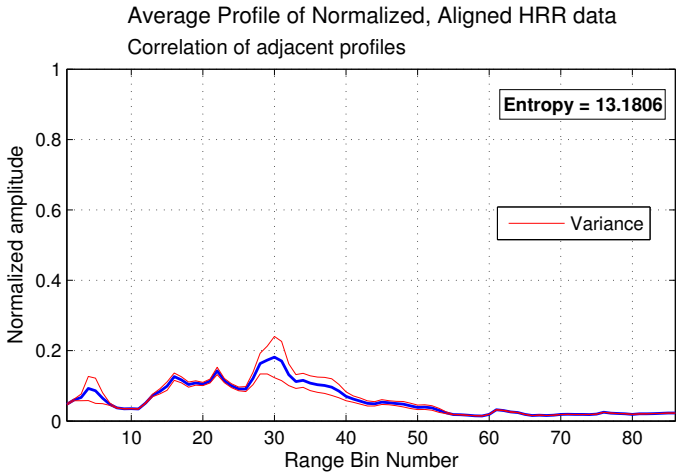

Figure 3.6: This figure shows the average of the normalized profiles that were aligned using the adjacent envelope correlation method. The calculated entropy of this profile is 13.1086.

The entropy of the average of the normalized aligned profiles using this technique is 13.1806, which is an entropy improvement of almost 10% when compared to the unaligned profile.

3.2.2 Non-coherent averaging of profiles to create reference profile

In this technique, the non-coherent average of all previously aligned profile envelopes is used as the reference profile for the cross correlation method. This technique is simpler than exponentially weighted averaging of envelopes [10], discussed in the next section.

The reference profile $\mathbf{R}_m$ is defined in Equation 3.5 [16].

$$R_m(n) = \frac{\sum_{i=1}^{m} \hat{P}_i(n)}{m} \tag{3.5}$$

Note that m represents the profile number and n is the range bin number. The aligned results appear in Figure 3.7. The averaged sum envelope of the profiles

aligned using this method and the amplitude variance per range bin is shown in Figure 3.8.

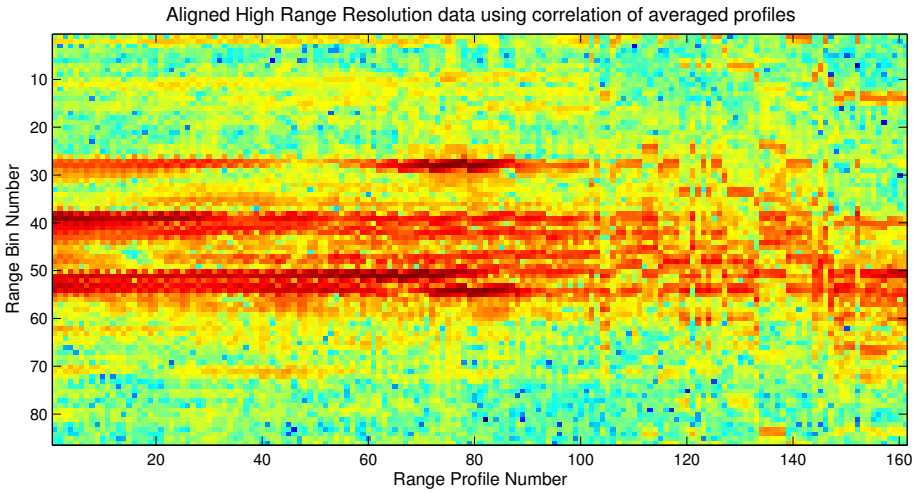

Figure 3.7: An example of aligned high range resolution data using the correlation with the average envelope. Data used with permission [1].

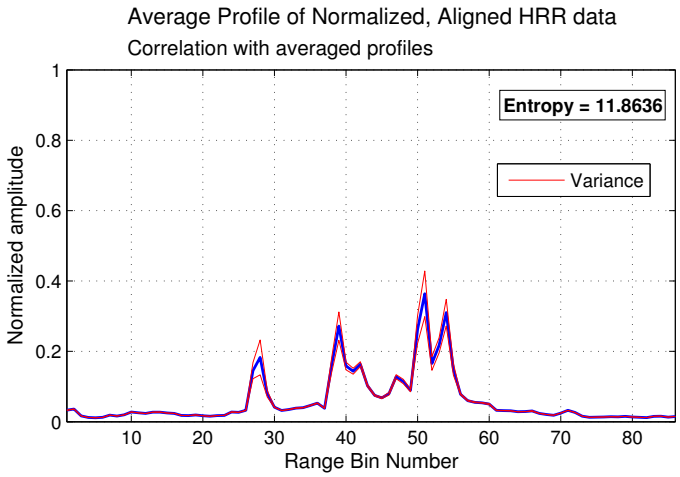

Figure 3.8: This figure shows the averaged sum envelope of the normalized profiles that were aligned using the average of aligned profiles in the correlation method. The calculated entropy of this profile is 11.8636.

The entropy of the average of the aligned profiles was 11.8636, which equates to an entropy improvement of over 21% when compared to the unaligned data entropy.

3.2.3 Exponentially weighted reference profile

To indicate the principle of using an exponentially weighted profile as reference profile for the cross correlation performed with this technique, a basic exponential moving filter is used. An expression for the filter weight W_m is given in Equation 3.6.

$$W_m = \kappa\gamma_m + (1 - \kappa)W_{m-1} \tag{3.6}$$

where W_m is the weighting value that will be applied to the m^{th} range profile, γ_m is the filter gain, which is set to unity and κ is the exponential factor of the filter between 0 and 1. In this example, κ was set equal to $1/m$ where m is the profile number.

The varying filter weights are applied to the profiles in order to suppress the effect of older profiles on the reference profile, and hence, the correlation value. An expression for the reference profile is given in Equation 3.7.

$$R_m(n) = \frac{\sum_{i=1}^{m} W_i \cdot \hat{P}_i(n)}{m} \tag{3.7}$$

Figure 3.9 provides the aligned result.

The improvement in alignment is visible in Figure 3.9. In order to quantify the alignment performance, the average of the sum envelope is given in Figure 3.10.

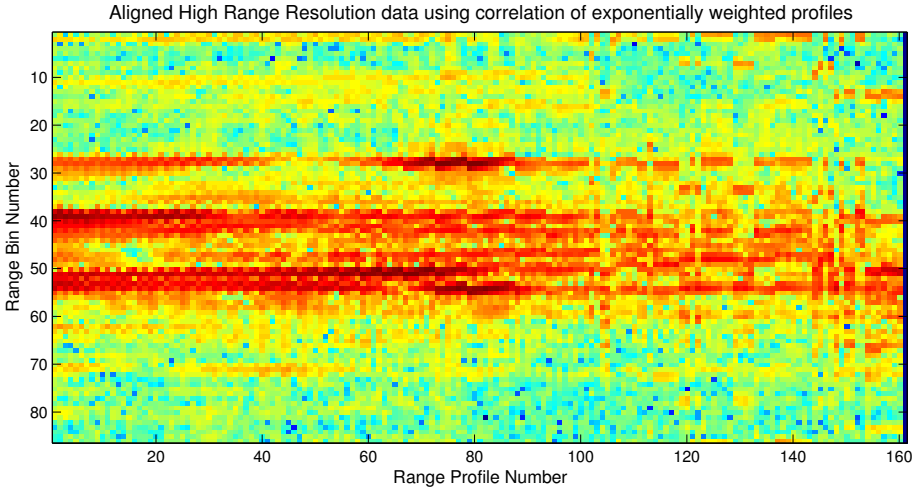

Figure 3.9: An example of aligned high range resolution data using the correlation with a reference profile obtained by exponentially weighted profiles. Data used with permission [1].

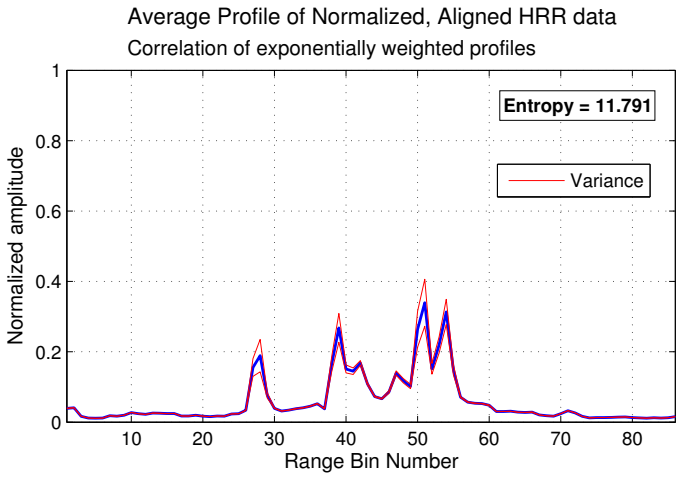

Figure 3.10: This figure shows the average sum envelope of the normalized profiles that were aligned using an exponentially weighted average of previously aligned profiles as reference profile in the correlation method. The calculated entropy of this profile is 11.7910.

The improvement in alignment by using this technique when compared to no alignment is 22%.

3.2.4 Sliding Window Averaging

One consideration regarding the window length of the filter selected previously is that the data may have changing characteristics. To this end, a sliding window approach is also investigates. In order to find optimal values for the window length and κ, a parametric sweep was done which included window lengths between 1 and 160 and κ values ranging from 0.01 to 0.99. The resulting surface plot appears in Figure 3.11. The high entropy at smaller window lengths can be

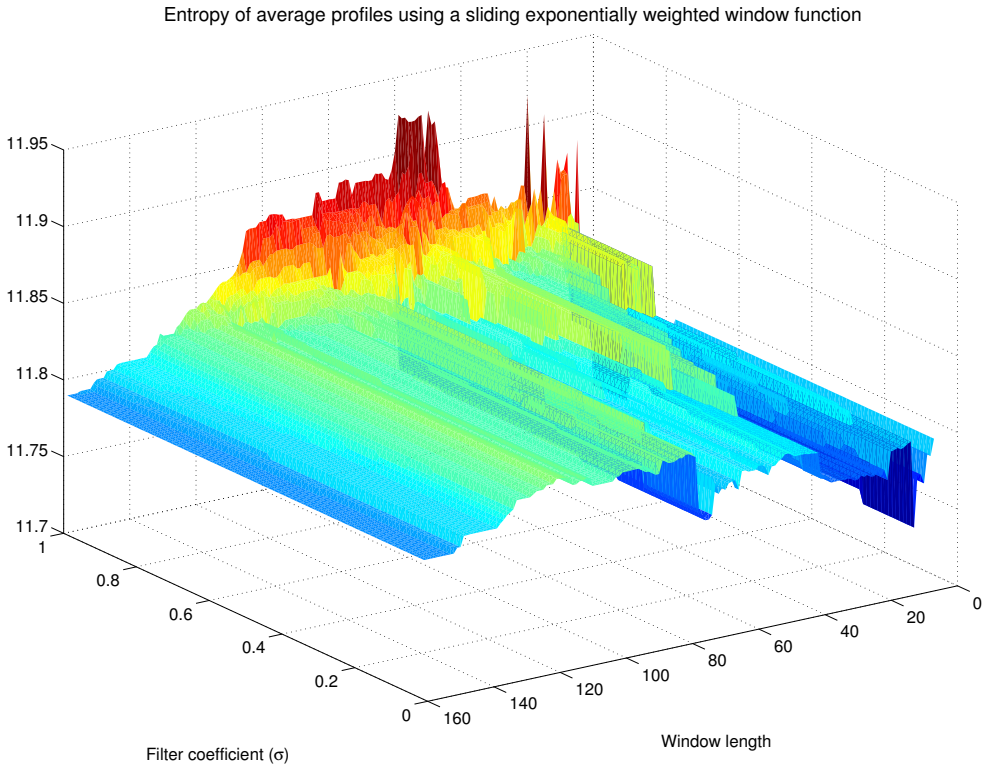

Figure 3.11: The surface plot shows the entropy values of the resulting average profile when an exponential weighting is applied to a sliding window of previously aligned profiles in order to obtain a suitable reference profile.

a result of the settling time of the filter needed for proper filtering. To evaluate the optimal values for the window length and σ, only window sizes larger than 6 profiles are considered.

The optimal[4] values for the sliding window length was **12** and $\mathbf{0.11} \leq \kappa \leq \mathbf{0.2}$. After selecting the optimal values found in the parametric sweep, the alignment was performed on the unaligned data set as before. The aligned result is given in Figure 3.12. The first observable improvement gained when using the sliding

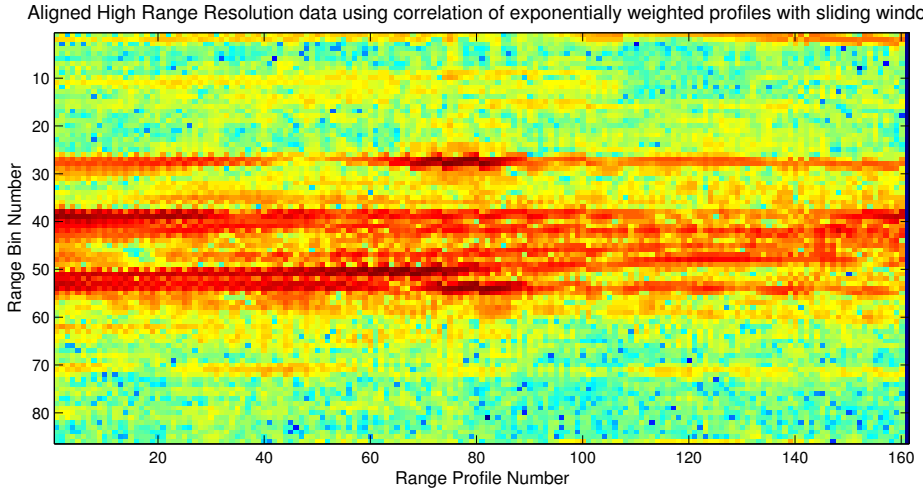

Figure 3.12: An example of aligned high range resolution data using the correlation with a reference profile obtained by exponentially weighted profiles, averaged over a sliding window. Data used with permission [1].

window approach is the improved alignment of particularly the profiles towards the end of the data. The alignment is however degraded by vibration-like noise throughout all the profiles, a result of integer range bin shifts, which is addressed in Chapter 7.

In order to quantify the improvement in the alignment of the profiles, the average of the aligned profiles is presented in Figure 3.13, along with the calculated entropy. The improvement in entropy achieved by making use of an optimally tuned sliding window is 22.64% compared to the entropy of the unaligned data.

[4]Values that resulted in the minimum entropy

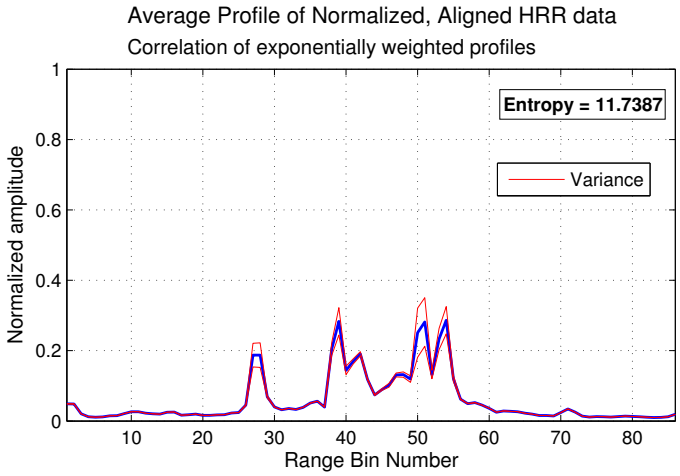

Figure 3.13: This figure shows the average of the sum envelope of the normalized profiles that were aligned using the an exponentially weighted average of previously aligned profiles as reference profile in the correlation method. Averaging was performed over a sliding window selection of profiles. The calculated entropy of this profile is 11.7387.

3.3 Spectral domain phase difference

A spectral domain phase difference method, or *frequency domain realignment* is described in Chen [3]. The method relies on two assumptions: a) that the phase change from one profile to the next is constant and b) the phase variation due to aspect angle changes is negligible c) range bin migration of dominant scatterers are less than one bin per profile [19]. The steps involved in this method are:

1. Estimate the *phase* of the Fourier Transform of each profile
2. Calculate the *phase difference* of adjacent profiles
3. Determine the *magnitude* of the Inverse Fourier Transform of the phase difference calculated in the previous step
4. The location of the maximum value of the magnitude calculated in the previous step indicates the range bin shift required for profile alignment

In cases where the assumptions listed above hold, the spectral domain phase difference approach may prove useful. In this study, targets with high velocities are considered, such as the data of the King Air 200 shown in Figure 3.1. The high radial velocity of these targets cause multiple range bin shifts per profile, so this technique will not result in adequate alignment.

3.4 Minimum entropy of the average range profile

The minimum entropy of the average between the profile to be aligned and some reference profile is similar to the cross correlation methods, the only diffence being the cost function of this method is the entropy, $\mathbf{H}_m$, defined in Equation 3.8, of a reference profile instead of the cross correlation, $\mathbf{X}_m$, used in Section 3.2. Xi [10] claims that this technique offers a reduced number of errors due to scintillation effects compared to the correlation method.

$$H_m(\tau_m) = -\sum_{n=1}^{N} R_m(n, \tau_m) \ln R_m(n, \tau_m) \tag{3.8}$$

3.4.1 Entropy of adjacent profiles

Any misalignment will cause smoothing of R_m and hence, an *increased* entropy value [10]. The first implementation of this method uses the summed envelope of the previously aligned profile, $\hat{\mathbf{P}}_{m-1}$, and the current profile, shifted by τ_m, as the reference profile. The summed envelope is defined in Equation 3.9.

$$R_m(n, \tau_m) = \frac{\hat{P}_{m-1}(n) + P_m(n - \tau_m)}{\sum_{n=1}^{N} \left(\hat{P}_{m-1}(n) + P_m(n - \tau_m) \right)} \tag{3.9}$$

The shift value, τ_m, that results in a minimum entropy of the average between two adjacent profiles is used to align the data. The aligned profile is given in

Figure 3.14.

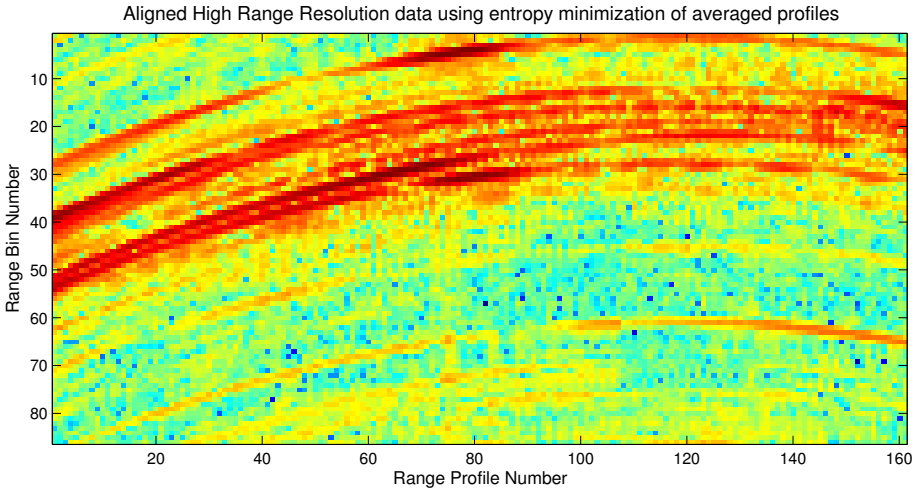

Figure 3.14: The aligned profiles from using the envelope entropy of the average of adjacent profiles is presented above. Data used with permission [1].

The result shown in Figure 3.14 presents many similarities to the cross correlation of adjacent profiles result shown in Figure 3.5, particularly the obvious problem of error accumulation. To quantify the quality of the alignment, the entropy[5] of the average normalized profile is given in Figure 3.15

The accumulating error causes severe degradation of the average profile entropy, as seen previously. The improvement in alignment when using this technique compared to the unaligned data is slightly above 9%.

Previously, the error accumulation effects were minimized by making use of a reference profile that is defined as the average of the previously aligned profiles.

[5]Note the definition in Equation 3.2 is used for calculating the entropy used as quality indicator.

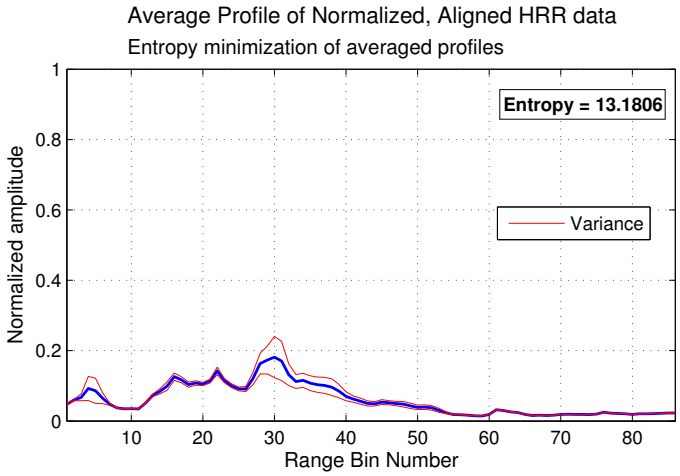

Figure 3.15: This figure shows the average of the normalized profiles that were aligned using the minimum entropy of average profiles method. The calculated entropy of this profile is 13.1806.

3.4.2 Non-coherent average of aligned profiles as reference profile

The minimum entropy method is implemented by using the average of all previously aligned profiles, $\bar{\hat{\mathbf{P}}}_{m-1}$, and the current profile, shifted by τ_m, as the reference profile. The reference profile is calculated using Equation 3.10.

$$R_m(n, \tau_m) = \frac{\bar{\hat{P}}_{m-1}(n) + P_m(n - \tau_m)}{\sum_{n=1}^{N} \left(\bar{\hat{P}}_{m-1}(n) + P_m(n - \tau_m) \right)} \tag{3.10}$$

The resulting aligned profile appears in Figure 3.16.

One observation from Figure 3.16 is the degradation of the alignment towards for the later range profiles. This is due to the averaging over many profiles and the "smoothing" of the reference profile. Next, a sliding window is applied to attempt compensating for this problem.

The entropy of the average of the normalized, aligned profiles provides a quantitative measure of the improvement in alignment. The entropy and the average

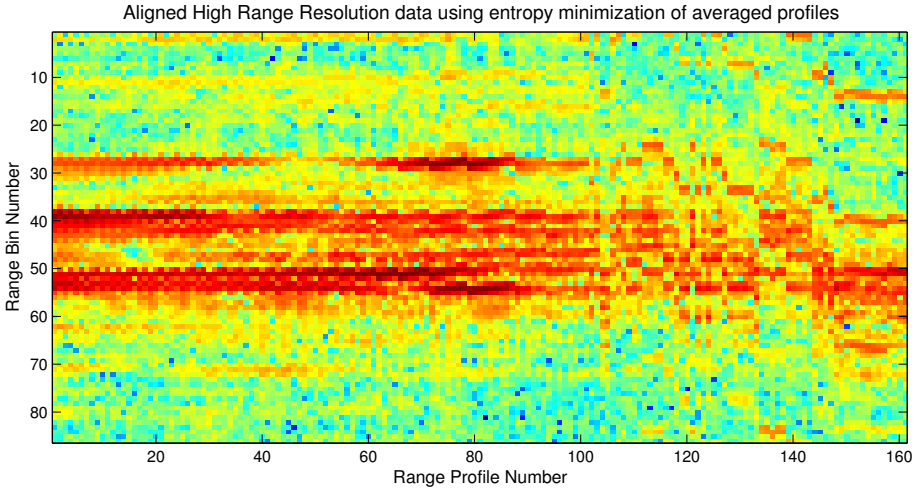

Figure 3.16: The aligned profiles from using the envelope entropy of the average of the profile to be aligned and the average of all previously aligned profiles is presented above. Data used with permission [1].

profile can be found in Figure 3.17.

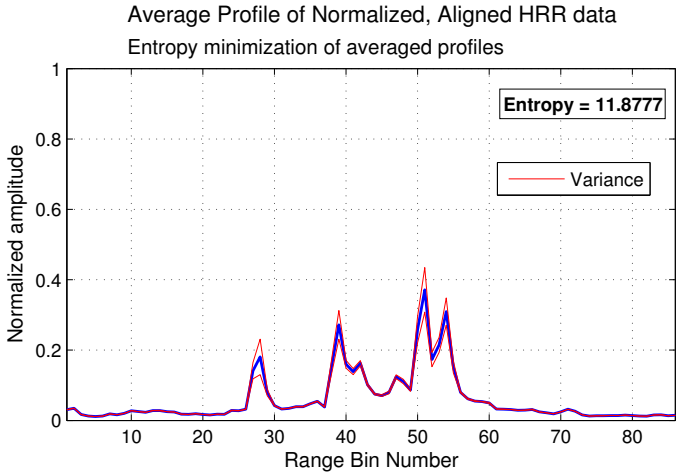

Figure 3.17: This figure shows the average of the normalized profiles that were aligned using the minimum entropy of the averaged profiles method. The reference profile is the mean of all previously aligned profiles. The calculated entropy of this profile is 11.8777.

The improvement in alignment using this method is over 21%.

3.4.3 Sliding window average of range profiles as reference profile

In Section 3.2.4 it was seen that making use of a sliding window in the calculation of the reference profile lead to improved alignment results. In order to alleviate the problems seen in Figure 3.16, a *sliding window* is used to determine which profiles should be used in obtaining the reference profile. Obviously the length of the window is dependent on the similarity of the profiles. If the profiles are identical, the ideal window length would be equal to the number of profiles. Conversely, is the profiles are changing significantly from one profile to the next, shorter window lengths would accommodate these rapid changes. Figure 3.18 shows the resulting entropy for various window lengths. Note that this implies using a fixed window length throughout the data.

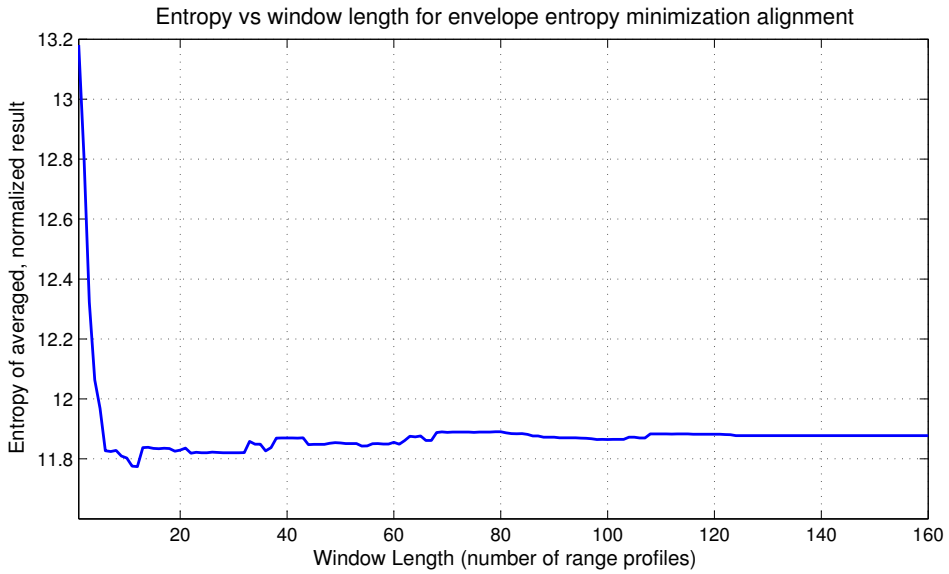

Figure 3.18: This plot indicates the entropy of the alignment result obtained when using a sliding window in the calculation of the reference profile for the envelope entropy minimization bin alignment method.

The minimum entropy was found when using a window length of **12**. Using this window length, the aligned data is presented in Figure 3.19.

Again, the quantitative measure of the alignment quality is determined using the

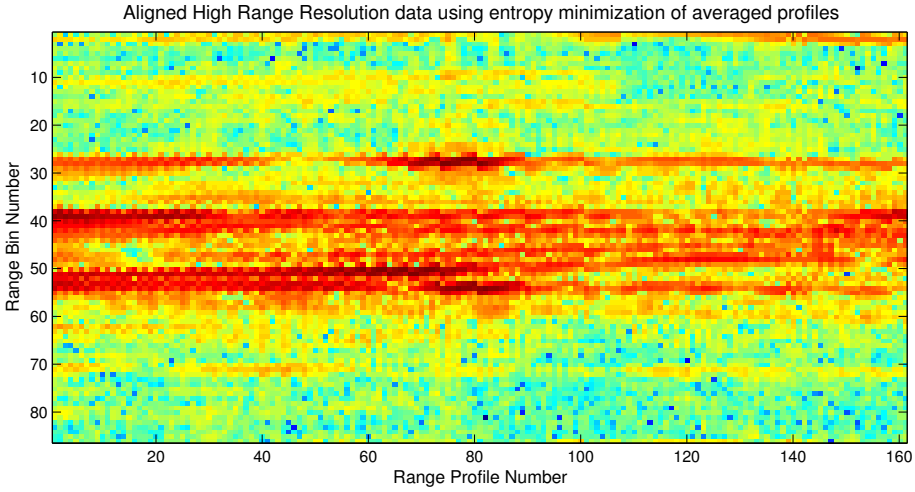

Figure 3.19: The aligned profiles from using the envelope entropy of the average of the profile to be aligned and the average of a sliding window selection of previously aligned profiles is presented above. Data used with permission [1].

average of the normalized and aligned profiles, shown in Figure 3.20.

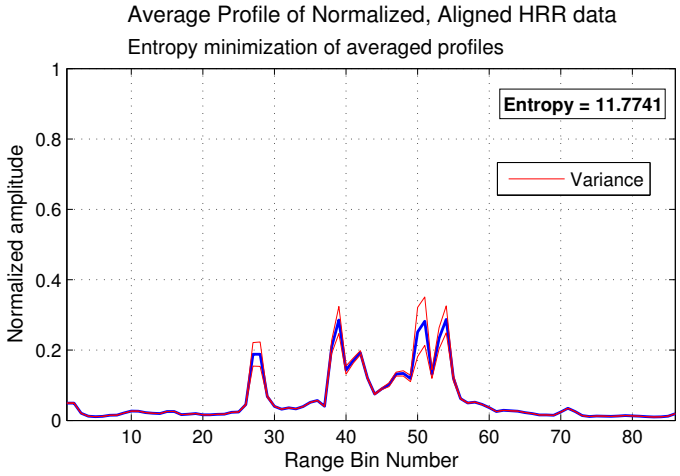

Figure 3.20: This figure shows the average of the normalized profiles that were aligned using the minimum entropy of the averaged profiles method. The reference profile is the mean of a sliding window selection of previously aligned profiles. The calculated entropy of this profile is 11.7741.

The resulting improvement in alignment, compared to the unaligned data entropy is 22.27%.

3.5 Sub-integer range bin alignment

The sub-integer range bin alignment method presented by Muñoz-Ferreras and Pérez-Martínez [16] is discussed here. The algorithm was tested against various state-of-the-art algorithms, including the minimum entropy method and the global range alignment method. The results in [16] indicate that the method provides improved range alignment compared to other techniques on simulated and actual data. Robustness against i) *Target Fluctuation*, ii) *Noise and Clutter* iii) *Error Accumulation* and iv) *Target Vibration effects*.

The algorithm makes use of a reference profile, $\mathbf{R}_m$, defined in Equation 3.11 [16] to calculate the cross correlation, $X(\tau_m)$, shown in Equation 3.3.

$$R_m(n) = \frac{m}{m+1} R_{m-1}(n) + \frac{1}{m+1} P_m(n) \tag{3.11}$$

The algorithm uses multiplication with a phase ramp in the frequency domain to achieve sub-integer size range bin shifts. This is a valid assumption when the shift property of the Fourier transform is considered to produce the shifted profile, $\hat{P}_m(n - \tau_m)$, as defined in Equation 3.12 and using the Fast Fourier Transform (FFT) as approximation to the Fourier transform.

$$\hat{P}_m(n - \tau_m) = IFFT\left\{e^{j(2\pi/N)\tau_m \mathbf{n}} FFT\{P_m(n)\}\right\} \tag{3.12}$$

where $\mathbf{n}$ is the vector $[0, 1, ..., N-1]^T$ and N is the total number of range bins per profile, as before. The optimal shift value, $\hat{\tau}_m$ is defined to be the value of τ_m that results in maximum correlation. Equation 3.13 expresses the optimal shift value mathematically.

$$\hat{\tau}_m = \arg\max_{\tau_m} X(\tau_m) \tag{3.13}$$

Finally, the optimal shift value is used with Equation 3.14 to calculate the aligned profile, $\hat{\mathbf{P}}_m$.

$$\hat{P}_m(n) = P_m(n - \hat{\tau}_m) \tag{3.14}$$

The algorithm consists of *seven* steps. These include [16]:

Step 1. (First profile). Let $\bar{\mathbf{P}}_0 = \mathbf{P}_0$.

Step 2. Calculate reference profile (m), $\mathbf{R}_m$ using Equation 3.5.

Step 3. Calculate the envelope correlation, $X_m(\tau_m)$ using Equation 3.3 for each integer [0,1,...,N-1] shift value of τ_m.

Step 4. Determine the value of τ_m that resulted in the maximum cross correlation. This value is termed $\tau_{m,0}$.

Step 5. Obtain the optimal shift $\hat{\tau}_m$ using $\tau_{m,0}$ as initial guess to the Nelder-Mead optimization algorithm.

Step 6. Obtain $\hat{\mathbf{P}}_m$ using Equation 3.14. If the optimum shift value, $\hat{\tau}_m$, is not an integer, use Equation 3.12.

Step 7. $(m = m+1)$. If $m \leq M-1$, where M is the total number of range profiles, go to Step 2 for alignment of the next profile.

The Nelder-Mead optimization algorithm used is the built-in MATLAB® function `fminsearch` [20]. The input function handle `FUN` is defined below:

```
1      % Function Handle
2      FUN = @(T)FourierXCORR(R(:,m+1),P(:,m+1),T,N);
3    % Function definition
4  function XC = FourierXCORR(R,P,T,N)
5
6  XC = -sum(abs(R).*abs(ifft((fftshift(fft(P,[],1),1))...
7      .*([exp(-1i*2*pi*(T.*[0:(N/2)-1]./N)) ...
8      exp(-1i*2*pi*(T.*([N/2:N-1]-N)./N))]).',[],1)));
```

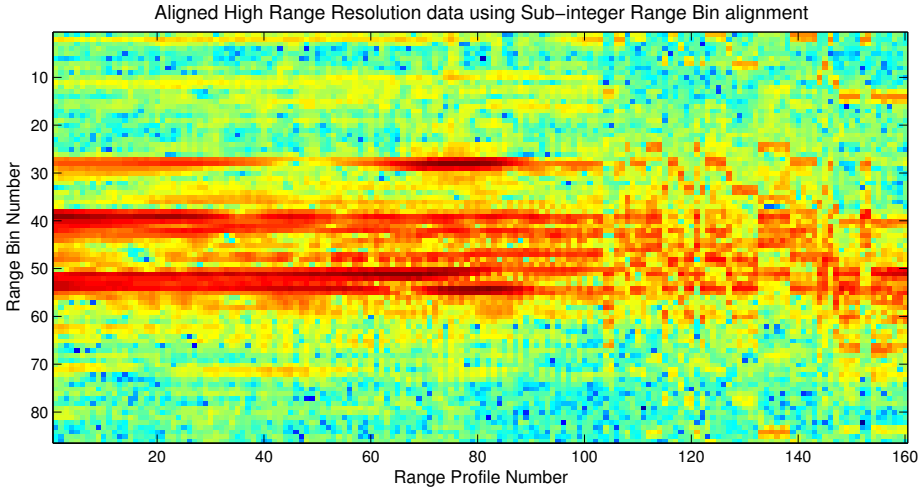

Figure 3.21: The aligned profiles using the Sub-integer range alignment algorithm from Muñoz-Ferreras and Pérez-Martínez [16] is presented above. Data used with permission [1].

The algorithm was applied to the unaligned data shown in Figure 3.1. The resulting aligned profile is given in Figure 3.21.

Note that the algorithm as implemented in [16] claims an improvement in robustness when compared to the global range alignment method of [6] due to not limiting the number of range bin shifts allowed from one profile to the next. Although it could provide an improvement, it results in alignment errors due to locking on incorrect scatterers in the profile. Because of target fluctuation effects, even dominant scatterers may have fluctuating amplitudes that may be exceeded by other scatterers in the profile.

The second observation of Figure 3.21 is the obvious degradation of the effect of the reference profile towards the end of the data. The reason for this phenomenon is related to the fact that the reference profile should provide an adequate representation of the profiles in close proximity to the profile to be aligned. When the reference profile is calculated as the average of *all* previously used reference profiles, regardless of the changes in the statistical properties of the actual profiles, the averaging operation causes a reduction in the validity of the reference profile. One obvious solution to this problem is to make use of *sliding window*

averaging, discussed in Section 7.1.

The quantitative quality of the range alignment is given by the average envelope entropy, as before. Figure 3.22 presents the average envelope of the aligned data.

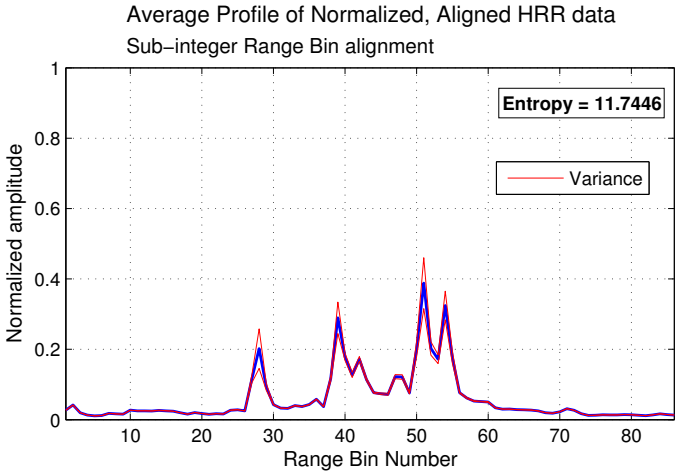

Figure 3.22: This figure shows the average of the normalized profiles that were aligned using the Sub-integer range alignment method. The calculated entropy of this profile is 11.7446.

The improvement in entropy of the average envelope profile is 22.58%.

3.6 Hough transform

The Hough Transform[6] method achieves superior alignment performance in high clutter environments when compared to the cross correlation methods [21]. It is therefore ideal in applications such as surface movement control at an airport terminal.

The range alignment algorithm using the Hough transform presented in Sauer [21] was applied to the data [1] shown in Figure 3.1. The Hough transform result of the original and filtered data is given in Figure 3.23.

[6] A detailed explanation of the Hough transform appears in Appendix C.

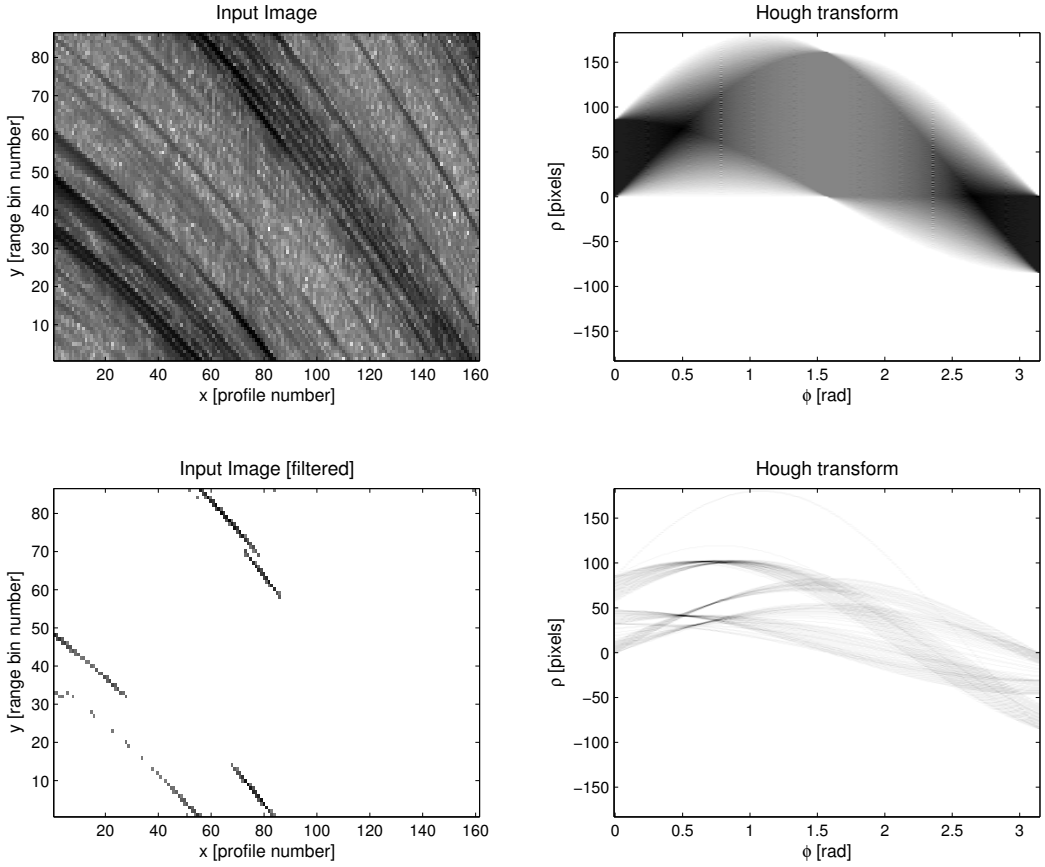

Figure 3.23: The Hough transforms of the original data (top left) and the filtered data (bottom left) appears to the right of each figure. The Hough transforms where calculated using an angular resolution of $\pi/180$.

The filtered data is obtained by simply discarding pixels in the original data that is smaller than 50% of the peak in the image. Using the peak of the filtered data Hough transform, located at (0.6458,101.4706), a straight line with (m,c)=(0.7536,168) is approximated with Equations C.3 and C.4. Applying this straight line approximation for range alignment produces the result shown in Figure 3.24.

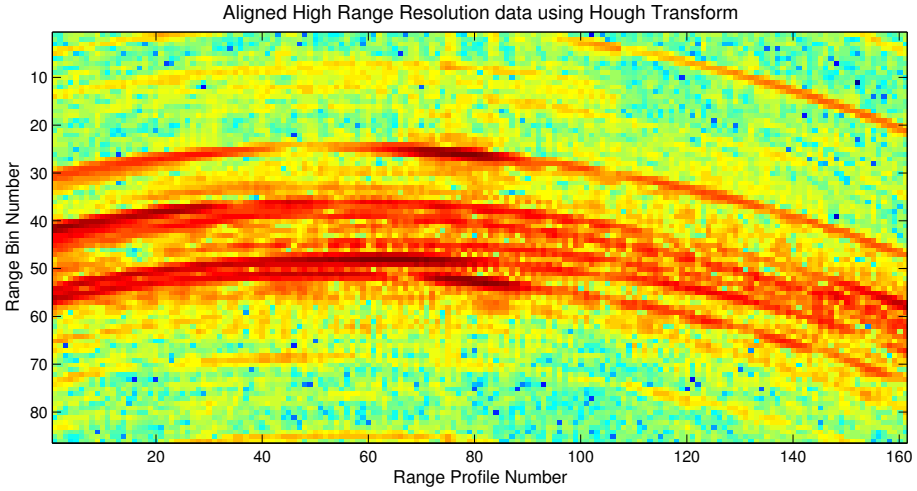

Figure 3.24: The aligned profiles from using the Hough transform method is presented above. Data used with permission [1].

The mismatch in the assumption of linear radial velocity and the actual radial velocity of the target causes misalignment of profiles. Note that even though it appears to be a propagation error, no reference profiles were used and it is in fact *not* a propagation error, but a miscalculated velocity estimate. Applying this technique using fewer range profiles per Hough transform calculation will improve the result, but with a substantial increase in computations. The alignment quality is determined using the average of the normalized and aligned profiles, shown in Figure 3.25.

The resulting improvement in alignment, compared to the unaligned data entropy is 15.56%.

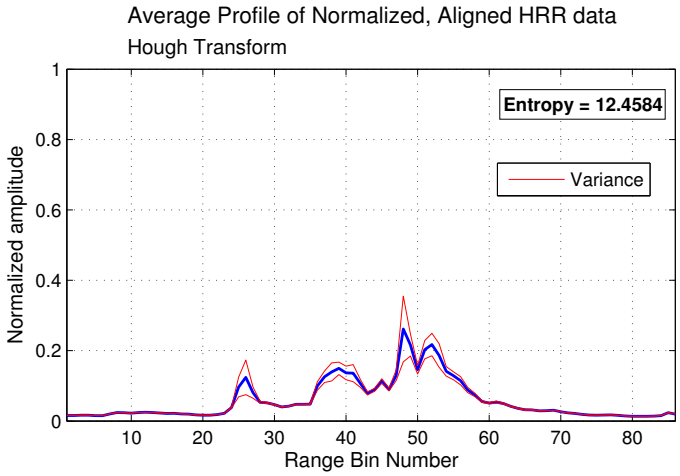

Figure 3.25: This figure shows the average of the normalized profiles that were aligned using the Hough transform method. The calculated entropy of this profile is 12.4584.

3.7 Global method

The global range alignment method presented in Wang [6] is an optimization algorithm designed to align profiles to maximize the resulting contrast-like value (C) of the sum envelope ($S(n)$), defined in Equation 3.1 and Equation 3.15, respectively.

$$C = \sum_{n=0}^{N-1} S(n)^2 \tag{3.15}$$

The sum envelope, given by Equation 3.1, is calculated for varying shifts applied to the current profile. The contrast defined in Equation 3.15 is used to determine if the iterations are causing an *enhancement* (increased contrast) of a *degradation* (decreased contrast) of the range alignment. The steps are calculated according to the contrast history throughout the iterations. The method uses a polynomial model to estimate the shifts required for bin alignment. The equations used and logical flow diagram of the technique is provided in Appendix B.

The original global alignment method as presented in Wang [6] was applied to

the unaligned data shown in Figure 3.1. The resulting aligned profile appears in Figure 3.26. The algorithm was followed by an improved global range align-

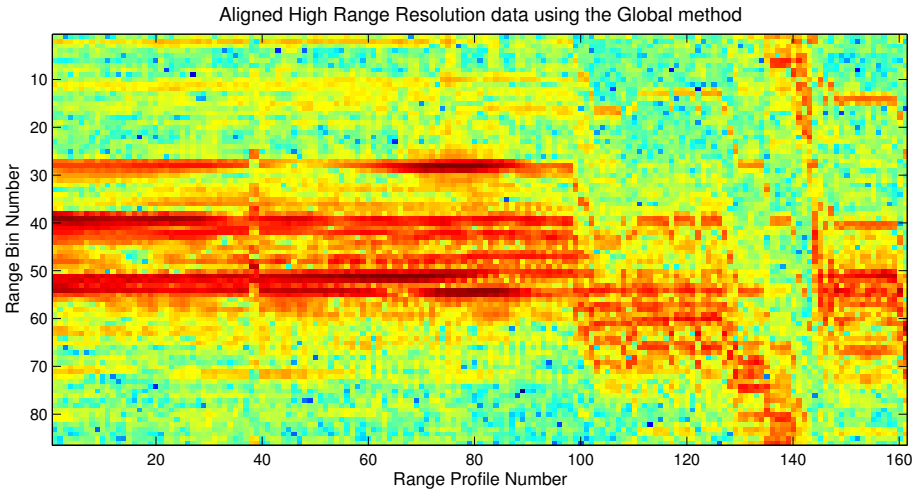

Figure 3.26: The aligned profiles using the Global range alignment algorithm from Wang [6] is presented above. Data used with permission [1].

ment algorithm Wang [22]. The improved algorithm uses a slightly altered cost function and iteration parameters, yielding comparable results with improved computational efficiency when compared to the original global alignment method [22].

The entropy of the normalized average range envelope shown in Figure 3.27 was calculated as 12.2727, which results in an improvement of 17.31% when compared to the unaligned data.

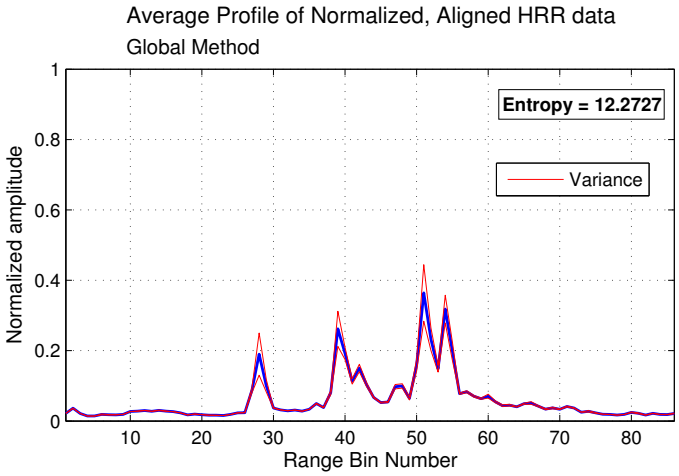

Figure 3.27: This figure shows the average of the normalized profiles that were aligned using the global range alignment method. The calculated entropy of this profile is 12.2727.

3.8 Summary

Problems found in existing range bin alignment techniques, as seen in this chapter and from the literature, include:

Error Accumulation (EA)

- Propagation of misalignment throughout the aligned data. Examples of this error appear in Figures 3.5 and 3.14.

Scatterer Fluctuation Effects (SFE)

- Alignment techniques sensitive to scatterer fluctuations. Good example of misalignment caused by scatterer fluctuation is the peak alignment result in Figure 3.3.

Degraded performance with noise and clutter (DPN)

- Misalignment caused by noise and clutter in the data. Some techniques in the literature are described as more robust against the effects of noise and clutter.

Integer Range Bin Shifts (IRBS)

- Limitation of some techniques which causes vibration-like misalignment. An example of this effect is seen in Figures 3.9.

Limited Target Manoeuvrability (LTM)

- Some techniques only achieve alignment when the target adheres to restricted manoeuvrability, such as constant velocity, etc. A technique that fails with highly manoeuvring targets is the Hough transform method. The results appear in Figure 3.24.

Degraded Performance with Platform/Target Vibration (DPPTV)

- Misalignment resulting from vibration effects of the target and/or radar platform. These effects are investigated in Chapter 6.

Computationally Expensive (CE)

- Some techniques, such as the sub-integer alignment method, make use of optimization algorithms which adds to the computational load of the algorithm.

A selection of autofocus and range bin alignment techniques found in the literature suffer from varying combinations of the problems listed above. A summary of popular techniques and common errors or shortcomings of each is given in Table 3.1.

Algorithm Name	**Disadvantages**						
	EA	SFE	DPN	IRBS	LTM	DPPTV	CE
Peak alignment	x	x	x	x			
Minimum entropy of the average range profile [23]				x	x	x	
Hough transform [21]	x	x		x	x	x	x
Global method [6]					x	x	x
Shift-and-convolution [24]	x	x		x			
Envelope correlation	x	x		x			
Exponentially averaged envelope correlation			x		x	x	
Extended envelope correlation [17]					x		
Image Contrast Based Autofocus [11]					x	x	x
Image Entropy Based Autofocus [10]					x	x	x
Prominent Point Processing					x	x	
Phase Gradient Autofocus [13]			x		x		
Subinteger Range-bin Alignment [16]							x

Table 3.1: This table provides a summary of the characteristics of various range bin alignment and autofocussing techniques investigated during the literature study.

An entropy function was defined in Equation 3.2 and used throughout this chapter to quantify the alignment accuracy. The values obtained for the various alignment methods is given in Table 3.2.

Algorithm Name	**Alignment Quality**	**Entropy**	**Improvement**
Unaligned data	Poor	14.3966	0.00%
Peak alignment	Moderate	12.4199	15.92%
Envelope correlation [*adjacent profiles*]	Poor	13.1806	9.23%
Envelope correlation [*average reference profile*]	Moderate	11.8636	21.35%
Envelope correlation [*exponentially weighted reference profile*]	Moderate	11.7910	22.10%
Envelope correlation [*optimal exponentially weighted reference profile*]	Good	11.7387	22.64%
Minimum entropy [*adjacent profiles*]	Poor	13.1806	9.23%
Minimum entropy [*average reference profile*]	Moderate	11.8777	21.21%
Minimum entropy [*windowed average reference profile*]	Good	11.7741	22.27%
Hough Transform	Poor	12.4584	15.56%
Global method	Moderate	12.2727	17.31%
Sub-integer method	Moderate	11.7446	22.58%

Table 3.2: The table indicates the range bin alignment algorithms that were implemented and the resulting entropy value as calculated using Equation 3.2 for each result.

Assumptions drawn from the results shown in Table 3.2 include:

- The entropy of the unaligned data exceeds all the entropy values obtained by using some form of alignment algorithm.
- Making use of a reference profile generally improves the entropy.
- Using reference profiles that are exponentially weighted provided an improvement in entropy.
- Using a sliding window for calculating the reference profile improved the

entropy.

- Of the algorithms implemented, the envelope correlation method using an optimal exponentially weighted reference profile provided the smallest entropy value[7].

In cases where adjacent profiles were used as the reference profile, error accumulation problems occurred which causes severe degradation of the "quality" of alignment when the quality is measured in terms of entropy.

An investigation of more quality measures is presented in Chapter 4 and the sensitivity of each measure to the common errors found in high resolution range profiles appears in Chapter 6. Additionally, methods of mitigating algorithm specific errors such as error accumulation is included in Chapter 7.

[7]Note that the parameters for the exponential weighting function was in fact optimized to minimize the entropy.

Chapter 4

Quality measures for range bin alignment

This chapter describes quality measures currently found in the literature for quantifying the performance of the bin alignment algorithms. In the previous chapter, the sum envelope entropy, defined in Equation 3.2, was used to quantify the alignment performance of the various techniques. It was found that this entropy value was severely degraded when the *error accumulation* problem was present. A sensitivity analysis of various quality measures to common problems encountered in high resolution range profile alignment follows in Chapter 6.

Commonly used quality measures in ISAR imaging is *image entropy* and *image contrast*. Of course, using these quality measures requires an ISAR image to be formed. Wang [6] [22] and Son [19] present various measures of quality for range alignment. These measures include:

- Sum Envelope Contrast
- Sum Envelope Entropy
- Global Envelope Correlation
- Variance of the peak location

- Burst Derivative

The *sum envelope* used in the calculation of the first two quality measures was defined in Equation 3.1, Chapter 3. Note that the quality measures listed above can be used as 1) the cost function for the alignment algorithm or 2) the quality of the entire aligned data set. In this chapter, the focus is mainly on the latter.

A definition and short discussion on each of the quality measures is presented next.

4.1 Sum Envelope Contrast

The definition of the sum envelope contrast as presented in Wang [6] appears in Equation 4.1. The full derivation and validation of Equation 4.1 appears in Appendix D.

$$C = \sum_{n=1}^{N} S(n)^2 \tag{4.1}$$

The expression for the sum envelope contrast given in Equation 4.1 will incorrectly favour (produce *higher* contrast) for datasets with a larger number of range bins. To avoid this error, the contrast value is divided by the number of range bins, N, after the summation. This includes the capability of using this performance measure for analysing multiple files.

4.2 Sum Envelope Entropy

The original definition of entropy provided by Shannon [25] was used to quantify the expected value of the information in a message and forms a cornerstone of information theory. The definition provided by Shannon was extended in Pun[26] to create an automatic threshold selection method for producing a two-level

image from an input grey tone image. The image entropy definition presented in Pun[26] is extended in Pal [27] to define a *global*, *local* and *conditional* image entropy. Properties of the image entropies defined in Pal [27] include:

- *Global image entropy* - provides a measure of the *greyness ambiguity* in the image
- *Local* and *Conditional image entropy* - provides information regarding the *spatial ambiguity* of the image by measuring intraset homogeneity and interset contrast.

Additionally, the entropic measures can be used for image segmentation, which provides another definition for entropy, namely the *positional entropy* [27]. This definition of image entropy is used in Flores [28] for range-Doppler processing. An ISAR autofocus technique based on minimizing this entropy function is presented in Xi [10].

The entropy is applied in range alignment as a measure that relates to the standard deviation [1], or fluctuation, caused by misalignment between range profiles on the average profile. A larger standard deviation implies that the probability of accurately estimating the position of the scatterer based on the location of the peaks in the average profile envelope is lower than cases where the standard deviation is low. The proof of this statement for a normally distributed random variable is provided in Appendix A. The entropy for *sinc* functions of varying widths is shown in Figure 4.1 to illustrate the effect of the standard deviation on the entropy value.

[1] the standard deviation is the square root of the variance

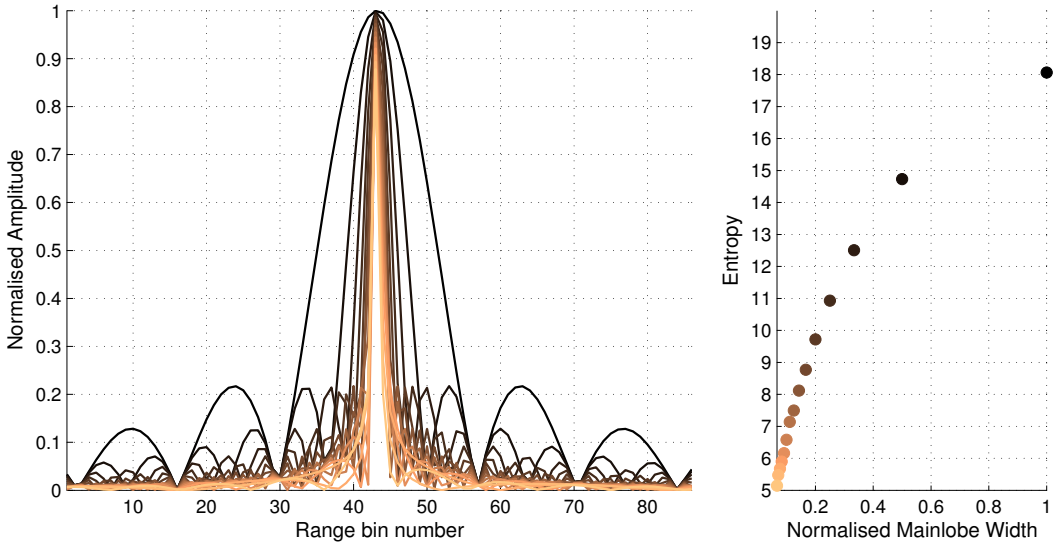

Figure 4.1: The effect of the standard deviation on the entropy is simulated in this example by *sinc* functions with varying widths.

When the sum envelope is used for this calculation, the misalignment from one profile to the next will cause an increase in the standard deviation of the resultant average profile and hence, increased uncertainty in the exact position of the scatterers. The increased standard deviation produces an increase in entropy. This concept is illustrated in Figure 4.2 by using a shifted copy of a simulated range profile, or *sinc* function, for calculating the sum envelope and resulting entropy.

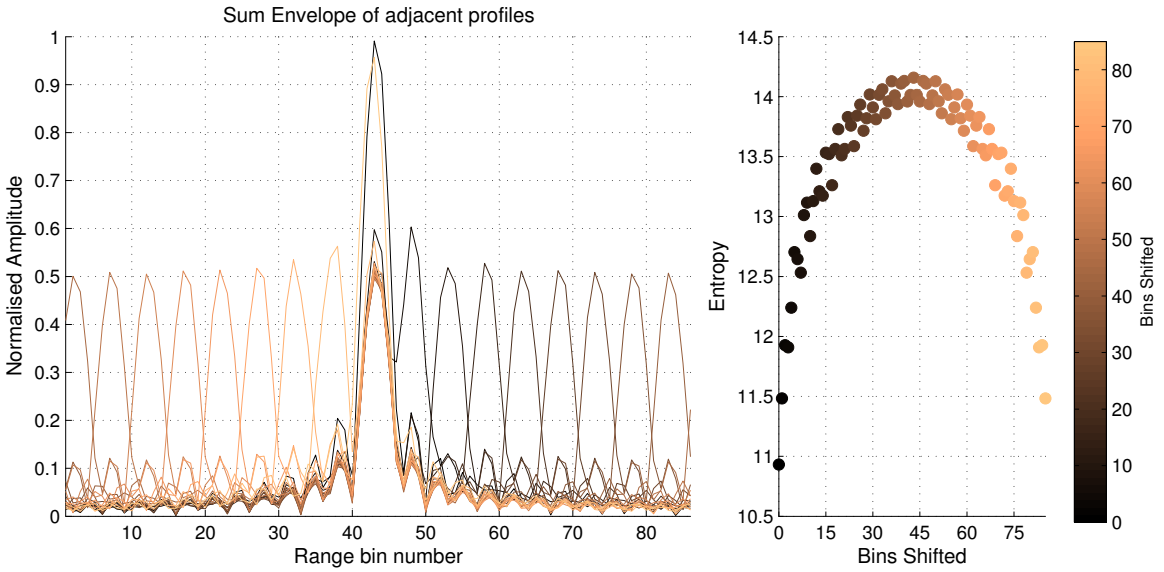

Figure 4.2: The influence of the misalignment of adjacent profiles on the resulting sum envelope entropy is investigated by simulating a range profile as a *sinc* function and calculating the sum envelope using a shifted copy of the original envelope.

The full derivation of the entropy function used for quantifying the range bin alignment quality appears in Appendix D. The sum envelope entropy is shown in Equation 4.2.

$$H = -\sum_{n=1}^{N} S(n) \ln S(n) \tag{4.2}$$

In order for Equation 3.1 to be applicable to multiple sets of files, it is again divided by N to form an averaged value of the entropy. Failure to perform the normalisation will incorrectly favour datasets with a higher number of range bins per profile. The derivation of Equation 4.2 as given in Wang [6] is given in Appendix D.

4.3 Global Envelope Correlation

Correlation is a commonly used cost function in range bin alignment techniques. Wang [6] defines the *global envelope correlation* as quality measure for range bin alignment, given in Equation 4.3.

$$G = \sum_{m=1}^{M-1} \sum_{l=m+1}^{M} \phi(m,l) X(m,l) \tag{4.3}$$

where $X(m,l)$ is the envelope correlation of profiles m and l, defined in Equation 4.4 and $\phi(m,l)$ is a weighting function, defined in Equation 4.5.

$$X(m,l) = \sum_{n=1}^{N} |p(m,n)|\,|p(l,n)| \tag{4.4}$$

$$\phi(m,l) = \exp\left[-\left(\frac{l-m}{\delta}\right)^2\right] \tag{4.5}$$

It is not clear from Wang [6] whether the value of δ is fixed throughout the operation or recalculated for each new correlation value. Since δ was not defined as a vector, it is assumed to be fixed throughout the calculation.

To investigate the influence of the δ parameter on the final envelope correlation result, simulation of an idealised data set, shown in Figure 4.3 is used. This first order test will also produce an estimate for the expected cross correlation value.

The envelope correlation was calculated for a parametric sweep of $0 < \delta \leq 1000$. The results appear in Figure 4.4.

Figure 4.4 indicates that lower values of δ results in a smaller global envelope correlation value that changes significantly as δ is increased from 0 to 100. The change in the resulting correlation value from one δ value to the next reaches an approximately constant value when δ is larger than 100.

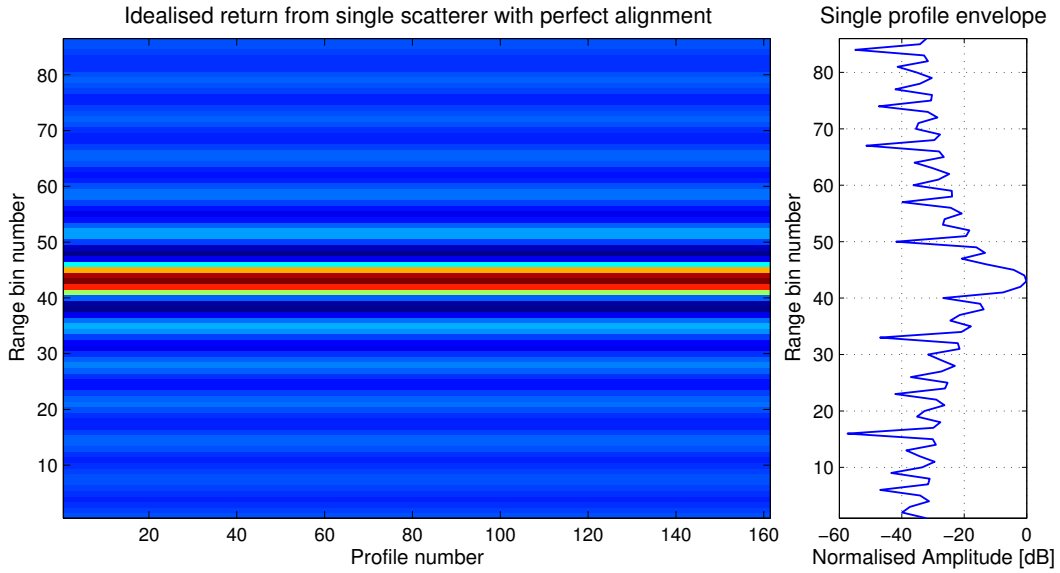

Figure 4.3: A number of assumptions are made in generating this figure. Note that only a single, non-fluctuating target is assumed. The return can therefore be modelled using the *sinc* function. No clutter or noise is added, as this figure is used for investigating an *idealised* scenario.

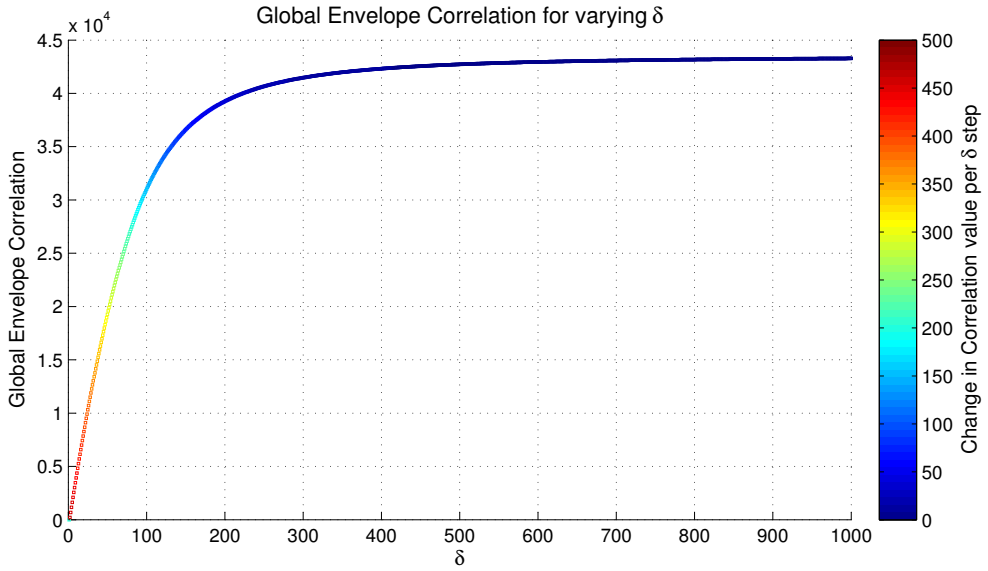

Figure 4.4: The influence of δ on the global envelope correlation result and the associated gradient.

4.4 Variance of the peak location

Ideally, the variance of the location of a dominant scatterer return after range bin alignment should be zero. This quality measure is used under the assumption that a) the data contains a single dominant scatterer and b) the return from this scatterer is in fact also the largest (peak) return in every range profile. One may regard the peak variance as the cost function of the peak alignment technique. While target fluctuation effects may severely degrade the validity of this value as a measure of quality, it will still be included in the study for completeness. The definition of the peak location variance, $\nu[n_p]$, appear in Equation 4.6.

$$\nu[n_p(m)] = \frac{1}{M}\sum_{m=0}^{M-1} n_p(m)^2 - \left[\frac{1}{M}\sum_{m=0}^{M-1} n_p(m)\right]^2 \tag{4.6}$$

For the purposes of this study, the MATLAB® built-in function, `var` is used to determine $\nu[n_p]$. Alternative definitions to Equation 4.6 as presented in Wang [6] appears in Appendix D.

4.5 Mean Squared Envelope Difference

Applying the mean squared envelope difference is an exploratory investigation to attempt to identify an additional measure to specify the correctness of the aligned data. The measure relies on the fact that if two identical profiles are perfectly aligned, the difference between the envelopes over all range bins will be zero. Any misalignment or amplitude variance between adjacent profiles will translate in an increased mean squared difference. The calculation of the mean squared envelope difference is performed using Equation 4.7.

$$D = \left[\sum_{n=1}^{N}\sum_{m=2}^{M}(p_{m-1,n} - p_{m,n})^2\right]^{\frac{1}{2}} \tag{4.7}$$

The mean squared envelope difference will be susceptible to incorrect results when anomalous effects are present, such as target fluctuations. The sensitivity of all the measures discussed in this section to commonly found anomalies in data is addressed in Chapter 6.

4.6 Burst Derivative

The burst derivative approach to ISAR motion compensation was originally proposed by Bocker and Jones [29] and extensively analysed in Son [19]. The burst derivative is calculated using the target reflectivity in the *frequency domain*, thus eliminating the 2-dimensional IFFT required in ICBA and IEBA, which results in significant improvement in computational efficiency [29]. A discussion on the burst derivative in terms of the velocity and acceleration estimation errors as given in Son [19] appears in Appendix D.

The burst derivative, as defined in Bocker and Jones [30] is given in Equation 4.8.

$$B(\hat{v},\hat{a},\hat{j}) = \sum_{n=0}^{N-1}\sum_{m=0}^{M-1}\left|\frac{\partial}{\partial m}\hat{P}(m,n;\hat{v},\hat{a},\hat{j})\right| \tag{4.8}$$

where $\hat{P}(m,n;\hat{v},\hat{a},\hat{j})$ is the compensated sample in the n^{th} range bin of the m^{th} profile when estimates of the radial velocity, acceleration and jerk, denoted as $\hat{v}$, $\hat{a}$ and $\hat{j}$, respectively, were used for motion compensation.

For the purposes of this study, the motion compensation parameter of concern is assumed as the range bin shift vector, τ, that results from the target motion and not the specific values of velocity, acceleration and jerk. The advantage of only considering the resulting range bin shift is that the target motion is not required to strictly fit a polynomial as before. The definition for the burst derivative used for the remainder of the investigation appears in Equation 4.9.

$$B(\tau) = \sum_{n=0}^{N-1} \sum_{m=0}^{M-1} \left| \frac{\partial}{\partial m} \hat{P}(m, n; \tau_m) \right| \tag{4.9}$$

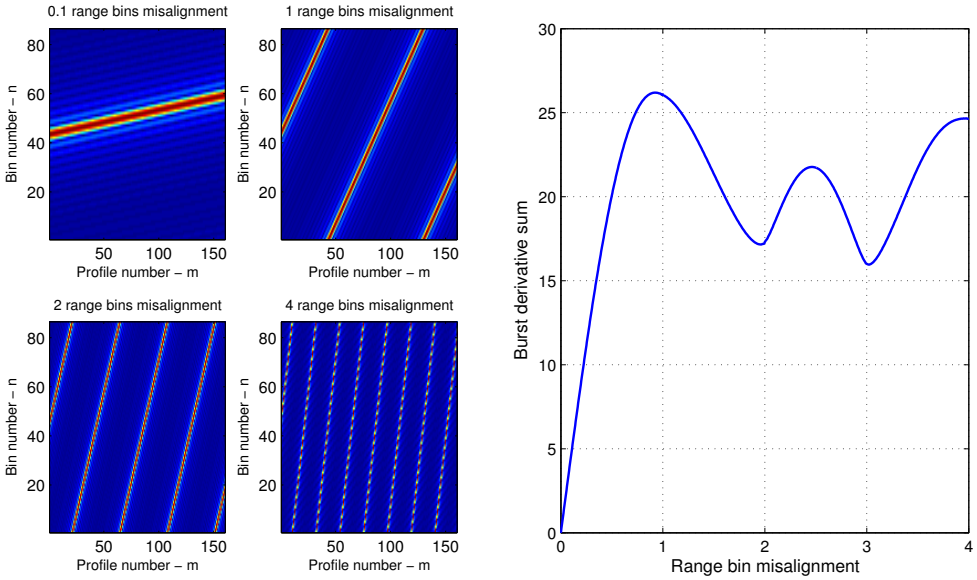

Figure 4.5: The idealised data shown in Figure 4.3 was adjusted to simulate linear misalignment (left). The burst derivative sum for varying misalignment gradients appear to the right.

Figure 4.5 shows data simulated to display a linear misalignment and the burst derivative sum for varying misalignment gradients.

4.7 Summary

This chapter presents and discusses range alignment quality measures found in the literature. These quality measures are used to quantify the alignment quality of aligned data sets. Some quality measures may favour particular alignment techniques without adequately indicating improved alignment, so using multiple quality measures provide added means of verifying the alignment quality achieved by alignment techniques. The sensitivity of the quality measures to various factors is investigated in Chapter 6.

Chapter 5

Alignment and Typical Alignment Quality Values for Measured data

This chapter presents results obtained by applying the alignment techniques presented in Chapter 3 to measured data of the Beechcraft King Air 200 propeller aircraft and the Umoya Omusha sailing yacht. In contrast to the data used in Chapter 3, the data and results presented in this chapter are *not normalised*, to provide realistic quality measure values.

5.1 Aircraft data

The aircraft data presented in this section was measured during a propeller aircraft NCTR measurement trial, held in September 2009 at the CSIR. The data used is that of the King Air 200 propeller aircraft. A schematic of the aircraft is provided in Figure 5.1. The aircraft is 13.34m long with a wingspan of 16.61m.

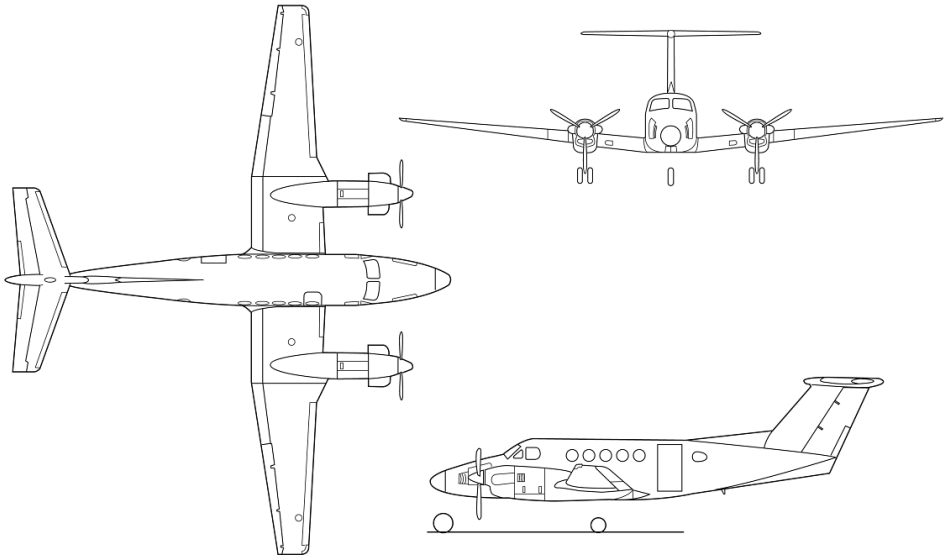

Figure 5.1: Schematic of the Beehcraft King Air 200 propeller aircraft including top, front and side views.

An example of results obtained in the alignment of measured data appear in Appendix E. Typical values for the measured envelopes are indicated in Table 5.1.

File	Number of profiles	Number of fine range bins	Fine range resolution	Average over complete data set				
				Min	Mean	Max	Median	Variance
Air File 1	5764	86	17.42 cm	7.25	106.3	616.4895	71.4597	3.86E+04
Air File 2	1873	106	17.67 cm	6.67	80.809	302.5773	66.7666	4.38E+03
Air File 3	1324	106	17.67 cm	4.49	57.176	190.6151	48.2049	1.51E+03
Air File 4	437	86	17.42 cm	9.76	123.84	529.3691	77.6505	1.36E+04
Air File 5	5023	86	17.42 cm	9.37	125.39	610.5431	83.7892	2.57E+04
Air File 6	6830	86	17.42 cm	5.46	87.292	544.2821	57.1924	2.59E+04
Average	-	-	-	**7.17**	**96.801**	**465.64603**	**67.51055**	**18291.9833**

Table 5.1: File details and typical values for the aircraft data envelopes.

The normalised mean envelope magnitude for all the files listed in Table 5.1 is presented in Figure 5.2 as a function of range from the radar and approximated aspect angle of the aircraft with respect to the radar.

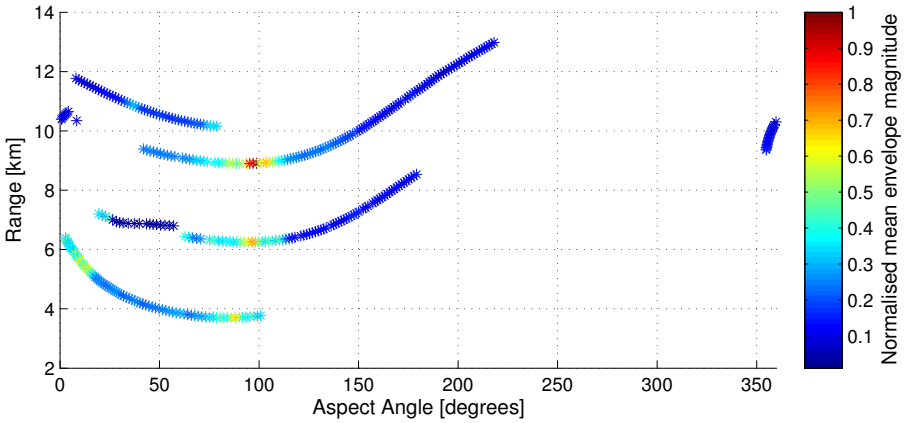

Figure 5.2: Returned signal magnitude as a function of aspect angle and range for the data captured of the King Air 200 propeller aircraft.

Figure 5.2 indicates that in general, maximum retuned signal magnitudes are received close to the instance where the target is turning, or when the velocity of the target with respect to the radar changes sign.

5.1.1 Algorithm Performance

The performance of the techniques presented in Chapter 3 in aligning the data of the aircraft is summarised in Table 5.2.

Method	% of instances in nth position									
	1st	2nd	3rd	4th	5th	6th	7th	8th	9th	10th
Peak Alignment	20	55	9	1	0	0	0	1	1	2
Neighbour Correlation Maximization	0	2	9	27	24	9	9	0	0	0
Average Correlation Maximization	0	1	18	21	16	11	12	1	1	1
Exponentially Weighted Correlation Maximization	0	1	5	10	16	18	11	1	11	9
Sliding Exponentially Weighted Correlation Maximization	0	1	3	7	16	17	17	1	8	12
Neighbour Entropy Minimization	0	0	0	0	1	5	7	17	10	43
Average Entropy Minimization	0	0	0	0	2	8	11	34	22	5
Sliding Average Entropy Minimization	0	0	0	0	1	7	10	27	28	8
Global Range Alignment	0	11	38	15	6	5	5	0	1	1
Sub-integer range alignment	66	12	2	0	0	0	0	0	0	2

Table 5.2: The performance of the range alignment techniques presented in Chapter 3 on aircraft data.

Table 5.2 shows the performance of the range bin alignment techniques when applied to the measured aircraft data. The alignment was performed and the rankings were determined based on the quality measures of the aligned profiles. The results for each quality measure appear in the first section of Appendix F.

The high number of instances where the peak alignment technique produces optimal alignment occurs when i) the variance of the peak location and ii) the burst derivative quality measures determine the alignment quality. It is important to take note of the limitations of the peak alignment technique and the visual quality of the alignment obtained when using it. The sub-integer range alignment algorithm is used for the analysis of typical quality measure values obtained in properly aligned data.

5.1.2 Typical quality measure values

Histograms of the quality values calculated for data aligned using the sub-integer algorithm appear in Figure 5.3. The data was aligned in chunks of 0.5 seconds (roughly 58 profiles per chunk).

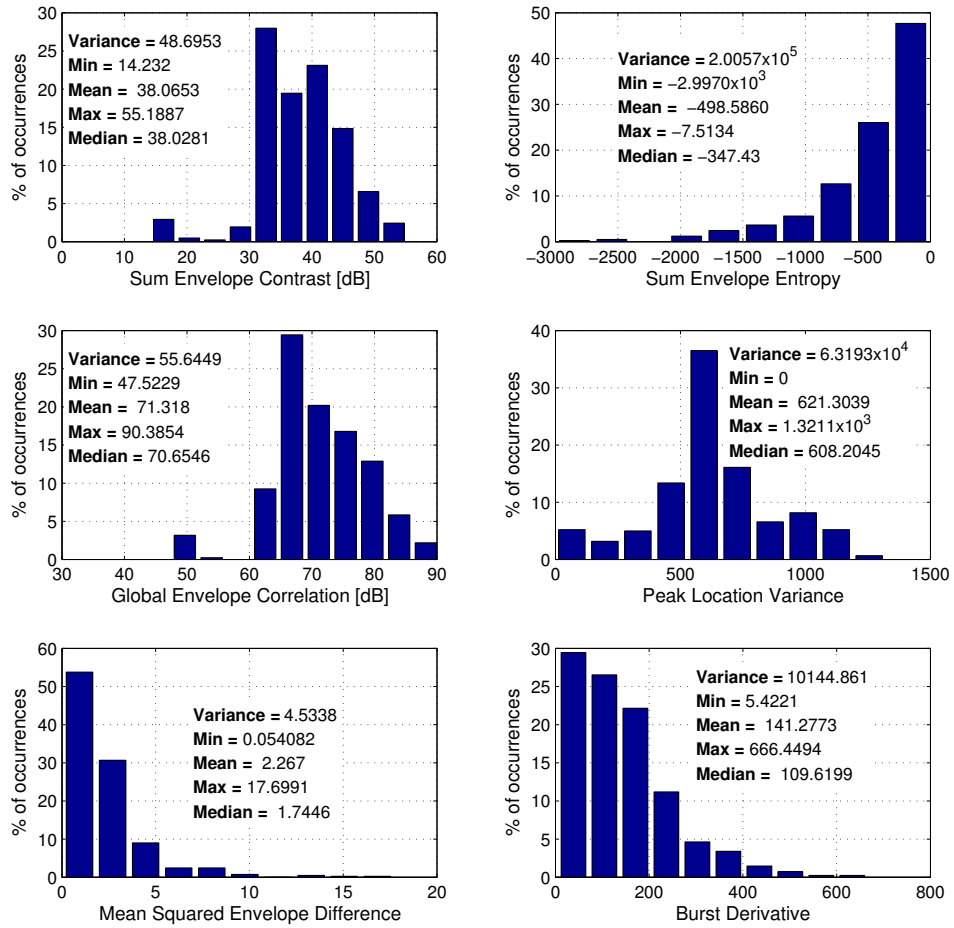

Figure 5.3: Typical quality values for aligned airborne data. The method used was the sub-integer alignment algorithm and the data aligned was 0.5 seconds long.

5.2 Maritime data

The maritime data processed in this section was made during the CSIR Awarenet Td0.5 trial in Simon's Town during October 2010. The target of interest is the Umoya Omusha sailing yacht. A photo of the yacht appears in Figure 5.4.

Figure 5.4: Photograph of the Umoya Omusha sailing yacht used in HRR measurements during October 2010. From [1].

An example of results obtained in the alignment of measured data appear in Appendix G. Typical values for the measured envelopes are indicated in Table 5.3.

File	Number of profiles	Number of fine range bins	Fine range resolution	Average over complete data set				
				Min	Mean	Max	Median	Variance
Maritime File 1	9389	86	21.78 cm	14.6744	297.0329	2.35E+03	154.9793	2.22E+05
Maritime File 2	8281	86	21.78 cm	6.358	129.8207	1.47E+03	67.0716	6.32E+04
Maritime File 3	8781	69	21.72 cm	12.8234	258.4823	2.05E+03	139.3556	2.32E+05
Maritime File 4	7133	86	21.78 cm	7.252	169.1155	1.77E+03	79.1834	1.14E+05
Maritime File 5	7465	86	21.78 cm	7.2073	170.376	1.78E+03	78.4402	1.13E+05
Maritime File 6	8133	69	21.72 cm	9.0101	194.719	1.78E+03	97.9235	1.49E+05
Maritime File 7	4985	69	21.72 cm	8.6656	190.7792	1.68E+03	95.4717	1.16E+05
Average	-	-	-	**9.4272571**	**201.47509**	**1840.1857**	**101.77504**	**144223.29**

Table 5.3: File details and typical values for the maritime data envelopes.

The normalised mean envelope magnitude for all the files listed in Table 5.3 is presented in Figure 5.5 as a function of range from the radar and approximated aspect angle of the yacht with respect to the radar.

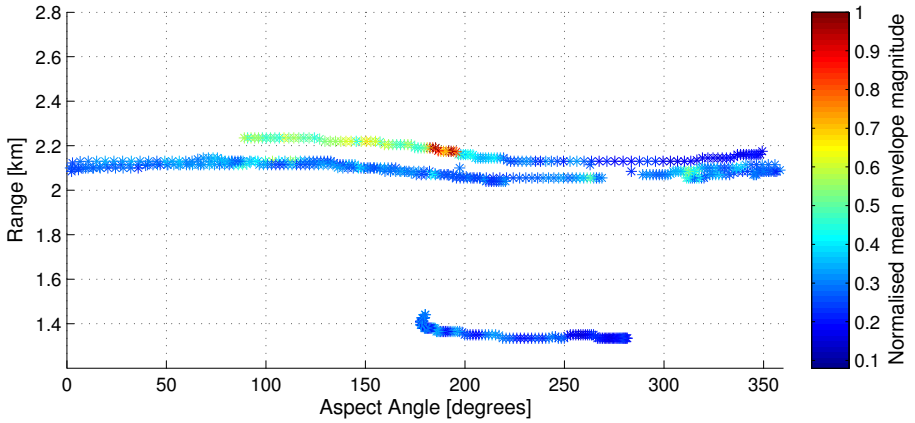

Figure 5.5: Returned signal magnitude as a function of aspect angle and range for the data captured of the yacht.

Figure 5.5 indicates less variation in signal magnitude compared to that of the aircraft data shown in Figure 5.2. No clear variation in magnitude with changes in aspect angle appear and the slow speed of the yacht is represented by the very small changes in range.

5.2.1 Algorithm Performance

The performance of the techniques presented in Chapter 3 in aligning the data of the sailing yacht is summarised in Table 5.4.

Method	% of instances in nth position									
	1st	2nd	3rd	4th	5th	6th	7th	8th	9th	10th
Peak Alignment	33	29	28	7	1	0	0	1	2	4
Neighbour Correlation Maximization	0	7	13	29	14	10	18	1	1	1
Average Correlation Maximization	0	2	15	26	20	16	16	0	0	0
Exponentially Weighted Correlation Maximization	0	2	4	11	31	27	19	0	0	2
Sliding Exponentially Weighted Correlation Maximization	0	1	3	8	22	32	27	0	1	1
Neighbour Entropy Minimization	0	0	0	0	0	1	3	28	11	52
Average Entropy Minimization	0	0	0	0	0	1	4	44	33	12
Sliding Average Entropy Minimization	0	0	0	0	0	1	3	22	47	22
Global Range Alignment	2	31	29	13	7	5	5	0	1	0
Sub-integer range alignment	63	24	4	1	0	1	1	0	0	1

Table 5.4: The performance of the range alignment techniques presented in Chapter 3 on maritime data.

Table 5.4 shows the performance of the range bin alignment techniques when applied to the measured maritime data. The alignment was performed and the rankings were determined based on the quality measures of the aligned profiles. The results for each quality measure appear in the second section of Appendix F. The sub-integer range alignment algorithm is again used for the analysis of typical quality measure values obtained in properly aligned data.

5.2.2 Typical quality measure values

Histograms of the quality values calculated for data aligned using the sub-integer algorithm appear in Figure 5.6. The data was aligned in chunks of 0.5 seconds (roughly 61 profiles per chunk).

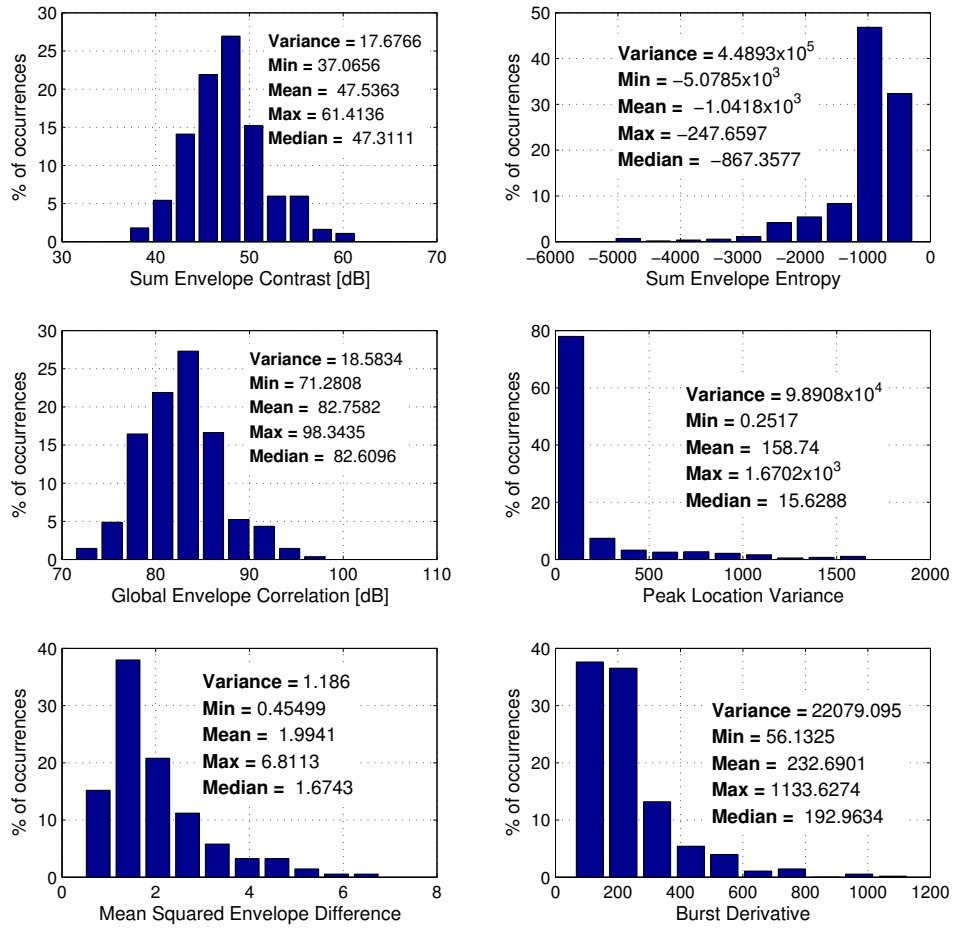

Figure 5.6: Typical quality values for aligned maritime data. The method used was the sub-integer alignment algorithm and the data aligned was 0.5 seconds long.

5.3 Summary

The difference in envelope magnitude values and the quality measures obtained from aligned[1] profiles presented in this chapter is summarised in Table 5.5. The difference between maritime and airborne data statistics presented is calculated by subtracting the airborne statistic from the maritime statistic and converting the result to a percentage using the sum of the statistics of both data sets.

[1] using the sub-integer range alignment algorithm

	% difference between maritime and airborne results									
	Min		Mean		Max		Median		Variance	
Measured envelope magnitude		14		36		60		20		78
Sum envelope contrast		98		68		62		78		88
Sum envelope entropy	-26		-36		-94		-42		-38	
Global envelope correlation		100		72		72		88		90
Peak location variance		100	-60			12	-94		22	
Mean squared envelope difference		78	-6		-44		-2		-58	
Burst derivative	-32		-48			78		94		38

Table 5.5: The difference between maritime and airborne data statistics. *Larger* values for the maritime statistics, compared to the airborne statistics, are shown in green and *smaller* values are indicated in red (or negative percentages).

The following conclusions can be made from the results in Table 5.5:

- The mean envelope magnitude of the maritime data is on average 36% larger than the aircraft data.
- The mean values for all the quality measures indicate improved results for the maritime data compared to the aircraft data.
- The most significant difference considering the mean values of the quality measures is the 72% improvement in global envelope contrast for the maritime data.

The difference in the results obtained from the airborne and marine target data sets is attributed to a wide selection of factors, discussed in the next chapter.

Chapter 6

Sensitivity Analysis and Recommendations for Quality Measures

The idealised data set shown in Figure 4.3, Chapter 4, is used to investigate the sensitivity of the various range bin quality measures to nonidealities in the data *after* alignment. This investigation will only attempt to recreate the resultant error to an acceptable degree of accuracy without adding any additional errors. The goal of this chapter is twofold: 1) to identify the *sensitivity trend* of the quality measure when exposed to different levels of severity of the errors and 2) to create a framework by which certain quality measures can be *recommended* as cost function for a range bin alignment technique in order to yield the best possible alignment result. In some instances, the modelling of the effects are beyond the scope of this study, so conclusions are drawn on isolated cases only.

Various factors produce problems in range alignment techniques. Two main groups of error sources can be identified:

- Effects caused by the target
- Effects caused by external factors

In order to identify which quality measure is more suited to a particular application, a first order investigation into the sensitivity of each measure to the commonly encountered errors is conducted.

6.1 Effects caused by the target

In many instances, the return from target of interest may exhibit characteristics that could cause difficulty in the range alignment process. These effects include:

- Scatterer Fluctuation Effects
- Platform/Target Vibration
- Micro-Doppler effects
- Target Rotation

6.1.1 Scatterer Fluctuation Effects

The received signal power from the target depends on the Radar Cross Section (RCS) of the target, which is an aspect angle and frequency dependent value. The RCS of any moving target may not be constant from one measurement to the next. This phenomenon is termed *fluctuation effects* and is caused by a large number of sources, including the target size, shape, dynamics and relative motion with respect to the radar [31].

The investigation of the influence of the target fluctuation on the various range bin alignment quality measures will make use of simplified target fluctuation modelling and the idealised data shown in Figure 4.3. The fluctuations are illustrated by applying a sinusoidal amplitude modulation to the range profile envelopes. An example of a simulated fluctuation appears in Figure 6.1.

Although the example of scatterer fluctuation shown in Figure 6.1 is overly simplified, it succeeds in displaying the scatterer fading effects found in actual data.

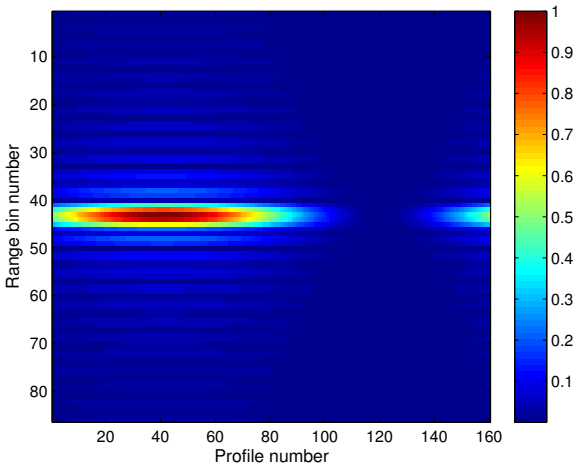

Figure 6.1: The target fluctuation investigated in this section is modelled as a sinusoidal amplitude modulation on the idealised data shown in Figure 4.3.

Note that this chapter is dedicated to investigating only the trends of the quality measures when exposed to varying degrees of severity of the nonidealities.

Sum Envelope Contrast

The first parameter analysed for sensitivity to fluctuations is the sum envelope contrast. This quality measure was introduced in Section 4.1.

Figure 6.2 shows the sum envelope contrast of the simulated version of the data when varying values of the fluctuation period are applied, normalised to the sum envelope contrast of the idealised data set shown in Figure 4.3.

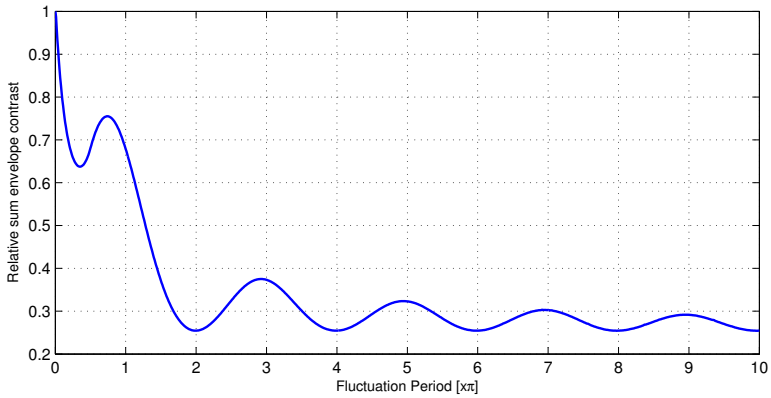

Figure 6.2: The relative sum envelope contrast is plotted for varying fluctuation period.

The relative sum envelope contrast shown in Figure 6.2 shows a peak at a fluctuation period of 0, which is equivalent to the nonfluctuating data shown in Figure 4.3. As expected, the maximum (or optimal) value corresponds to the value obtained for nonfluctuating data. The sum envelope contrast decreases as the fluctuation period increases up to the first local minimum at 0.35π. At 0.74π, it reaches a local maximum, after which the sum envelope contrast decreases until the fluctuation period is equal to 2π. The sum envelope contrast reaches local minima at fluctuation periods of integer multiples of 2π. Note that the oscillatory nature of the sum envelope contrast results from the varying contributions of the fluctuation introduced.

For scatterers that fade and reappear multiple times, as seen for fluctuation periods exceeding 2π, the relative sum envelope entropy varies around 0.3, which is 70% lower than the optimal value of 1. This indicates that the sum envelope entropy is moderately sensitive to scatterer fluctuations. If the fluctuation can be modelled by a single sine amplitude modulation with a period exceeding 2π, which causes the scatterer to fade and reappear, the loss in sum envelope contrast as opposed to the ideal data approaches 70%.

Sum Envelope Entropy

The influence of target fluctuations on the sum envelope entropy, which was used in quantifying the alignment quality in Chapter 3, is considered here.

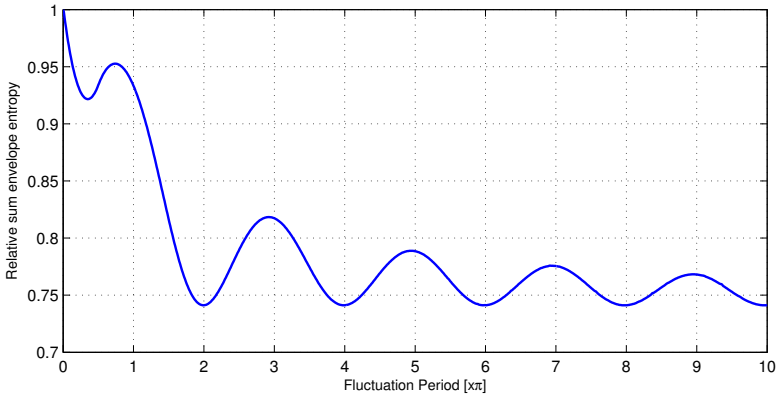

Figure 6.3: The relative sum envelope entropy is plotted for varying fluctuation period

The sum envelope entropy provides an oscillatory response to increases in fluctuation period, which settles around 77% of the value obtained for the ideal data in Figure 4.3. The reason for the decline in sum envelope entropy is the decreased sum envelope amplitude due to the inclusion of an increasing number of zeros due to the fluctuation of the scatterer. The sum envelope entropy is however considered a measure of the randomness of a function, which is related to the variance. The alterations in the sum envelope amplitude causes variations in the variance that follows the exact same trend as the sum envelope entropy shown in Figure 6.3.

Global Envelope Correlation

The global envelope correlation is defined in Section 4.3 based on the original derivation given in Wang [6]. Recall that a maximum global envelope correlation should indicate optimal alignment.

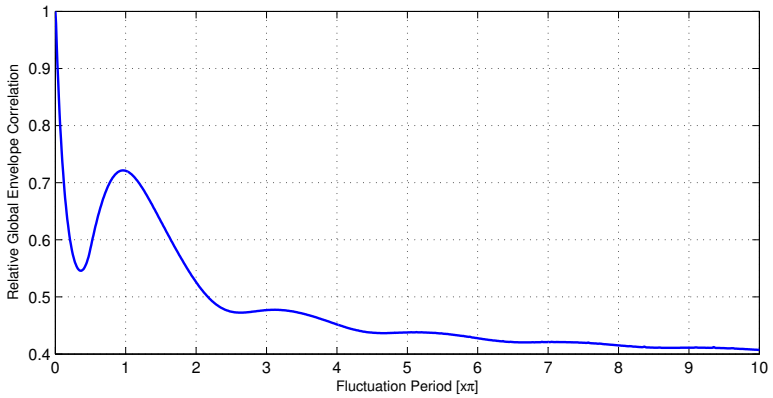

Figure 6.4: The relative global envelope correlation is plotted for varying fluctuation period.

The results shown in Figure 6.4 indicate that the optimal global envelope correlation is obtained for the nonfluctuating data shown in Figure 4.3. It rapidly decreases until 0.36π where a local minimum value is encountered. A local maximum is found at 0.96π where after the global envelope correlation decreases to between 40% and 50% of the optimal value with little sensitivity to increasing fluctuation period. If the scatterer fluctuation can be modelled by a sine wave as in this example, a decrease of 50% to 60% in the global envelope correlation can be expected for scatterers that fade and reappear due to fluctuation.

Variance of the peak location

The variance of the peak location is a very simplistic quality measure in the sense that it assumes the largest return (peak) in each profile is resulting from the single dominant scatterer present in the data.

The simulated result includes only a single scatterer, so the assumption is valid, but since the amplitude modulation is applied to the entire profile[1], no variation in the peak location occurs. The variance in the peak position when multiple scatterers occur is dependent on the positions, fluctuation and variance of each of the scatterers. This implies that the variance of the peak location is sensitive

[1] where the sinc response is assumed to have originated from a single scatterer

to scatterer fluctuations only if multiple scatterers are present, which negates the assumptions of this quality measure.

Envelope Mean Squared Difference

The mean squared difference was introduced in Section 4.5. In this analysis, the actual value of the mean squared difference is a function of the amplitude of the range profile, which is modulated with a sine wave with varying periods. The envelope mean squared difference is equal to zero in the ideal case shown in Figure 4.3.

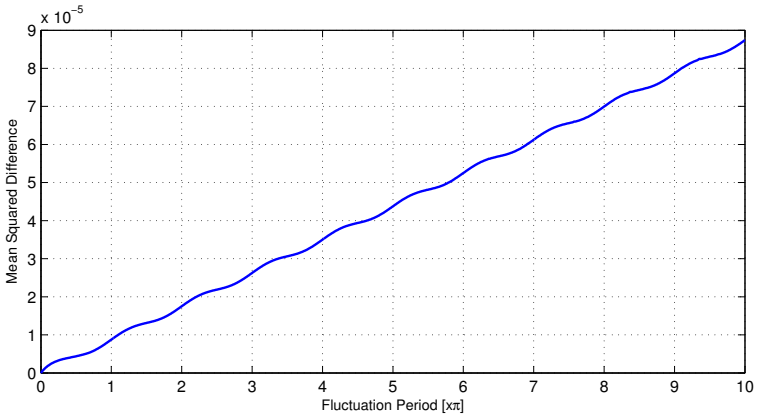

Figure 6.5: The mean squared difference is plotted for varying fluctuation period.

The mean squared difference for fluctuating scatterers appears in Figure 6.5. The value of the mean squared difference appear to be approximately linearly related to the fluctuation period. An increase in fluctuation period causes more abrupt changes from one profile to the next, which are summed to produce the result seen in Figure 6.5.

Burst Derivative

The burst derivative measure is an extension of the mean squared difference. The measure was introduced and discussed in Section 4.6.

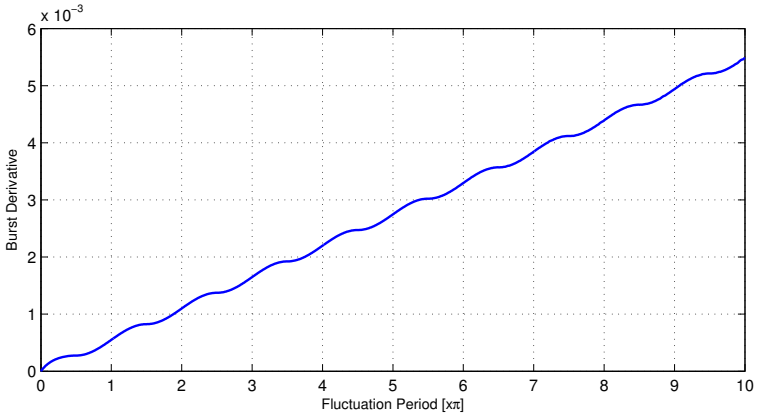

Figure 6.6: The burst derivative is plotted for varying fluctuation period.

The burst derivative for fluctuating scatterers appears in Figure 6.6. The value of the burst derivative is approximately linearly related to the fluctuation period. The cause of this effect is analogous to the findings for the sum envelope difference. An increase in fluctuation period causes more abrupt changes from one profile to the next, which are summed to produce the result seen in Figure 6.6.

6.1.2 Platform/Target Vibration

Platform/Target vibration is commonly found when either or both the target and the platform are airborne due to the light weight of the aircraft and the effect of the engines.

A very simple sinusoidal model is used to illustrate the effect of vibration on the range bin alignment quality measures. The amplitude, A_v, of the sinusoid will determine the number of range bins shifts between profiles as a result of the vibration and the period, τ_v, determines the time elapsed before the sinusoidal cycle is repeated. Due to the nature of this investigation, τ_v will be expressed in terms of *range profiles*.[2]. An example of simulated vibration on the hypothetical data shown in Figure 4.3 is displayed in Figure 6.7. For the example, the

[2]The number of profiles that are influenced by a *single* vibration cycle

vibration amplitude applied is $A_v = 0.05$ bins and the period is $\tau_v = 5$ profiles.

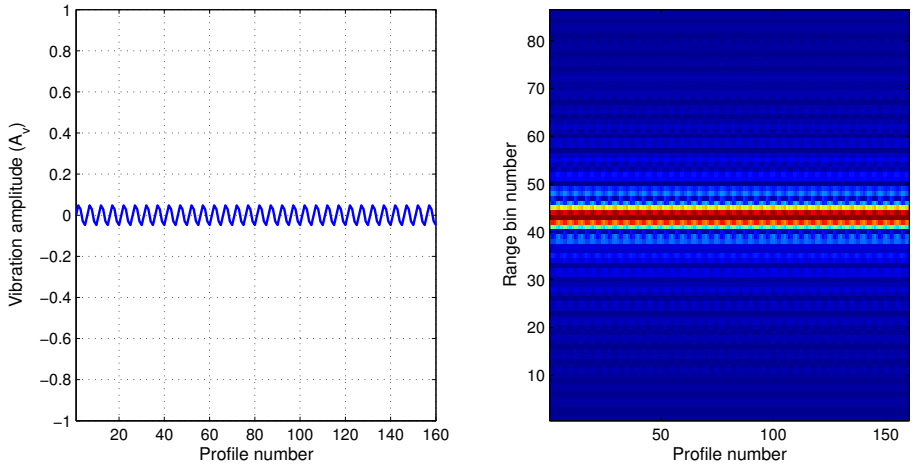

Figure 6.7: Simulated vibration data generated using a vibration period τ_v=5 profiles and amplitude A_v=0.05 bins.

The nature of the vibration is dictated by both the amplitude and period of the sinusoid. To this end, a two-dimensional parametric sweep of these values is conducted to investigate the quality measure trends associated with target/platform vibration. The amplitude sweep included values of $0 \leq A_v \leq 1$ (range bins) and the period was swept over $5 \leq \tau_v \leq M/2$ (profiles), where M denotes the total number of range profiles in the data.

Sum Envelope Contrast

The sum envelope contrast, introduced in Section 4.1 is considered first. The results for varying vibration amplitudes and periods appear in Figure 6.8.

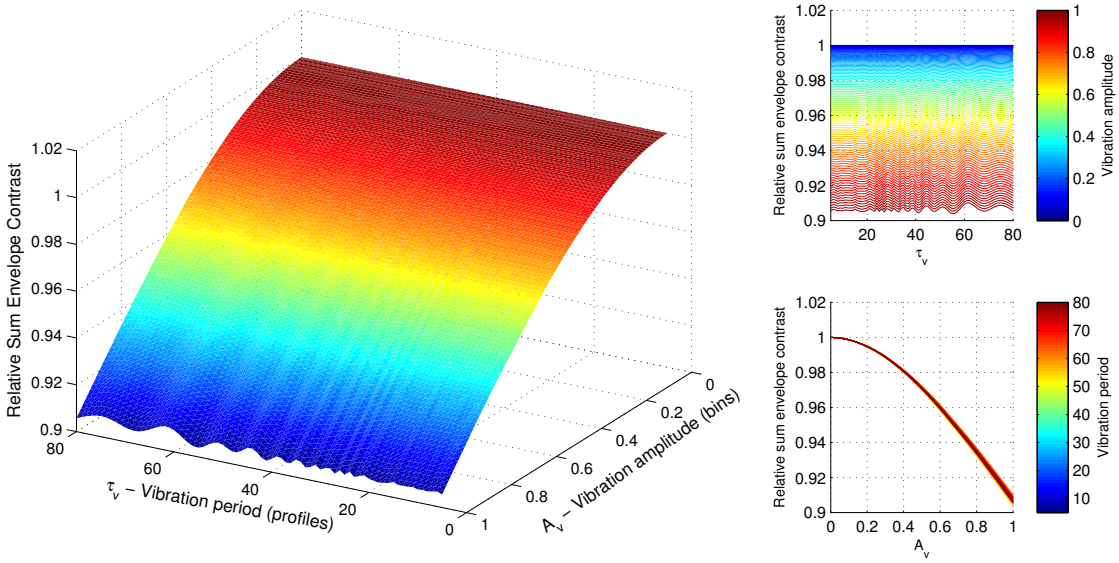

Figure 6.8: The relative sum envelope contrast is plotted for varying vibration amplitudes, A_v, and periods, τ_v.

It can be seen from Figure 6.8 that the sum envelope contrast of the entire aligned profile is not significantly sensitive to changes in the vibration period. This may be attributed to the fact that the summed envelope of the data is used, which causes the time period that the change occurs less relevant.

The sum envelope contrast indicates a Gaussian-like relationship to the amplitude of the vibration, decreasing as the amplitude increases. The minimum contrast value encountered here is around 0.90, which indicates a 10% deviation from the optimal contrast value. Large vibration amplitudes causes more severe misalignment between profiles, so the decrease in contrast is an expected result.

Sum Envelope Entropy

As with the sum envelope contrast, the sum envelope entropy is calculated using the sum envelope. Recall that smaller values of entropy are assumed to indicate improved alignment.

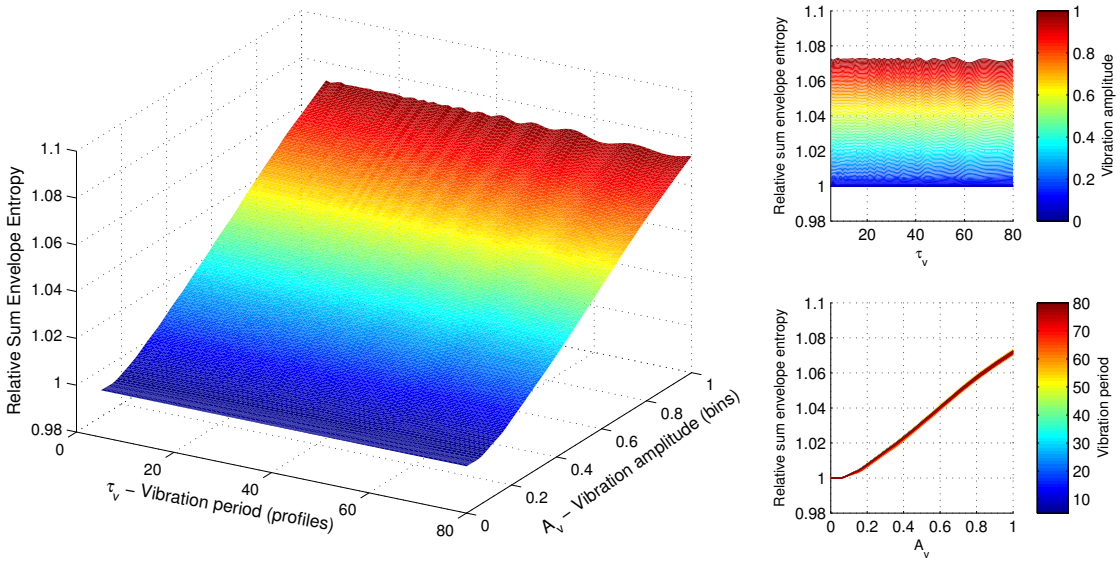

Figure 6.9: The relative sum envelope entropy is plotted for varying vibration amplitudes, A_v, and periods, τ_v.

As seen in the analysis of the sum envelope contrast, the sum envelope entropy is also not sensitive to changes in the vibration period. This is an expected result, since the sum envelope is again used in the calculation of this performance measure. The sum envelope entropy presents an approximately linear relationship to the vibration amplitude, increasing as the amplitude increases. The increase in vibration amplitude increases the misalignment between profiles, which is correctly indicated by the increase in entropy. The entropy increases by approximately 7% when exposed to a vibration amplitude of 1 range bin, compared to the optimal value of 0 when no vibration is encountered.

Global Envelope Correlation

The global envelope correlation provides another measure of quantifying the similarity of profiles in aligned data. The measure was introduced in Section 4.3 and larger values were assumed to indicate improved alignment.

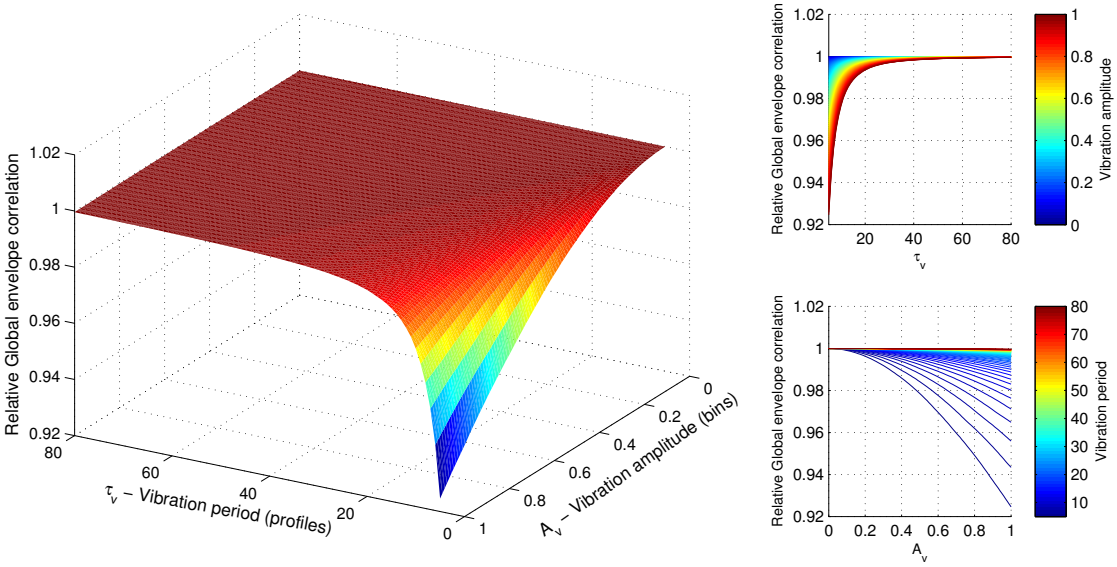

Figure 6.10: The relative global envelope correlation is plotted for varying vibration amplitudes, A_v, and periods, τ_v.

The result shown in Figure 6.10 indicates that the global envelope correlation is not severely sensitive to scatter vibration. It worst result obtained occurs at low vibration period and high vibration amplitude and is 8% lower than the optimal value. Since the vibration amplitude is implemented to not exceed one range bin shift, the similarity between adjacent profiles is not significantly degraded in the presence of vibration.

Variance of the peak location

The variance of the peaks location, introduced in Section 4.4, for varying vibration circumstances is analysed here.

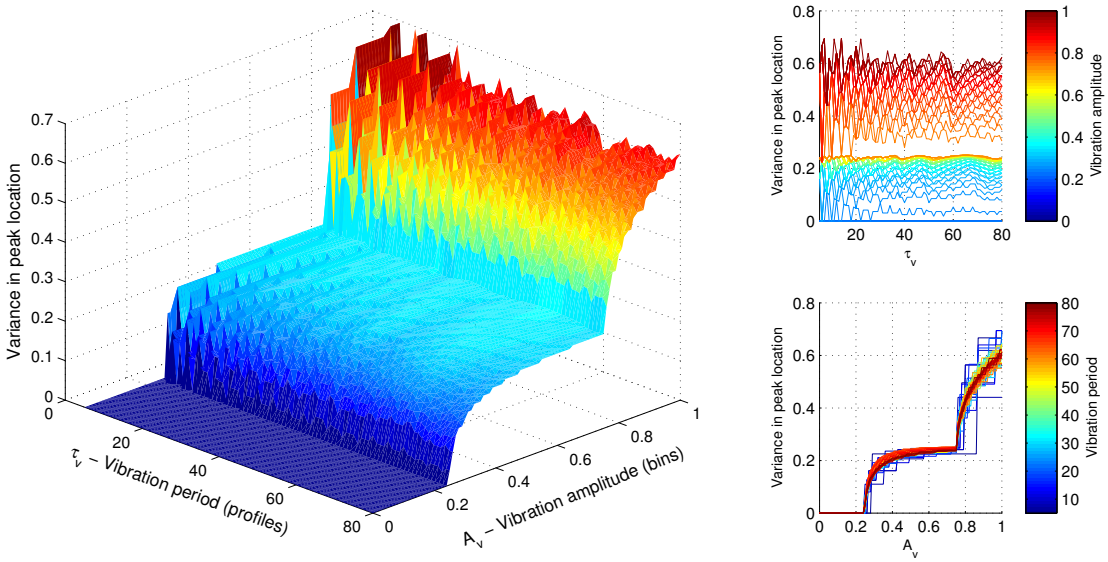

Figure 6.11: The variance of the peak location is plotted for varying vibration amplitudes, A_v, and periods, τ_v.

The optimal peaks location variance is zero. The results shown in Figure 6.11 indicates little variation in the peaks location. The total variance incurred for all instances of target vibration simulated here is small and therefore the variance in the peak location is considered insensitive to target vibration.

Envelope Mean Squared Difference

The sensitivity of the envelope mean squared difference, presented in Section 4.5, to scatterer vibration effects is analysed in this section.

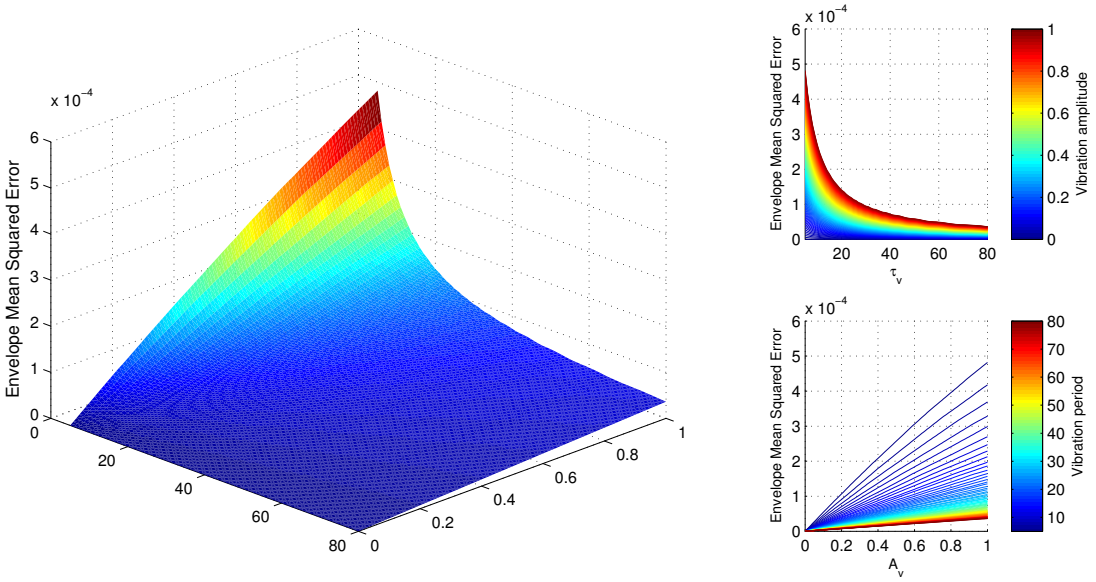

Figure 6.12: The mean squared difference is plotted for varying vibration amplitudes, A_v, and periods, τ_v.

The result in Figure 6.12 indicate that the mean squared difference value increases approximately linearly with vibration amplitude and decreases with increasing vibration period. The mean squared difference value is more sensitive to changes in the vibration amplitude, which dictates the similarity between adjacent profiles and hence lead to increased mean squared difference values. The effect of the vibration period on the mean squared difference is related to the rate of change of the adjacent profiles. Large periods imply slowly changing differences between adjacent profiles, which leads to a small effect overall.

Burst Derivative

The burst derivative was introduced in Section 4.6. The results obtained for varying scatterer vibration simulations appear in Figure 6.13.

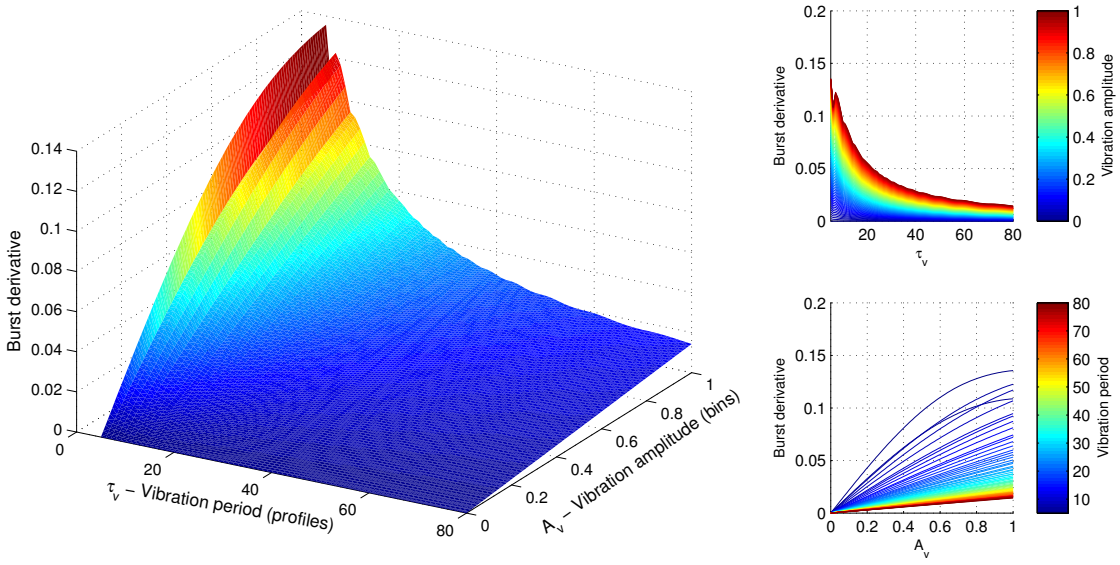

Figure 6.13: The burst derivative is plotted for varying vibration amplitudes, A_v, and periods, τ_v.

Figure 6.13 indicates a decrease in burst derivative with increased vibration period, which can be expected since larger vibration periods produces less variation between adjacent profiles. The effect of target vibration on the burst derivative is similar to the findings for the mean squared difference, as these values are closely related. The decrease in burst derivative with increasing vibration period can be expected since the derivative between adjacent profiles changes slowly, producing a low burst derivative value. The increase in burst derivative with vibration amplitude is also expected because increased vibration amplitude adds to the dissimilarity between adjacent profiles and produces a higher burst derivative value.

6.1.3 Micro-Doppler effects

Micro-Doppler modulation results from the return from rotating, vibrating or moving parts on a target of interest. A common source of micro-Doppler modulation is aircraft rotor blades. As a result, micro-Doppler modulation is more

commonly found in aircraft data. The modelling of micro-Doppler effects in high range resolution radar data is beyond the scope of this research, so the effects on the quality measures will not be quantified.

6.1.4 Target Rotation

The target rotation is simulated by applying a sinusoidal range bin shift to a scaled copy of the idealised data shown in 4.3, the sum of the shifted data and the ideal data forms the simulated result of a dominant scatterer with a rotating smaller scatterer. An example of the simulated data appears in Figure 6.14.

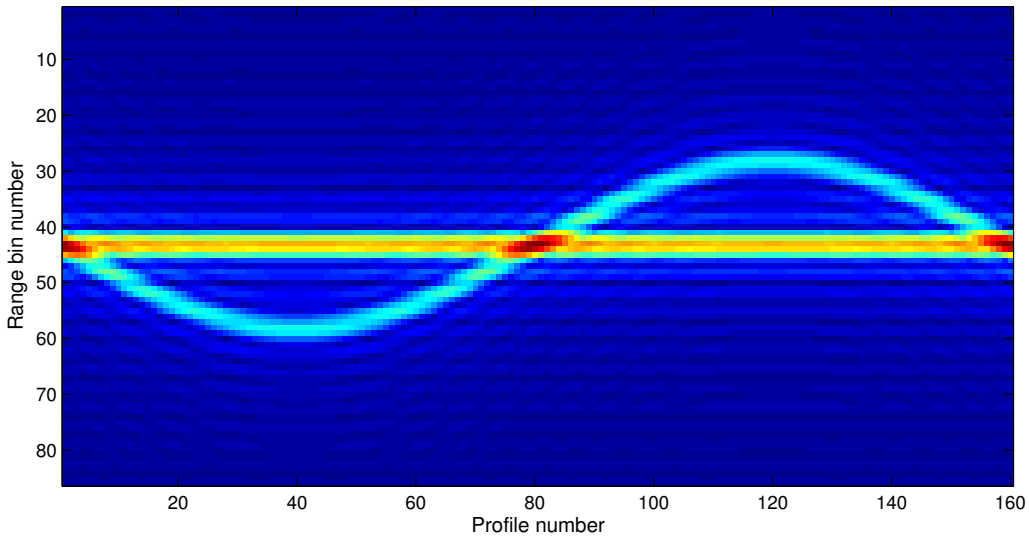

Figure 6.14: The target rotation effects were simulated by applying a sinusoidal shifting function to a scaled copy of the idealised data shown in Figure 4.3.

The amplitude of the sinusoidal rotation will be considered the measure of "severity" of the rotation incurred, which is related to the relative distance between the dominant scatterer and the rotating scatterer. A larger distance would cause a larger displacement of the secondary scatterer. Note that the example in Figure 6.14 is perfectly aligned according to the translational motion of the dominant scatterer. The analysis aims at identifying the trend in changes in the quality measures as a result of the added rotating scatterer.

Sum Envelope Contrast

The sum envelope contrast, introduced in Section 4.1, is the first quality measure analysed for sensitivity to target rotation effects. Figure 6.15 shows the results of the investigation.

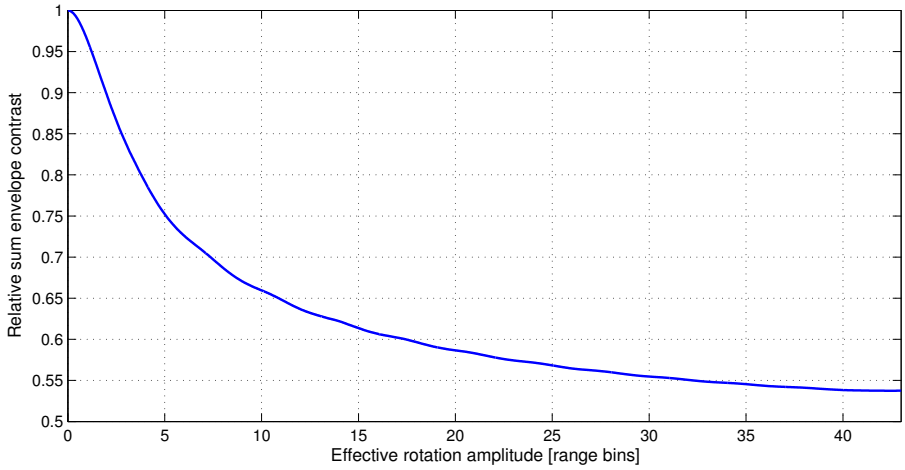

Figure 6.15: The relative sum envelope contrast is plotted for varying values of the effective rotation "amplitude".

The sum envelope contrast shown in Figure 6.15 was normalised to the ideal return were no rotation is incurred, at zero effective rotation amplitude. The sum envelope entropy decreases at a decreasing rate to around 55% of the optimal value when severe rotation is encountered. The maximum rotation amplitude allowed was half the total number of range bins. This limit was chosen so as to not allow wrapping of the rotating scatterer in the profile.

Sum Envelope Entropy

The sum envelope entropy was used to quantify the alignment of the measured data analysed in Chapter 3. More details on the derivation and calculation of this measure appears in Section 4.2. The sum envelope entropy for varying values of the effective rotation amplitude appears in Figure 6.16.

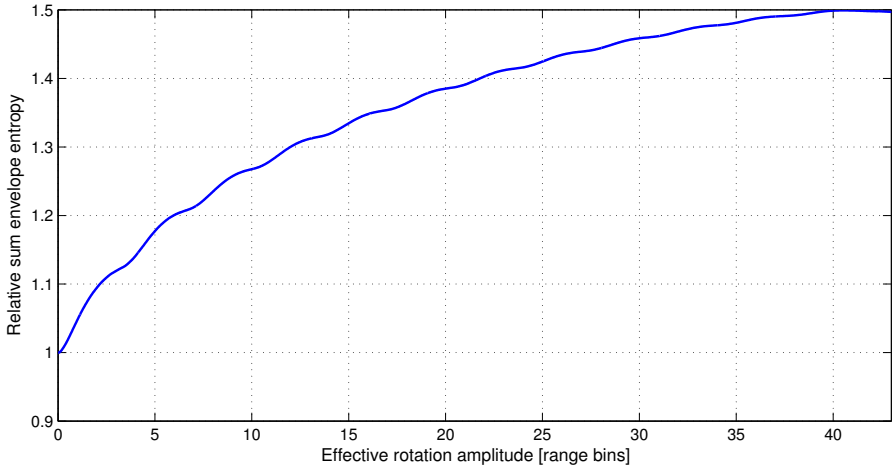

Figure 6.16: The relative sum envelope entropy is plotted for varying values of the effective rotation "amplitude".

As in the previous section, the sum envelope entropy shown in Figure 6.16 is normalised with the ideal return of a nonrotating target. The sum envelope entropy escalates at a rate that decreases as the effective rotation amplitude increases. For the rotation limits incurred, the sum envelope entropy reaches a value 50% larger than the optimal value. Recall that large sum envelope entropy values are indicative of misalignment between profiles.

Global Envelope Correlation

The global envelope correlation was introduced in Section 4.3. The results obtained for varying rotation amplitudes are given in Figure 6.17.

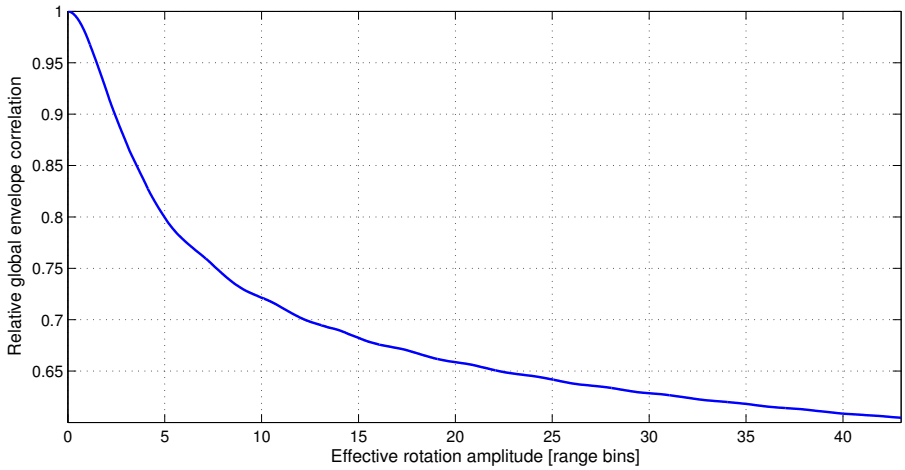

Figure 6.17: The relative global envelope correlation is plotted for varying values of the effective rotation "amplitude".

The result shown in Figure 6.17 is normalised to the first value, or zero rotation amplitude. The trend in the global envelope correlation with increasing rotation amplitude is similar to the trend found with the sum envelope contrast investigation, shown in Figure 6.15. The global envelope correlation reaches close to 60% of the optimal value for the maximum rotation in this investigation. This finding may indicate that it is slightly less sensitive to target rotation when compared to the sum envelope contrast.

Variance of the peaks location

The variance of the peaks location in the aligned profiles was introduced in Section 4.4. The results for analysing the effect of target rotation on the value of the variance is seen in Figure 6.18.

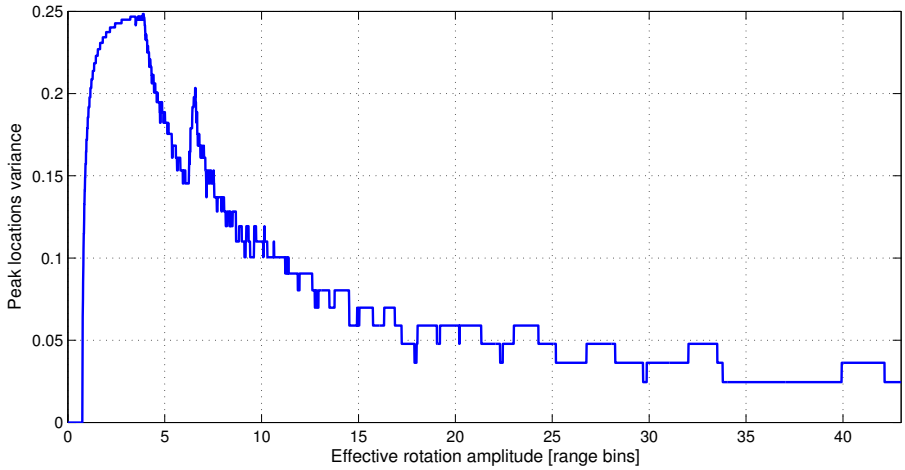

Figure 6.18: The variance of the peaks location is plotted for varying values of the effective rotation "amplitude".

The simulated rotating scatterer was implemented to return half the energy of the dominant scatterer, so it would be expected that the peak remains centred in the profile, with small variance. The overlapping of the returns from the dominant and the rotating scatterers causes constructive interference that may lead to larger peaks that are not perfectly centred on all profiles, which occurs for longer periods at small rotation amplitudes. This also explains the small sensitivity seen in Figure 6.18 for large rotation amplitudes. It should be noted that severe fluctuations in the variance of the peaks location may exist when multiple dominant scatterers with similar amplitude returns are present.

Mean Squared Difference

The mean squared difference as presented in Section 4.5 provides an indication of the similarity between adjacent profiles in the data. The results obtained for the target rotation study appears in Figure 6.19.

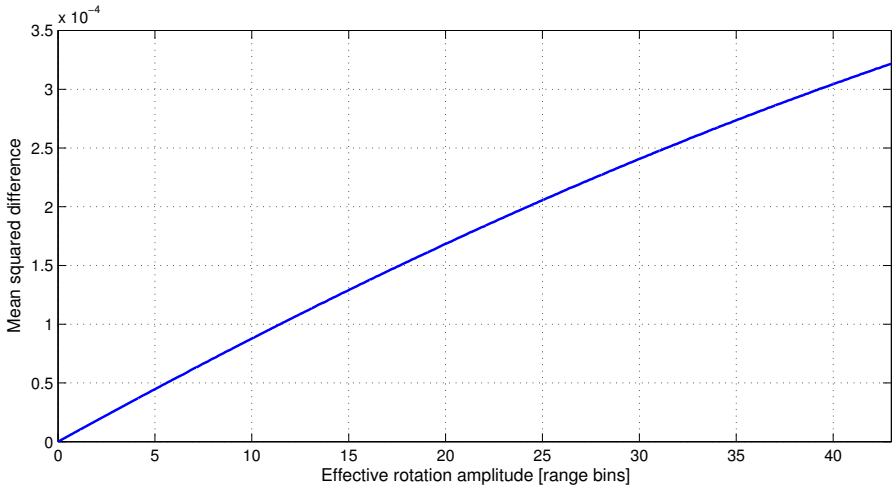

Figure 6.19: The relative mean squared error is plotted for varying values of the effective rotation "amplitude".

Figure 6.19 indicates that the mean squared difference increases with the effective rotation amplitude. This result is expected, since the larger rotation amplitudes causes higher dissimilarity between adjacent profiles, and a higher sum of differences. Note that the exact values shown in Figure 6.19 is related to the amplitudes of the profiles and is not normalised, since the optimal value is zero.

Burst Derivative

The burst derivative was introduced in Section 4.6 and is related to the mean squared difference in the sense that it considers difference measures between profiles in the calculation. The result for varying the rotation amplitude appears in Figure 6.20.

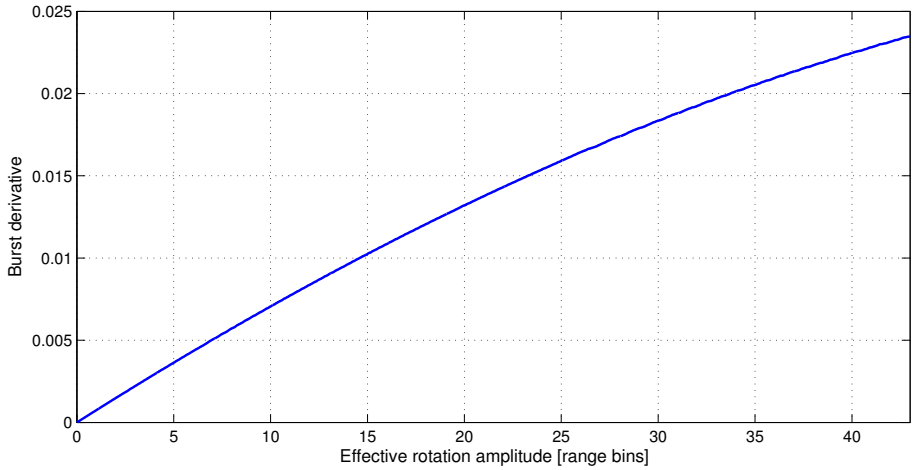

Figure 6.20: The burst derivative is plotted for varying values of the effective rotation "amplitude".

The burst derivative values increases approximately linearly with the effective rotation amplitude. Again, the values shown in Figure 6.20 is related to the profile amplitudes and is not normalised since the optimal value is zero.

6.2 Effects caused by external factors

In the radar operating environment, many factors may influence the target return. Although many of these effects can be mitigated through intelligent processing, no guarantee can be given that the effect has been completely eliminated from the data. These effects include:

- Noise
- Clutter Effects

6.2.1 Effect of Noise

The noise used for investigating the typical trends that can be expected in the various quality measures is *additive zero mean white Gaussian noise*. The noise is

also assumed to be uncorrelated. Additional information regarding the statistical properties of the simulated Gaussian noise is given in Appendix H. The amplitude of the noise was chosen to vary between[3] 0 and 1 and the noise variance was chosen as 0.2. The result appears in Figure 6.21.

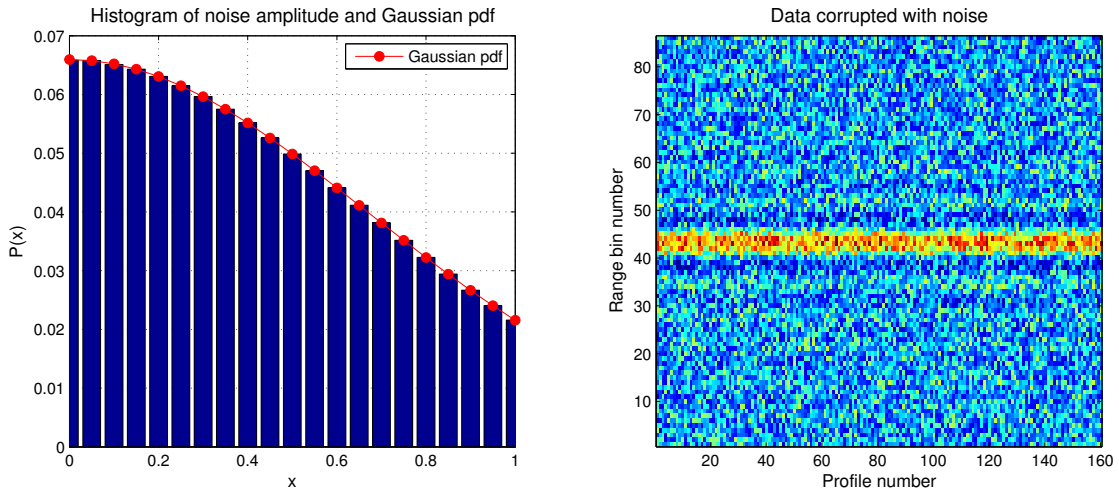

Figure 6.21: The probability density function (or histogram) of the simulated noise-corrupted data appears on the left. The simulated data is shown on the right. The amplitude of the noise has a maximum value of 1 and $\sigma_x^2 = 0.2$.

A parametric sweep of the noise variance, σ_x^2, is used for analysing the behaviour of the quality parameters.

Sum Envelope Contrast

The sensitivity of the sum envelope contrast, introduced in Section 4.1, to additive Gaussian noise is investigated in this section.

[3]This choice of noise amplitude allows for a minimum signal-to-noise ratio of 0 dB.

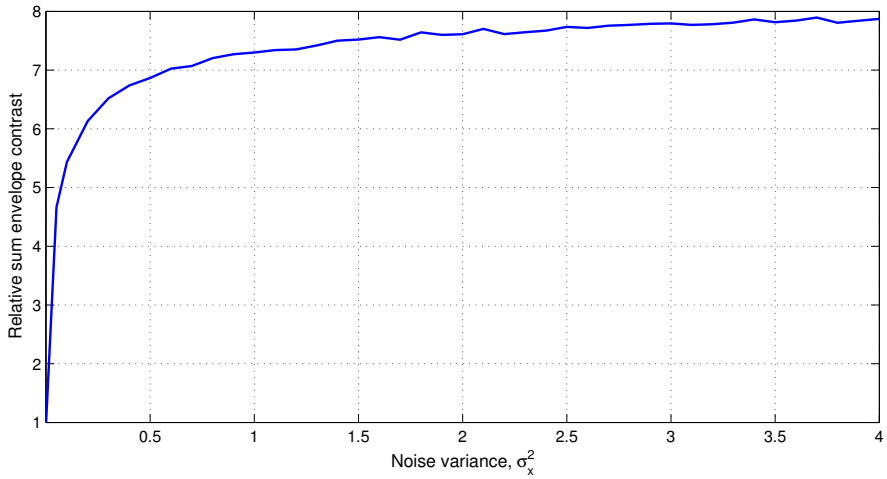

Figure 6.22: The relative sum envelope contrast is plotted for varying values of the noise variance, σ_x^2.

The results in Figure 6.22, normalised to noiseless data, indicate an increase in sum envelope contrast when the data is corrupted with noise of higher variance σ_x^2. The rate of change of the sum envelope contrast decreases for larger values of σ_x^2, and seems to approach a limit around 8. This result indicates that the sum envelope contrast is sensitive to the addition of noise, but presents and *improved* result for noisy data compared to ideal data.

Sum Envelope Entropy

The sum envelope entropy was introduced in Section 4.2. The sensitivity of this measure to additive Gaussian noise is investigated next.

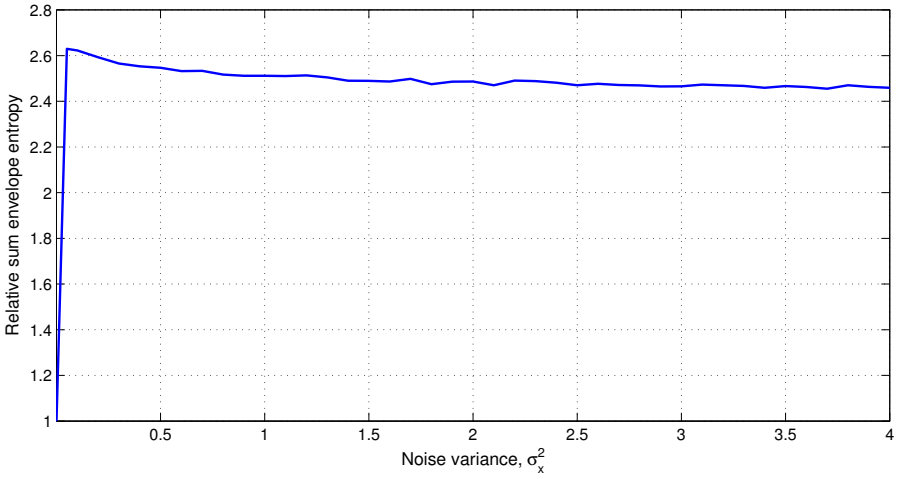

Figure 6.23: The relative sum envelope entropy is plotted for varying values of the noise variance, σ_x^2.

Figure 6.23 shows the sum envelope entropy of simulated noisy data, normalised to noiseless data. The sum envelope entropy rapidly increases up to a value around $\sigma_x^2 = 0.1$, reaches a slight peak and then descends slowly to settle around 2.4 times the optimal value. Since the noise is Gaussian, the entropy of the noise only is related to the variance by the relation[4] $H_{noise} = \ln \sqrt{\sigma_x^2 2\pi e}$. The addition of the noise causes an increase in sum envelope entropy that is insensitive to changes in noise variance.

Global Envelope Correlation

The global envelope correlation, introduced in Section 4.3, calculated for data sets that contain Gaussian noise with varying variances, is presented in this section.

[4]See Appendix A for full derivation of this relationship.

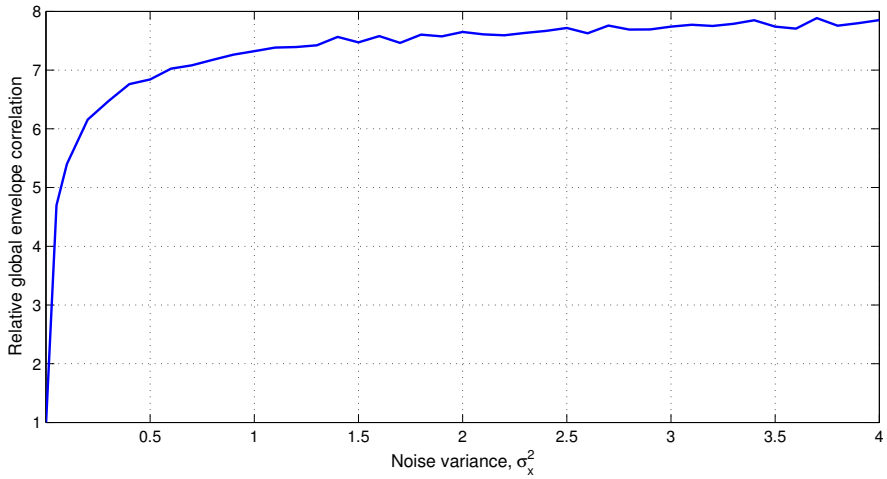

Figure 6.24: The relative global envelope correlation is plotted for varying values of the noise variance, σ_x^2.

Increases in the noise variance causes an increase in the global envelope correlation, very similar to the result found for the sum envelope contrast in Figure 6.22. For large noise variance values, the global envelope correlation settles around a value of 8. The addition of noise provides an improved global envelope correlation which is not very sensitive to the noise variance, particularly at larger values.

Variance of the peak location

The introduction to the variance of the peak location was presented in Section 4.4.

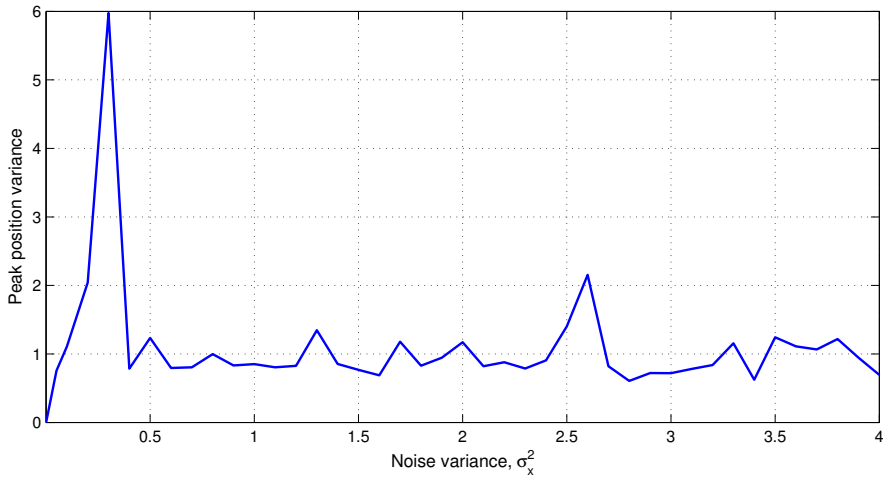

Figure 6.25: The variance of the peak locations is plotted for varying values of the noise variance, σ_x^2.

The peak location variance for noisy data is offset by almost 1 compared to the ideal result of 0. Isolated instances exist where large variances occur, which appears to be independent of the noise variance. The variance of the peak location is not considered highly sensitive to noise simulated in this study. Noise with higher power may not produce similar findings to that presented here.

Envelope Mean Squared Difference

The envelope mean squared difference is considered here. The measure was introduced in Section 4.5.

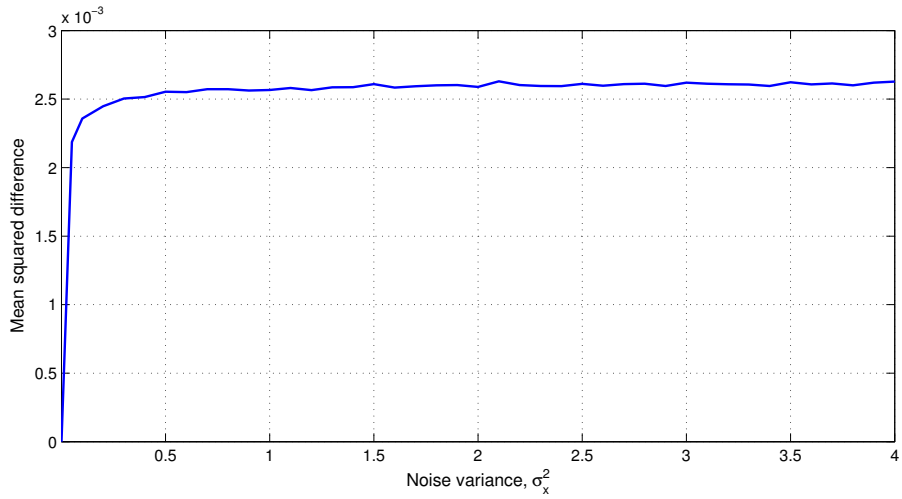

Figure 6.26: The normalised mean squared difference is plotted for varying values of the noise variance, σ_x^2.

The results shown in Figure 6.26 is not normalised and the values are dependent on the amplitude of the data. The envelope mean squared difference increases very sharply with the noise variance up to around 6, after which it slowly settles to a values around 7. Using the mean squared difference as quality measure for noisy data may produce a result that is 7 times "worse" compared to the noiseless case. The measure is not sensitive to increases in the noise variance exceeding 1.

Burst Derivative

The burst derivative provides another measure of similarity between profiles to quantify the alignment quality. The measure was introduced and discussed in Section 4.6.

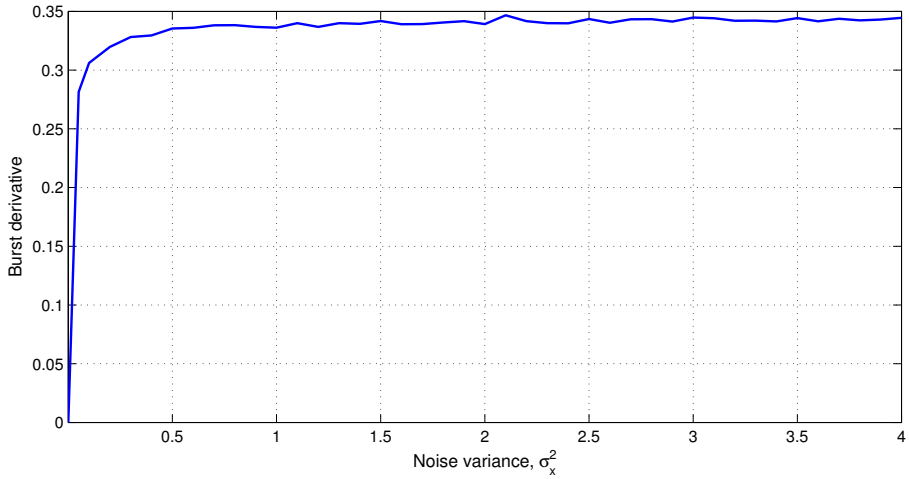

Figure 6.27: The burst derivative is plotted for varying values of the noise variance, σ_x^2.

The trend seen in Figure 4.6 is practically identical to that seen for the mean squared difference in Figure 6.26. Depending on the noise power, the burst derivative may be slightly increased by the addition of noise. The burst derivative value is however not sensitive to noise with variances that exceed 1.

6.2.2 Clutter Effects

The effect of clutter in a range profile on the quality measure for range bin alignment relies heavily on the type of clutter. Various types of clutter exist, where sea clutter, atmospheric clutter and ground clutter can be linked to the measurement environment. Clutter is generally considered to be coherent, with fluctuating properties. Clutter cancellation and mapping techniques have been developed to limit the clutter in a measurement. These include [32]:

- antenna spatial (angular) selectivity
- range discrimination (temporal separation)
- velocity discrimination (Doppler filtering)

Modelling of various types of clutter is beyond the scope of this study. The effect of the clutter on the quality measures of the aligned profiles is dependent on the type, location and intensity of the clutter. When quantifying the quality of alignment in data containing significant clutter, it is advisable to isolate and consider the influence of the clutter before conclusions are drawn.

6.3 Quality Measure Calculation

The statistics of the unaligned data typically change with time as the orientation and speed of the target change. This implies that the quality measures will also vary depending on which sections of the data were used in the calculation.

6.3.1 Number of Profiles

The number of profiles used in the calculation of a quality measure may be varied according to the statistics of the data. The number of profiles to use for alignment should be a function of the rotation rate of the target.

6.3.2 Normalisation of Profiles

The normalisation of profiles, particularly profiles containing deep nulls or very large bit errors need careful consideration as these extremes have an equally extreme influence on the quality measure. Proper pre-processing of the data should include checks to isolate and remove the influence of these samples.

Another option is to consider the quality measures over sections of the data using a sliding window approach to check for unusual outliers in the result that may be indicative of a deep zero or large bit error.

6.4 Summary

The sensitivity of various quality measures to a selection of data nonidealities were investigated. Since this chapter dealt exclusively with simplified simulated data, the exact values shown in Table 6.1 are only valid under the assumptions of the simulation models and should be used as guideline only.

The convention used in Table 6.1 is as follows:

x	-	value not investigated since it is dependent on multiple parameters of the target/external effect
xx	-	value not investigated since the addition of the target/external effect negates the assumptions required by the calculation of the quality measure
H	-	Highly influenced by the presence of the target/external effect
M	-	Moderately influenced by the presence of the target/external effect
L	-	Presence of the target/external effect has little or no effect on the measure
+	-	Presence of the target/external effect causes the quality measure to indicate an *improvement* in alignment quality
-	-	Presence of the target/external effect causes the quality measure to indicate a *decline* in alignment quality
(v)	-	Indicates that the quality measure varies significantly with increased target/external influence intensity

Quality Measure	**Target Effects**				**External Effects**	
	Scatterer Fluctuation	Platform/Target Vibration	Micro-Doppler effects	Target Rotation	Noise	Clutter
Sum envelope contrast	H(v) -	L -	x	M -	H+	x
Sum envelope entropy	H(v)+	L -	x	M -	H -	x
Global envelope correlation	H -	L -	x	M -	H -	x
Variance of the peak location	xx	L -	x	L -	L(v) -	x
Mean squared envelope difference	L(v) -	H(v) -	x	M(v) -	M(v) -	x
Burst derivative	L(v) -	H(v) -	x	M(v) -	M(v) -	x

Table 6.1: A summary of the sensitivity of all studied quality measures to common error-causing effects found in radar data.

The results in Table 6.1 provide a guideline for selecting quality measures that most accurately quantify the *alignment quality* without significant degradation from nonidealities in the data[5].

[5]Provided that the assumptions made in each simulation are applicable to the data

Chapter 7

Mitigation of range bin alignment errors caused by algorithm parameters

A selection of the errors listed in Section 3.8, Chapter 3 are a direct consequence of the methods and parameters used in the algorithm.

Errors and causes for error commonly found in range bin alignment include:

- Error Accumulation
- Integer Range Bin Shifts
- Limited Target Manoeuvrability

This chapter presents methods of mitigating or minimizing the impact of the errors on the aligned result.

7.1 Error Accumulation

The error accumulation problem found in range bin alignment techniques occurs when *adjacent* profiles are compared in order to find the optimal alignment between the two, based on a parameter such as correlation, contrast or entropy. Making use of a sliding window with insufficient length may also lead to the error accumulation effect.

Since the error accumulation effect mostly occurs in methods that use adjacent profiles shifted by at most *integer* shifts, it is assumed that the error accumulation does not result in a range bin shift exceeding *one bin* from one profile to the next. To simulate the error accumulation effect, a linear phase ramp is applied to the idealised data shown in Figure 4.3, Chapter 4. The resulting shift value represents the error accumulation.

An analysis of the sensitivity of the various quality measures on the error accumulation effect appears in Appendix I. Table 7.1 provides a summary of the findings in terms of the possible quality improvement if the error accumulation problem is mitigated.

Quality Measure	**Maximum improvement**
Sum envelope contrast	80%
Sum envelope entropy	67%
Global envelope correlation	11%
Variance of the peak location	760
Envelope mean squared difference	7.2×10^{-3}
Burst derivative	0.16

Table 7.1: Findings of the sensitivity analysis of error accumulation on various alignment quality measures. The full analysis and all plots are given in Appendix I.

The effect of error accumulation is a misalignment of profiles and Table 7.1 provides values for the maximum possible improvement in the quality measure values that can be achieved if the error accumulation effect is eliminated. Mitigation of the error accumulation effect will also cause an improvement in the achievable quality measure values.

Ways of mitigating the error accumulation effect involve making use of multiple aligned range profiles as the reference profile. The number of profiles to use is dependent on the data. For instance, aligning data with highly fluctuating scatterers may need a form of weighting or "forgetting factor" to increase the adaptability of the algorithm to the changing amplitude of the dominant scatterers in the data.

A special case of the forgetting factor is to discard a certain number of previously aligned profiles, which renders a sliding window for estimating the range bin shifts from one profile to the next. The forgetting factor can then be thought of as a low pass filter with a very sharp cutoff. Another option is to use exponential weighting of profiles to limit, but still include, contributions of older profiles on the quality measure.

7.2 Integer Range Bin Shifts

All alignment algorithms must make use of shifting of profiles in order to achieve alignment. If the shifting is achieved using multiplication by a phase ramp in the frequency domain, sub-integer shifts can be achieved. The resolution of the applied phase ramp can be set by the user and offers a trade off between alignment accuracy and computational load.

7.3 Limited Target Manoeuvrability

The problem of limited target manoeuvrability is a constraint that is presented by some alignment techniques and is independent of the statistics of the data. The effect of limited target manoeuvrability ultimately leads to a misalignment of range profiles after applying the alignment technique. The most common limitation on target manoeuvrability is the condition that the target must have a *linear radial velocity*. In most practical cases, particularly with fast moving targets such as aircraft, this assumption can only be approximated by applying

the alignment technique to groups of fewer profiles per group and then collating the results.

The extent of the alignment error produced due to the limited allowed target manoeuvrability is dependent on the alignment technique used as well as the radial motion of the target with respect to the radar. Due to the large number of contributing factors to these errors, modelling and quantifying the resulting influence on the range bin alignment quality measures is regarded unfeasible.

Chapter 8

Conclusions

The first problem investigated in this study was understanding the purpose of range bin alignment. Range bin alignment constitutes the first step in non-parametric motion compensation for ISAR imaging. The background context was provided in Chapter 2.

8.1 Range Bin Alignment Techniques

This study included the implementation and analysis of classic and state-of-the art range bin alignment algorithms. In terms of their implementation strategies, the algorithms can be identified as *parametric* or *non-parametric* techniques.

The parametric techniques included in this study were the Hough transform method (see Section 3.6) and the global method (see Section 3.7). The Hough transform method can be implemented in data where the target translational velocity is constant throughout the processing time. The global method assumes that the target does not accelerate radially with respect to the radar for the duration of the processing time. Both these assumptions place limitations on the robustness of the algorithms when applied to data of various manoeuvring targets.

8.2 Quality Measures for Range Bin Alignment

Five alignment quality measures were identified and discussed in Chapter 4. The quality measures are used in quantifying the quality of range bin alignment achieved as well as the cost function of the optimisation problem of finding the optimal shift required for alignment.

8.3 Sensitivity Analysis and Recommendations for Quality Measures

Chapter 6 provided simulated analyses of the effect of various nonideal data phenomena on the quality parameters. The nonidealities included target and external effects. It was found that the quality measures have varying sensitivity to the nonidealities, which indicate that some measures may be more suited to particular data sets. A table in Section 6.4 summarised the findings of the sensitivity analysis by assigning a level of sensitivity to each simulation for every quality measure. This table may be consulted when selecting the cost function and/or quality measure in range alignment algorithm design.

8.4 Mitigation of range bin alignment errors

Chapter 7 presented simple procedures for mitigating or minimizing the effect of alignment errors caused by the limitations of the algorithm. The chapter addresses error accumulation, integer range bin shifts as well as the target manoeuvrability limitations. In range alignment algorithm design, these factors may influence the performance of the algorithm and need to be considered.

Chapter 9

Recommendations

Since radar imaging is a widely studied field with many applications, any contribution to the improvement of the image formation process is worth pursuing. The work presented in this dissertation presented many avenues for continued research in range bin alignment for ISAR image formation.

9.1 Design framework for alignment algorithm design

Chapter 3 presented seven range bin alignment algorithms that are considered to range from elementary (peak alignment) to state of the art (sub-bin technique [16]). The knowledge gained from this analysis may be applied to creating a *design framework* for designing an alignment algorithm optimally designed for a particular data quality.

A general framework for non-parametric techniques is provided in Figure 9.1.

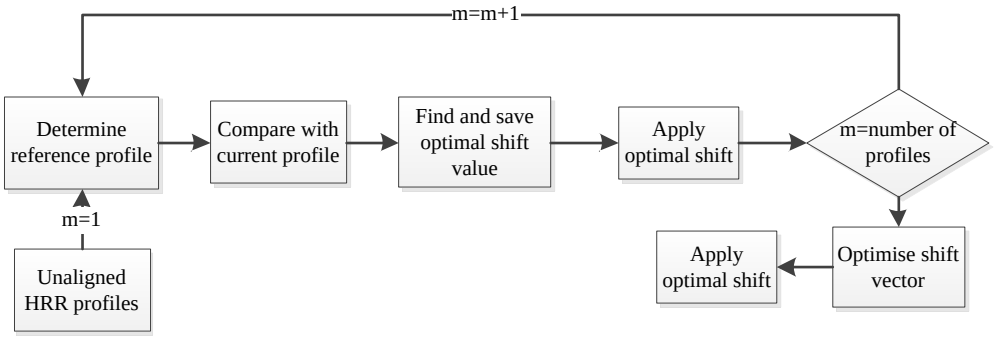

Figure 9.1: Flowchart depicting the various steps in a non-parametric range alignment algorithm.

Figure 9.1 shows the basic steps involved in a non-parametric range alignment algorithm. Various options exist for the different steps, which could influence the performance of the algorithm in terms of alignment quality and computational load.

Findings in this study provide various options to the parameters of each step shown in Figure 9.1. A summary of these considerations and parameters for the processing steps is provided below.

Determine reference profile

- Methods of combining the profiles to form the reference profile
  - Sum envelope
- Number of profiles to use in reference profile calculation
  - Large number of profiles - high robustness to noise and self-correcting of minor alignment errors. For highly fluctuating targets, the reference profile may lose significance as the peaks "cancel out" due to averaging.
  - Small number of profiles - able to accommodate returns from high speed targets, but error accumulation may occur.
- Weighting profiles used in reference profile calculation

  - Linear
  - Exponential

Compare with current profile

- Choice of cost function - consider data characteristics and quality measure sensitivities
  - Correlation
  - Entropy
  - Contrast

Find and save optimal shift value

- Choice of resolution where sub-bin accuracy is required (fine) or computational cost should be lowered (coarse)
- Estimation of the search space - linked to the scatterer displacement (target speed) allowed or assumed

Apply optimal shift

- Circular data shift for integer values
- Phase ramp for sub-integer resolution
- Phase considerations post shifting (topic for future work)

Optimise shift vector

- Filtering
- Interpolation
- Making use of tracking algorithms

9.2 Improved simulations for sensitivity analysis

The simulations used in Chapter 6 were intended to illustrate the possible trends in quality measure sensitivity. Simulations with improved accuracy, particularly for investigating the effect of micro-Doppler and clutter effects, may be useful. Added accuracy in these simulations will produce quantitative results that may be used in the development of *adaptive* alignment algorithms.

9.3 Complex analysis

In this study, only the envelopes of range profiles where considered. Addition of phase alignment in conjunction with envelope alignment may produce improved ISAR images. The use of the complex range profiles when estimating the alignment cost functions warrants further investigation.

Bibliography

[1] V. J van Rensburg, "HRR profile range alignment for ISAR imaging," tech. rep., CSIR, 2012.

[2] D. Barton and S. Leonov, *Radar technology encyclopaedia*. Artech house, 1997.

[3] C. Chen and H. Andrews, "Target-motion-induced radar imaging," *Aerospace and Electronic Systems, IEEE Transactions on*, no. 1, pp. 2–14, 1980.

[4] A. Zyweck, *Preprocessing Issues in High Resolution Radar Target Classification*. PhD thesis, The University of Adelaide, 1995.

[5] D. Ausherman, A. Kozma, J. Walker, H. Jones, and E. Poggio, "Developments in radar imaging," *Aerospace and Electronic Systems, IEEE Transactions on*, no. 4, pp. 363–400, 1984.

[6] J. Wang and D. Kasilingam, "Global range alignment for ISAR," *Aerospace and Electronic Systems, IEEE Transactions on*, vol. 39, no. 1, pp. 351–357, 2003.

[7] G. Stimson, *Introduction to airborne radar*. SciTech Pub., 1998.

[8] C. Ozdemir, *Inverse Synthetic Aperture Radar Imaging with MATLAB Algorithms*, vol. 210. Wiley-Interscience, 2012.

[9] F. Anderson, "Radar sensor technology developments as csir dpss in support of persistent, ubiquitous surveillance systems," 2008.

[10] L. Xi, L. Guosui, and J. Ni, "Autofocusing of ISAR images based on entropy minimization," *Aerospace and Electronic Systems, IEEE Transactions on*, vol. 35, no. 4, pp. 1240–1252, 1999.

[11] M. Martorella, F. Berizzi, and B. Haywood, "Contrast maximisation based technique for 2-D ISAR autofocusing," in *Radar, Sonar and Navigation, IEE Proceedings-*, vol. 152, pp. 253–262, IET, 2005.

[12] M. Martorella, "ISAR Signal Modeling." University Lecture, 2011.

[13] D. Wahl, P. Eichel, D. Ghiglia, and C. Jakowatz Jr, "Phase gradient autofocus-a robust tool for high resolution SAR phase correction," *Aerospace and Electronic Systems, IEEE Transactions on*, vol. 30, no. 3, pp. 827–835, 1994.

[14] B. Steinberg, "Microwave imaging of aircraft," *Proceedings of the IEEE*, vol. 76, no. 12, pp. 1578–1592, 1988.

[15] B. Haywood and R. Evans, "Motion compensation for ISAR imaging," *Proceedings of ASSPA*, vol. 89, pp. 113–117, 1989.

[16] J. Muñoz-Ferreras and F. Pérez-Martínez, "Subinteger range-bin alignment method for ISAR imaging of noncooperative targets," *EURASIP Journal on Advances in Signal Processing*, vol. 2010, p. 14, 2010.

[17] J. Muñoz-Ferreras and F. Pérez-Martínez, "Extended envelope correlation for range bin alignment in ISAR," in *Radar Systems, 2007 IET International Conference on*, pp. 1–5, IET, 2007.

[18] G. Delisle and H. Wu, "Moving target imaging and trajectory computation using ISAR," *Aerospace and Electronic Systems, IEEE Transactions on*, vol. 30, no. 3, pp. 887–899, 1994.

[19] J. Son, G. Thomas, and B. Flores, *Range-Doppler radar imaging and motion compensation*, vol. 1. Artech House Publishers, 2000.

[20] MATLAB®, *version 7.13.0.564 (R2011b)*. Natick, Massachusetts: The MathWorks Inc., 2011.

[21] T. Sauer and A. Schroth, "Robust range alignment algorithm via Hough transform in an ISAR imaging system," *Aerospace and Electronic Systems, IEEE Transactions on*, vol. 31, no. 3, pp. 1173–1177, 1995.

[22] J. Wang and X. Liu, "Improved global range alignment for ISAR," *Aerospace and Electronic Systems, IEEE Transactions on*, vol. 43, no. 3, pp. 1070–1075, 2007.

[23] D. Zhu, L. Wang, Y. Yu, Q. Tao, and Z. Zhu, "Robust ISAR range alignment via minimizing the entropy of the average range profile," *Geoscience and Remote Sensing Letters, IEEE*, vol. 6, no. 2, pp. 204–208, 2009.

[24] J. Muñoz-Ferreras, J. Calvo-Gallego, F. Pérez-Martínez, A. Blanco-del Campo, A. Asensio-López, and B. Dorta-Naranjo, "Motion compensation for ISAR based on the shift-and-convolution algorithm," in *Radar, 2006 IEEE Conference on*, pp. 5–pp, IEEE, 2006.

[25] C. Shannon, "A mathematical theory of communication," *ACM SIGMOBILE Mobile Computing and Communications Review*, vol. 5, no. 1, pp. 3–55, 2001.

[26] T. Pun, "A new method for grey-level picture thresholding using the entropy of the histogram," *Signal processing*, vol. 2, no. 3, pp. 223–237, 1980.

[27] N. Pal and S. Pal, "Entropy: a new definition and its applications," *Systems, Man and Cybernetics, IEEE Transactions on*, vol. 21, no. 5, pp. 1260–1270, 1991.

[28] B. Flores, A. Ugarte, and V. Kreinovich, "Choice of an entropy-like function for range-Doppler processing," in *Proceedings of SPIE*, vol. 47, p. 1993, 1960.

[29] R. Bocker and S. Jones, "ISAR motion compensation using the burst derivative measure as a focal quality indicator," *International Journal of Imaging Systems and Technology*, vol. 4, no. 4, pp. 285–297, 1992.

[30] R. Bocker and S. Jones, "Using the burst derivative measure to improve the computational efficiency of ISAR motion compensation algorithms," tech. rep., DTIC Document, 1992.

[31] R. Bassem and Z. Atef, "Matlab simulations for radar systems design," 2004.

[32] P. Lacomme, J. Hardange, J. Marchais, and E. Normant, "Air and Spaceborne Radar Systems: An Introduction (SPIE Press Book)," 2001.

[33] M. van Ginkel, C. Hendriks, and L. van Vliet, "A short introduction to the Radon and Hough transforms and how they relate to each other," *the Quantitative Image Group Technical Report Series, N. QI-2004-01*, pp. 1–9, 2004.

Appendix A

Entropy of a Gaussian random variable

Assume a normally distributed random variable, x. The probability density function of x, p(x), is given by Equation A.1.

$$p(x) = \frac{1}{\sqrt{2\pi\sigma^2}} e^{\frac{(x-\mu)^2}{2\sigma^2}} \tag{A.1}$$

where μ is the *mean* and σ is the *standard deviation* of x.

Properties of p(x) include:

(1) The area over the pdf for all values of x is unity.

$$\boxed{\int_{-\infty}^{\infty} p(x)dx = 1}$$

Proof:

$$\int_{-\infty}^{\infty} p(x)dx = \int_{-\infty}^{\infty} \frac{1}{\sqrt{2\pi\sigma^2}} e^{-\frac{(x-\mu)^2}{2\sigma^2}} dx \tag{A.2a}$$

Let $y = x - \mu$, $dx = dy$, then Eq. (A.2a) becomes

$$= \frac{1}{\sqrt{2\pi\sigma^2}} \int_{-\infty}^{\infty} e^{-\frac{y^2}{2\sigma^2}} dy \tag{A.2b}$$

Due to the symmetry of the function about y, (A.2b) can be written as

$$\begin{aligned} &= \frac{2}{\sqrt{2\pi\sigma^2}} \int_0^\infty e^{-\frac{y^2}{2\sigma^2}} dy \\ &= \frac{2}{\sqrt{2\pi\sigma^2}} \frac{\sqrt{2\pi\sigma^2}}{2} \\ &= 1 \end{aligned}$$

(2) The *expected value* of a Gaussian variable x is equal to the mean of x, μ.

$$\boxed{E[x] = \int_{-\infty}^{\infty} xp(x)dx = \mu}$$

Proof:

$$\int_{-\infty}^{\infty} xp(x)dx = \int_{-\infty}^{\infty} \frac{x}{\sqrt{2\pi\sigma^2}} e^{-\frac{(x-\mu)^2}{2\sigma^2}} dx \tag{A.3a}$$

Let $y = \frac{x-\mu}{\sqrt{2}\sigma}$, $dx = \sqrt{2}\sigma dy$, then (A.3a) becomes

$$\begin{aligned} &= \sqrt{2}\sigma \int_{-\infty}^{\infty} \frac{\sqrt{2}\sigma y + \mu}{\sqrt{2\pi\sigma^2}} e^{-y^2} dy \\ &= \frac{\sqrt{2}\sigma}{\sqrt{\pi}} \int_{-\infty}^{\infty} y e^{-y^2} dy + \frac{\mu}{\sqrt{\pi}} \int_{-\infty}^{\infty} e^{-y^2} dy \end{aligned}$$

Since $\int_{-\infty}^{\infty} ye^{-y^2}dy = 0$ and $\int_{-\infty}^{\infty} e^{-y^2}dy = \sqrt{\pi}$, the equation becomes:

$$\begin{aligned} &= 0 + \frac{\mu}{\sqrt{\pi}}\sqrt{\pi} \\ &= \mu \end{aligned}$$

(3) The expected value of $(x-\mu)^2$ is equal to the *variance*, σ^2.

$$\boxed{E[(x-\mu)^2] = \int_{-\infty}^{\infty} (x-\mu)^2 p(x) = \sigma^2}$$

Proof:

$$E[(x-\mu)^2] = \int_{-\infty}^{\infty} \frac{(x-\mu)^2}{\sqrt{2\pi\sigma^2}} e^{-\frac{(x-\mu)^2}{2\sigma^2}} \tag{A.4a}$$

Let $y = x - \mu$, $dx = dy$, then (A.4a) becomes

$$\frac{1}{\sqrt{2\pi\sigma^2}} \int_{-\infty}^{\infty} y^2 e^{-\frac{y^2}{2\sigma^2}} \tag{A.4b}$$

and using $\int_{-\infty}^{\infty} x^2 e^{-ax^2} = \frac{1}{2}\sqrt{\frac{\pi}{a^3}}$:

$$\begin{aligned} &= \frac{1}{\sqrt{2\pi\sigma^2}} \frac{1}{2} \sqrt{\pi (2\sigma^2)^3} \\ &= \frac{1}{\sqrt{2\pi\sigma^2}} \sqrt{2\pi}\sigma^3 \\ &= \sigma^2 \end{aligned}$$

(4) The *entropy*, H, of the Gaussian variable x is $\ln(\sigma\sqrt{2\pi e})$**.**

$$\boxed{H = -\int_{-\infty}^{\infty} p(x) \ln p(x) dx = \ln(\sigma\sqrt{2\pi e})}$$

Proof:

$$H = -\int_{-\infty}^{\infty} \frac{1}{\sqrt{2\pi\sigma^2}} e^{-\frac{(x-\mu)^2}{2\sigma^2}} \ln\left(\frac{1}{\sqrt{2\pi\sigma^2}} e^{-\frac{(x-\mu)^2}{2\sigma^2}}\right) dx \tag{A.5a}$$

Using the $\ln(ab) = \ln(a) + \ln(b)$ and $\ln(\frac{1}{c}) = -\ln(c)$ properties, (A.5a) becomes:

$$\begin{aligned} &= -\int_{-\infty}^{\infty} \frac{1}{\sqrt{2\pi\sigma^2}} e^{-\frac{(x-\mu)^2}{2\sigma^2}} \left[-\ln\left(\sqrt{2\pi\sigma^2}\right) - \frac{(x-\mu)^2}{2\sigma^2}\right] dx \\ &= \ln(\sqrt{2\pi\sigma^2}) \int_{-\infty}^{\infty} \frac{1}{\sqrt{2\pi\sigma^2}} e^{-\frac{(x-\mu)^2}{2\sigma^2}} + \frac{1}{2\sigma^2} \int_{-\infty}^{\infty} \frac{(x-\mu)^2}{\sqrt{2\pi\sigma^2}} e^{-\frac{(x-\mu)^2}{2\sigma^2}} \\ &= \ln(\sqrt{2\pi\sigma^2}) \int_{-\infty}^{\infty} p(x) dx + \frac{1}{2\sigma^2} E[(x-\mu)^2] \\ &= \frac{1}{2}\ln(2\pi\sigma^2) + \frac{1}{2\sigma^2}\sigma^2 \\ &= \frac{1}{2}\ln(2\pi\sigma^2) + \frac{1}{2}\ln e \\ &= \ln(\sigma\sqrt{2\pi e}) \end{aligned}$$

Appendix B

The Global Range Bin Alignment Algorithm Flow Diagram

The shift value applied to profile m, τ_m is calculated using Equation B.1.

$$\tau_m = \sum_{i=1}^{\infty} \beta(i) \left(\frac{2m}{M} - 1 \right)^i \tag{B.1}$$

As mentioned before, the value of $\beta(i)$ is calculated using an iterative algorithm. The algorithm is explained in the flowchart of Figure B.1, which also appears in Wang [6].

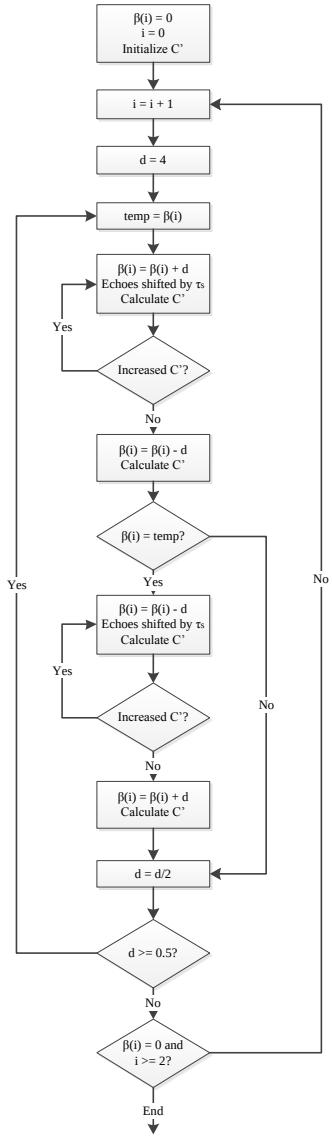

Figure B.1: The flow diagram shows the iterative process for in calculating the value of $\beta(i)$ that results in optimal contrast of the range envelope.

Appendix C

The Hough Transform

The Hough transform is an image processing technique which is used for detecting straight lines in images. Equation C.1 provides the traditional straight line expression in Cartesian coordinates.

$$y = mx + c \tag{C.1}$$

With the Hough transform method, the Hessian normal parameterization is preferred over the Cartesian system because of the unbounded nature of Equation C.1 for vertical lines. An expression for the parameterization is given in Equation C.2.

$$\rho = x \cos \phi + y \sin \phi \tag{C.2}$$

The relationship between EquationC.1 and the parameterization given in C.2 is presented graphically by Figure C.1.

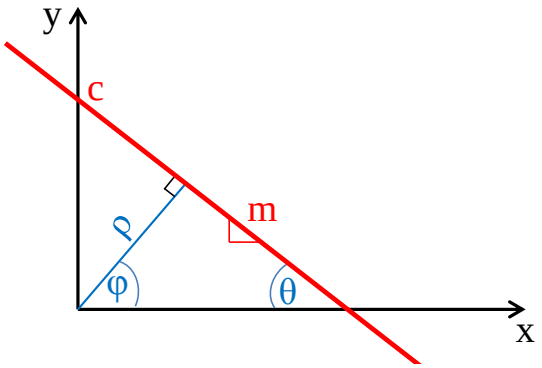

Figure C.1: The Hessian parameterization can be indicated on the Cartesian plane as shown above. The Hessian parameters, (ρ, ϕ), are indicated in blue and the straight line parameters, (m, c), in red.

It can easily be verified from Figure C.1 that the values of m and c can be found using Equation C.3 and Equation C.4, respectively.

$$\begin{aligned} m &= tan(\theta) \\ \text{where } \theta &= 90^\circ - \phi \end{aligned} \tag{C.3}$$

$$c = \frac{\rho}{\cos(90^\circ - \phi)} = \frac{\rho}{\sin(\phi)} \tag{C.4}$$

The Hough transform can be considered as a *discretisation* of the (continuous) Radon transform (van Ginkel [33]). If the input data is sparse, the Hough transform offers a reduction in computation time [33].

The Hough transform of the image is formed from a pre-processed version of the image and is mapped to a parameter space. The parameter space is created by determining realistic bounds on the value of m, which presents the velocity of the tracked scatterer with respect to the radar. The maxima of the Hough transform provides an indication of the parameters of the straight line. An example of an image containing a straight line with $m = 1$ and $c = 128$ is given in Figure C.2.

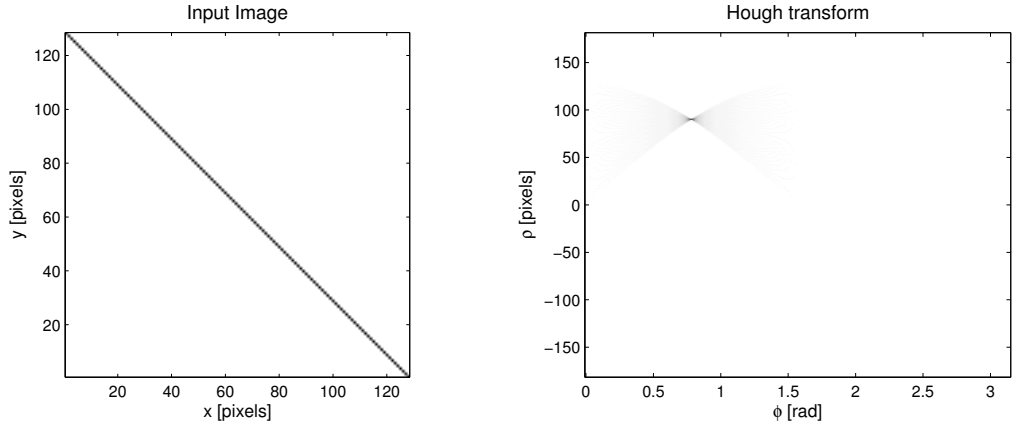

Figure C.2: The input image (left) and its corresponding Hough transform (right) are indicated in the figure above. The Hough transform was calculated with an angular resolution of $\pi/180$.

As seen in Figure C.2, the peak in the Hough transform is located at (0.7854,89.9807), which corresponds to estimates of (m,c) of (1,127.2519) when using Equations C.3 and C.4.

Appendix D

Mathematical derivations of Quality Measures

D.1 Sum Envelope Contrast

The derivation below appears in Wang [6] and is used for quantifying range alignment quality of an aligned high resolution range profile data set.

The sum envelope as defined in D.1:

$$a(n) = \sum_{m=0}^{M-1} |x(m,n)| \tag{D.1}$$

$x(m,n)$ is the range resolved signal, m refers to the range profile number, n to the range bin number and M is the total number of range profiles in the dataset. The contrast of $a(n)$ is defined in Equation D.2.

$$C = \frac{\sigma[a(n)]}{E[a(n)]} \tag{D.2}$$

where $E[a(n)]$ is the mean of $a(n)$ with respect to n, as shown in Equation D.3.

$$E[a(n)] = \frac{1}{N}\sum_{n=0}^{N-1} a(n) \tag{D.3}$$

where N is the total number of range bins per profile. $\sigma[a(n)]$ refers to the standard deviation of $a(n)$ with respect to n, as in Equation D.4.

$$\sigma[a(n)] = \sqrt{\frac{1}{N}\sum_{n=0}^{N-1}\left[a(n) - \frac{1}{N}\sum_{n'=0}^{N-1} a(n')\right]^2} \tag{D.4}$$

which can also be written as Equation D.5.

$$\sigma[a(n)] = \sqrt{\frac{1}{N}\sum_{n=0}^{N-1} a(n)^2 - \left[\frac{1}{N}\sum_{n=0}^{N-1} a(n)\right]^2} \tag{D.5}$$

The envelopes of the profiles are assumed to have similar shapes but varying time delays, so when all the profiles are properly aligned, $a(n)$ would be sharp and C is a maximum. Substituting Equation D.3 and Equation D.5 into Equation D.2 results in Equation D.6.

$$C = \sqrt{\frac{N}{A^2}\sum_{n=0}^{N-1} a(n)^2 - 1} \tag{D.6}$$

where

$$A = \sum_{n=0}^{N-1} a(n) \tag{D.7}$$

Now, since A is a constant value in range aligned data, contrast can be defined in the more efficient form of Equation D.8, shown below.

$$C' = \sum_{n=0}^{N-1} a(n)^2 \tag{D.8}$$

The next steps validate this expression for image contrast.

If the sum envelope definition, Equation D.1 is substituted in D.8, one obtains

$$C' = e + 2\sum_{m=0}^{M-2}\sum_{l=m+1}^{M-1} c(m,l) \tag{D.9}$$

where e is the total energy of $x(m,n)$, as given below.

$$e = \sum_{m=0}^{M-1}\sum_{n=0}^{N-1} |x(m,n)|^2 \tag{D.10}$$

and $c(m,l)$ is the envelope *correlation* of profile m and l, defined below.

$$c(m,l) = \sum_{n=0}^{N-1} |x(m,n)|\,|x(l,n)| \tag{D.11}$$

The value of e is a constant in range alignment. The profile envelopes have similar shapes but varying time delays, so when all the profiles are aligned, every $c(m,l)$ is a maximum and therefore C' is also a maximum.

D.2 Sum Envelope Entropy

The sum envelope entropy as defined in Wang [6] uses the same definition for the sum envelope, given in Equation D.1.

The sum envelope entropy, H, is defined is Equation D.12.

$$H = -\sum_{n=0}^{N-1} \frac{a(n)}{A} \ln \frac{a(n)}{A} \tag{D.12}$$

where the definitions of n, N and A remains as given previously. Again, the envelopes of different profiles within a data set has similar shapes but varying time delays, therefore, when all the profiles are aligned, $a(n)$ is sharpest and

therefore H would be a minimum. Equation D.12 can be rewritten as

$$H = \ln A - \frac{1}{A}\sum_{n=0}^{N-1} a(n)\ln a(n) \tag{D.13}$$

A remains constant in range alignment, so H can be redefined as

$$H' = -\sum_{n=0}^{N-1} a(n)\ln a(n) \tag{D.14}$$

which can be calculated more efficiently than Equation D.12.

D.3 Global Envelope Correlation

The definition of the global envelope correlation, as given in Wang [6] is reproduced here.

The global envelope correlation, G, is defined as

$$G = \sum_{m=0}^{M-2}\sum_{l=m+1}^{M-1} \phi(m,l)c(m,l) \tag{D.15}$$

where $\phi(m,l)$ is a weighting function. The similar shape, but varying time delays of the profiles in the data set implies that when the profiles are properly aligned, every $c(m,l)$ is a maximum and hence, G is a maximum as well. A typical choice for $\phi(m,l)$ is

$$\phi(m,l) = \exp\left[-\left(\frac{l-m}{\delta}\right)^2\right] \tag{D.16}$$

where δ is chosen according to the particular application.

D.4 Variance of the peak location

The definition for the variance in the peak location, used in Wang [6] for quantifying the quality of range alignment, is presented in this section.

The variance of the peak location, V, is defined below.

$$V = \nu[n_p(m)] \tag{D.17}$$

where $n_p(m)$ is the location index of the range bin that contains the maximum amplitude value for a certain range profile m. The variance of $n_p(m)$ with respect to m, denoted as $\nu[n_p(m)]$ is defined as

$$\nu\left[n_p(m)\right] = \frac{1}{M}\sum_{m=0}^{M-1}\left[n_p(m) - \frac{1}{M}\sum_{m'=0}^{M-1} n_p(m')\right]^2 \tag{D.18}$$

or equivalently

$$\nu[n_p(m)] = \frac{1}{M}\sum_{m=0}^{M-1} n_p(m)^2 - \left[\frac{1}{M}\sum_{m=0}^{M-1} n_p(m)\right]^2 \tag{D.19}$$

A smaller value for V indicates improved alignment.

D.5 Burst Derivative

The burst derivative, B, for a partially compensated[1] signature of a point target as defined in Son [19], appears in Equation D.20.

$$B = \sum_{m=0}^{M-2}\sum_{n=0}^{N-1} 4\sin^2\left[4\pi\frac{f_n}{c}(r_{m,n} - \tilde{r}_{m,n} + r_{m+1,n} - \tilde{r}_{m+1,n})\right] \tag{D.20}$$

[1]Each iteration would be a partial compensation of the input.

where f_n is the frequency of the n$^{\text{th}}$ pulse in a burst and $r_{m,n} - \tilde{r}_{m,n}$ is defined in Equation D.21.

$$r_{m,n} - \tilde{r}_{m,n} = r_0 + \Delta v t_{m,n} + \frac{1}{2}\Delta a t_{m,n}^2 \tag{D.21}$$

where $t_{m,n}$ is the sampling time, given by Equation D.22.

$$t_{m,n} = (n + mN)\Delta t \tag{D.22}$$

and Δt is the pulse repetition interval (PRI) of the waveform.

In Equation D.21, Δv is the velocity estimation error and Δa is the acceleration estimation error, which when minimised should provide the desirable motion estimation[2] for proper motion compensation.

The phase term in Equation 4.9 represents the range bin shift between adjacent profiles resulting from the target motion. Clearly, the burst derivative has a minimum value of 0 when no range bin shifts (from target motion) exist between profiles and is positive for any nonzero bin shifts.

[2]Assuming the approximation to the target motion in Equation D.21 holds. In cases where higher order motion, such as *jerk*, occurs, more variables are included in the motion estimate.

Appendix E

Aligned Aircraft Data

An example of unaligned HRR data for a King Air 200 propeller aircraft appears in Figure E.1.

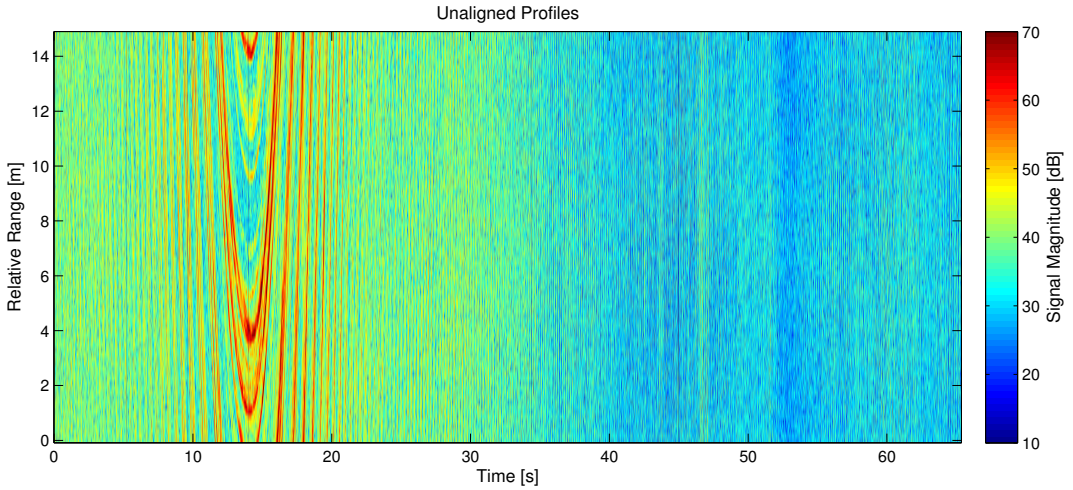

Figure E.1: Unaligned HRR data of a King Air 200 propeller aircraft. From [1].

The data shown in Figure E.1 provides an example of the variability of HRR data in terms of target aspect angle, speed and range changes. The flight path of the target corresponding to the measurement shown in Figure E.1 is provided in Figure E.2.

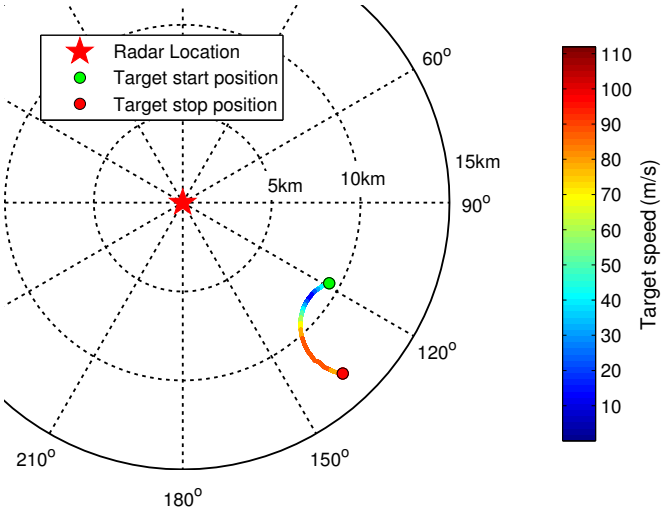

Figure E.2: Flight path of the King Air 200 aircraft for the measurements shown in Figure E.1. From [1].

The speed of the target is indicated by the colour used in the flight path representation in Figure E.2. The azimuth aspect angle of the target can be approximated from Figure E.2. The effect of the variations in the data as a result of the target position and motion on the quality measures is briefly discussed.

The data shown in Figure E.1 was divided into sets with lengths 0.5, 1 and 2 seconds. Each set was aligned using the methods presented in Chapter 3 and the quality measures, presented in Chapter 4, for each set were calculated.

E.1 Sum Envelope Contrast

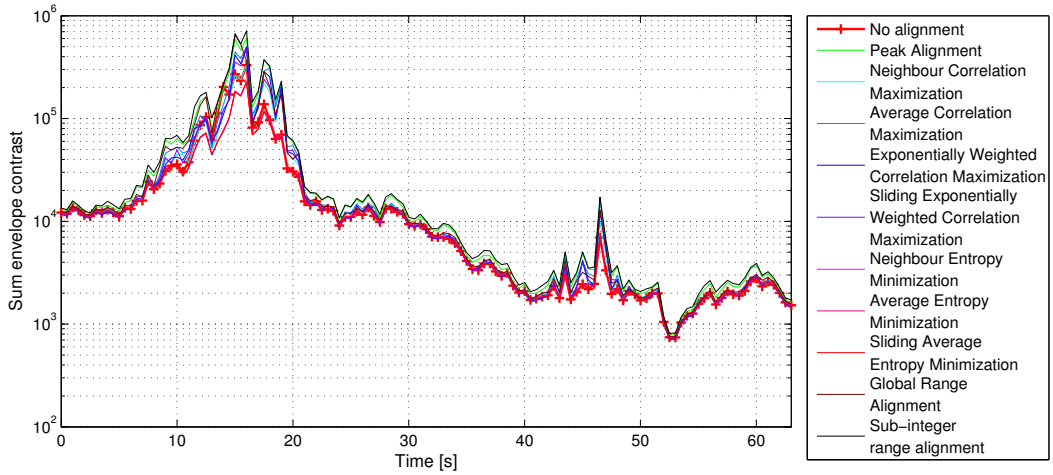

Figure E.3: Sum envelope contrast of King Air 200 of aligned and unaligned data. All methods presented in Chapter 3 were applied to data sets of 0.5 seconds each.

E.2 Sum Envelope Entropy

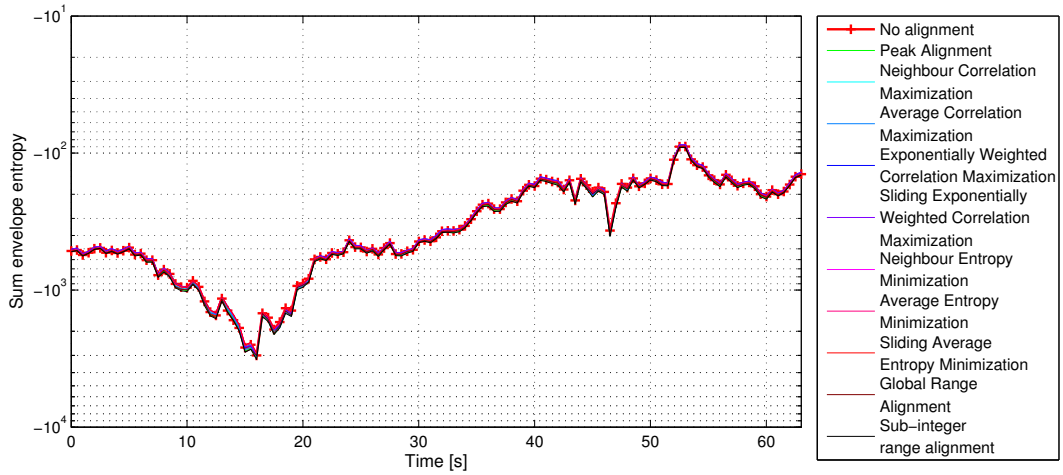

Figure E.4: Sum envelope entropy of King Air 200 of aligned and unaligned data. All methods presented in Chapter 3 were applied to data sets of 0.5 seconds each.

E.3 Global Envelope Correlation

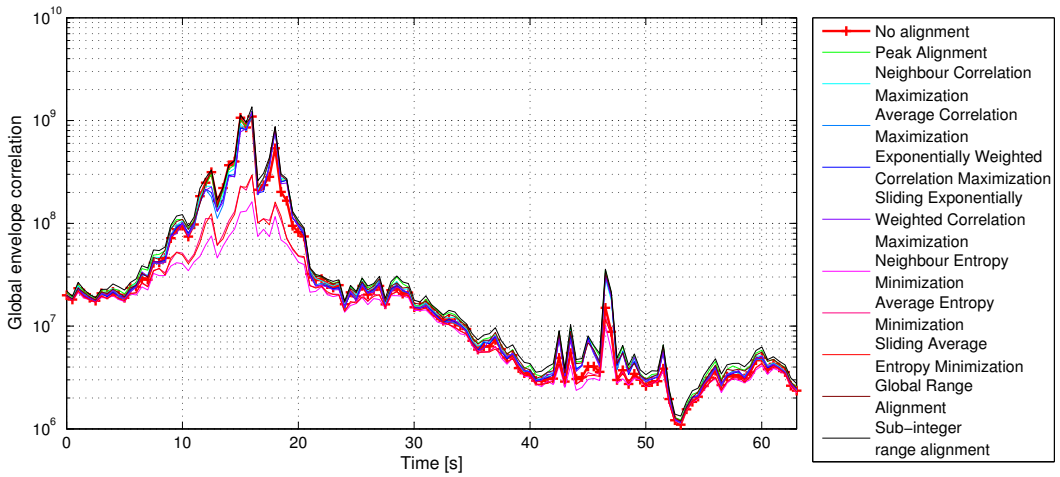

Figure E.5: Global envelope correlation of King Air 200 of aligned and unaligned data. All methods presented in Chapter 3 were applied to data sets of 0.5 seconds each.

E.4 Peak Location Variance

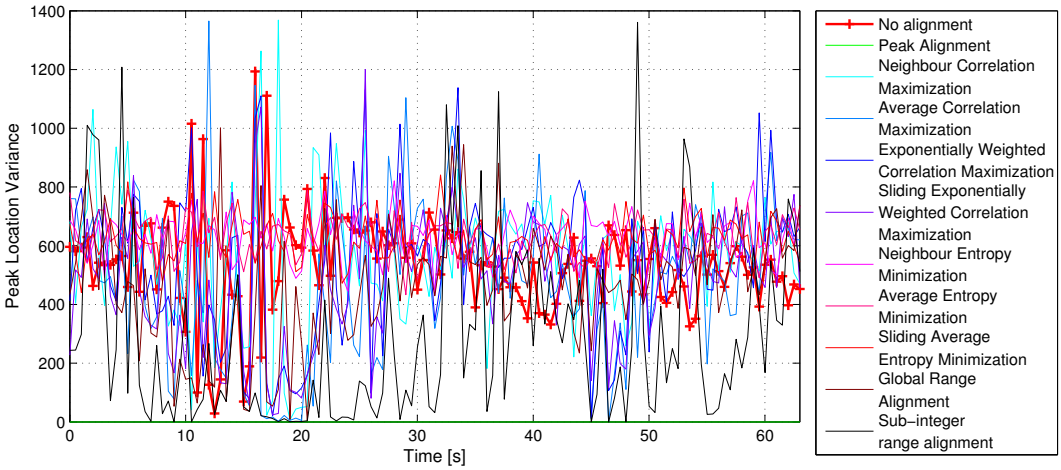

Figure E.6: Peak location variance of King Air 200 of aligned and unaligned data. All methods presented in Chapter 3 were applied to data sets of 0.5 seconds each.

E.5 Mean Squared Difference

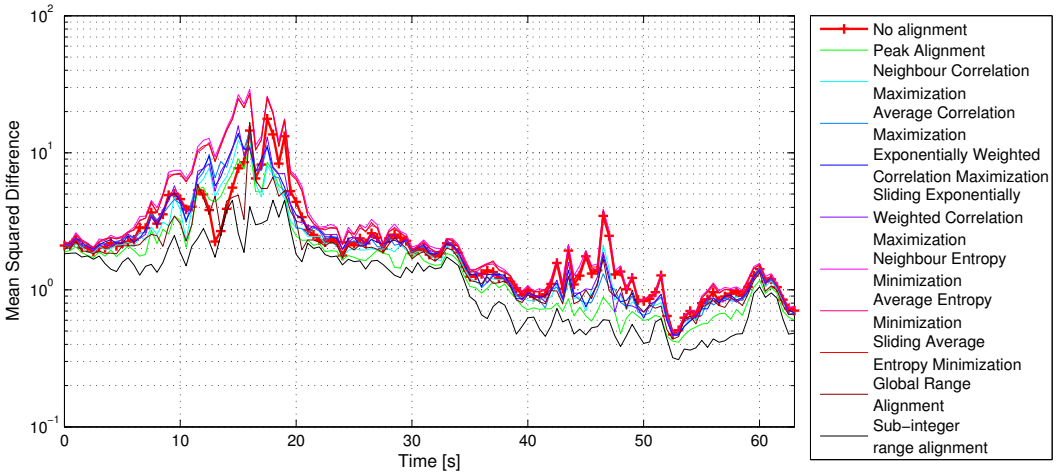

Figure E.7: Mean squared difference of King Air 200 of aligned and unaligned data. All methods presented in Chapter 3 were applied to data sets of 0.5 seconds each.

E.6 Burst Derivative

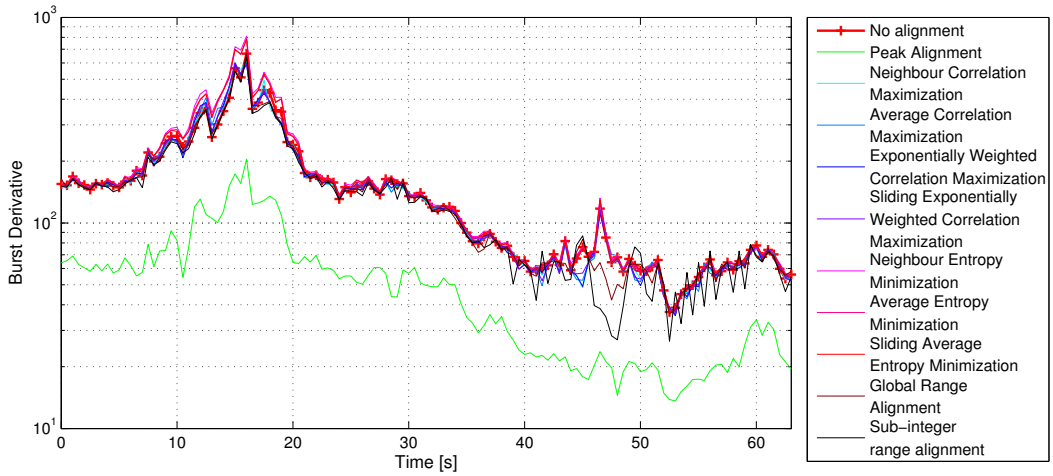

Figure E.8: Burst derivative of King Air 200 of aligned and unaligned data. All methods presented in Chapter 3 were applied to data sets of 0.5 seconds each.

Appendix F

Range alignment algorithm performance analysis

F.1 Aircraft data

	% of instances in nth position									
Method	**1st**	**2nd**	**3rd**	**4th**	**5th**	**6th**	**7th**	**8th**	**9th**	**10th**
Peak Alignment	0	96	3	0	0	0	0	0	0	0
Neighbour Correlation Maximization	0	0	2	16	35	18	25	0	0	0
Average Correlation Maximization	0	0	41	38	15	3	1	0	0	0
Exponentially Weighted Correlation Maximization	0	0	3	15	17	13	8	0	19	20
Sliding Exponentially Weighted Correlation Maximization	0	0	3	8	15	18	10	0	17	25
Neighbour Entropy Minimization	0	0	0	0	1	9	14	39	19	15
Average Entropy Minimization	0	0	0	0	3	12	14	32	20	15
Sliding Average Entropy Minimization	0	0	0	0	1	11	16	25	21	23
Global Range Alignment	0	3	45	21	9	11	8	0	0	0
Sub-integer range alignment	99	0	0	0	0	0	0	0	0	0

Table F.1: Performance based on sum envelope contrast

	% of instances in nth position									
Method	**1st**	**2nd**	**3rd**	**4th**	**5th**	**6th**	**7th**	**8th**	**9th**	**10th**
Peak Alignment	0	90	9	0	0	0	0	0	0	0
Neighbour Correlation Maximization	0	0	3	21	60	8	5	0	0	0
Average Correlation Maximization	0	0	36	48	14	0	0	0	0	0
Exponentially Weighted Correlation Maximization	0	0	0	1	5	12	4	0	40	34
Sliding Exponentially Weighted Correlation Maximization	0	0	0	0	3	8	8	0	31	47
Neighbour Entropy Minimization	0	0	0	0	1	21	24	41	7	3
Average Entropy Minimization	0	0	0	0	3	24	28	26	10	4
Sliding Average Entropy Minimization	0	0	0	0	1	22	26	31	9	9
Global Range Alignment	0	9	51	28	8	1	0	0	0	0
Sub-integer range alignment	100	0	0	0	0	0	0	0	0	0

Table F.2: Performance based on sum envelope entropy

	% of instances in nth position									
Method	**1st**	**2nd**	**3rd**	**4th**	**5th**	**6th**	**7th**	**8th**	**9th**	**10th**
Peak Alignment	0	72	21	3	1	0	0	0	0	0
Neighbour Correlation Maximization	0	3	18	49	12	8	7	0	0	0
Average Correlation Maximization	0	0	6	12	24	25	29	0	0	0
Exponentially Weighted Correlation Maximization	0	0	5	13	29	30	20	0	0	0
Sliding Exponentially Weighted Correlation Maximization	0	0	2	7	25	30	33	1	0	0
Neighbour Entropy Minimization	0	0	0	0	0	0	0	2	6	90
Average Entropy Minimization	0	0	0	0	0	0	1	57	37	3
Sliding Average Entropy Minimization	0	0	0	0	0	0	0	37	55	6
Global Range Alignment	0	21	45	13	6	4	8	0	0	0
Sub-integer range alignment	99	0	0	0	0	0	0	0	0	0

Table F.3: Performance based on global envelope correlation

Method	% of instances in nth position									
	1st	**2nd**	**3rd**	**4th**	**5th**	**6th**	**7th**	**8th**	**9th**	**10th**
Peak Alignment	100	0	0	0	0	0	1	2	8	22
Neighbour Correlation Maximization	0	3	8	13	9	14	14	8	10	10
Average Correlation Maximization	0	4	30	13	12	5	5	6	7	9
Exponentially Weighted Correlation Maximization	0	2	13	16	15	12	7	5	11	8
Sliding Exponentially Weighted Correlation Maximization	0	3	14	20	20	14	7	5	4	2
Neighbour Entropy Minimization	0	0	2	7	9	10	17	24	16	10
Average Entropy Minimization	0	0	3	5	10	14	19	17	13	13
Sliding Average Entropy Minimization	0	1	3	6	7	12	15	22	20	8
Global Range Alignment	0	6	17	13	11	12	10	6	5	10
Sub-integer range alignment	0	75	6	2	1	0	0	1	1	4

Table F.4: Performance based on the variance in peak locations

Method	% of instances in nth position									
	1st	2nd	3rd	4th	5th	6th	7th	8th	9th	10th
Peak Alignment	0	73	20	3	0	0	0	1	2	2
Neighbour Correlation Maximization	0	3	20	50	14	5	4	0	0	0
Average Correlation Maximization	0	0	8	13	28	22	25	1	0	0
Exponentially Weighted Correlation Maximization	0	0	2	9	27	35	22	1	0	0
Sliding Exponentially Weighted Correlation Maximization	0	0	1	5	23	29	37	1	0	0
Neighbour Entropy Minimization	0	0	0	0	0	0	0	2	6	88
Average Entropy Minimization	0	0	0	0	0	1	2	51	38	3
Sliding Average Entropy Minimization	0	0	0	0	0	0	2	40	50	4
Global Range Alignment	0	20	46	17	4	4	5	0	0	0
Sub-integer range alignment	99	0	0	0	0	0	0	0	0	0

Table F.5: Performance based on the mean squared envelope difference

Method	% of instances in nth position									
	1st	2nd	3rd	4th	5th	6th	7th	8th	9th	10th
Peak Alignment	100	1	1	2	2	2	2	4	4	5
Neighbour Correlation Maximization	0	9	13	24	20	14	10	1	2	0
Average Correlation Maximization	0	4	9	15	14	18	17	5	6	4
Exponentially Weighted Correlation Maximization	0	9	15	19	17	17	11	3	3	0
Sliding Exponentially Weighted Correlation Maximization	0	8	10	17	24	16	13	3	2	0
Neighbour Entropy Minimization	0	0	0	0	0	1	3	12	17	58
Average Entropy Minimization	0	0	0	2	3	8	16	35	22	5
Sliding Average Entropy Minimization	0	0	0	2	5	7	12	26	32	7
Global Range Alignment	0	10	36	11	7	9	8	2	6	4
Sub-integer range alignment	0	54	11	4	3	3	3	3	3	11

Table F.6: Performance based on the burst derivative

F.2 Maritime data

Method	% of instances in nth position									
	1st	2nd	3rd	4th	5th	6th	7th	8th	9th	10th
Peak Alignment	0	72	26	0	0	0	0	0	0	0
Neighbour Correlation Maximization	0	0	1	7	12	19	58	0	0	0
Average Correlation Maximization	0	1	22	41	16	11	6	0	0	0
Exponentially Weighted Correlation Maximization	0	0	5	19	34	22	17	0	0	0
Sliding Exponentially Weighted Correlation Maximization	0	0	2	18	27	37	14	0	0	0
Neighbour Entropy Minimization	0	0	0	0	0	0	0	67	22	9
Average Entropy Minimization	0	0	0	0	0	0	0	23	47	28
Sliding Average Entropy Minimization	0	0	0	0	0	0	0	8	29	61
Global Range Alignment	0	24	40	12	9	8	3	0	0	0
Sub-integer range alignment	98	1	0	0	0	0	0	0	0	0

Table F.7: Performance based on sum envelope contrast

Method	% of instances in nth position									
	1st	2nd	3rd	4th	5th	6th	7th	8th	9th	10th
Peak Alignment	0	57	41	0	0	0	0	0	0	0
Neighbour Correlation Maximization	0	0	3	13	33	21	27	0	0	0
Average Correlation Maximization	0	1	25	57	8	5	2	0	0	0
Exponentially Weighted Correlation Maximization	0	0	0	6	27	29	24	0	3	7
Sliding Exponentially Weighted Correlation Maximization	0	0	0	3	22	32	29	0	4	6
Neighbour Entropy Minimization	0	0	0	0	0	3	4	68	18	5
Average Entropy Minimization	0	0	0	0	0	3	6	20	44	25
Sliding Average Entropy Minimization	0	0	0	0	0	1	4	9	29	54
Global Range Alignment	4	36	28	18	6	3	1	0	0	0
Sub-integer range alignment	95	4	0	0	0	0	0	0	0	0

Table F.8: Performance based on sum envelope entropy

Method	% of instances in nth position									
	1st	2nd	3rd	4th	5th	6th	7th	8th	9th	10th
Peak Alignment	0	21	51	22	3	0	0	0	0	0
Neighbour Correlation Maximization	0	18	26	44	5	1	2	0	0	0
Average Correlation Maximization	0	0	3	10	29	26	30	0	0	0
Exponentially Weighted Correlation Maximization	0	0	2	7	37	31	21	0	0	0
Sliding Exponentially Weighted Correlation Maximization	0	0	0	3	20	35	39	0	0	0
Neighbour Entropy Minimization	0	0	0	0	0	0	0	0	0	100
Average Entropy Minimization	0	0	0	0	0	0	0	70	29	0
Sliding Average Entropy Minimization	0	0	0	0	0	0	0	29	70	0
Global Range Alignment	6	52	14	11	4	4	5	0	0	0
Sub-integer range alignment	93	6	0	0	0	0	0	0	0	0

Table F.9: Performance based on global envelope correlation

Method	% of instances in nth position								
	1st	2nd	3rd	4th	5th	6th	7th	8th	9th
Peak Alignment	100	0	0	0	0	0	0	0	5
Neighbour Correlation Maximization	0	0	11	16	15	14	17	3	6
Average Correlation Maximization	0	7	32	25	10	8	5	1	3
Exponentially Weighted Correlation Maximization	0	3	6	15	25	24	11	1	1
Sliding Exponentially Weighted Correlation Maximization	0	2	6	17	27	25	11	1	2
Neighbour Entropy Minimization	0	0	0	0	2	5	14	31	25
Average Entropy Minimization	0	0	0	1	2	6	15	26	22
Sliding Average Entropy Minimization	0	0	0	1	3	5	12	29	28
Global Range Alignment	0	12	28	17	9	7	9	2	2
Sub-integer range alignment	0	73	13	3	1	1	1	0	1

Table F.10: Performance based on the variance in peak locations

Method	% of instances in nth position									
	1st	2nd	3rd	4th	5th	6th	7th	8th	9th	10th
Peak Alignment	0	23	51	21	1	0	0	3	3	3
Neighbour Correlation Maximization	0	18	25	45	6	1	1	0	0	0
Average Correlation Maximization	0	0	3	11	33	25	26	0	0	0
Exponentially Weighted Correlation Maximization	0	0	1	5	35	33	23	0	0	0
Sliding Exponentially Weighted Correlation Maximization	0	0	0	2	17	35	44	0	0	0
Neighbour Entropy Minimization	0	0	0	0	0	0	0	0	0	96
Average Entropy Minimization	0	0	0	0	0	0	0	73	23	0
Sliding Average Entropy Minimization	0	0	0	0	0	0	0	23	73	0
Global Range Alignment	5	49	17	13	5	3	3	0	0	0
Sub-integer range alignment	93	6	0	0	0	0	0	0	0	0

Table F.11: Performance based on the mean squared envelope difference

Method	% of instances in nth position									
	1st	2nd	3rd	4th	5th	6th	7th	8th	9th	10th
Peak Alignment	100	2	2	2	2	2	2	4	5	5
Neighbour Correlation Maximization	0	4	13	49	14	7	3	2	1	0
Average Correlation Maximization	0	5	5	11	23	22	28	0	0	0
Exponentially Weighted Correlation Maximization	0	9	8	13	26	22	16	0	0	0
Sliding Exponentially Weighted Correlation Maximization	0	8	8	7	20	25	26	0	0	0
Neighbour Entropy Minimization	0	0	0	0	0	0	2	3	2	85
Average Entropy Minimization	0	1	0	1	1	1	3	52	32	0
Sliding Average Entropy Minimization	0	0	0	0	1	3	2	33	51	0
Global Range Alignment	0	11	45	7	7	8	8	1	4	1
Sub-integer range alignment	0	55	14	4	2	5	4	1	2	5

Table F.12: Performance based on the burst derivative

Appendix G

Aligned Maritime Data

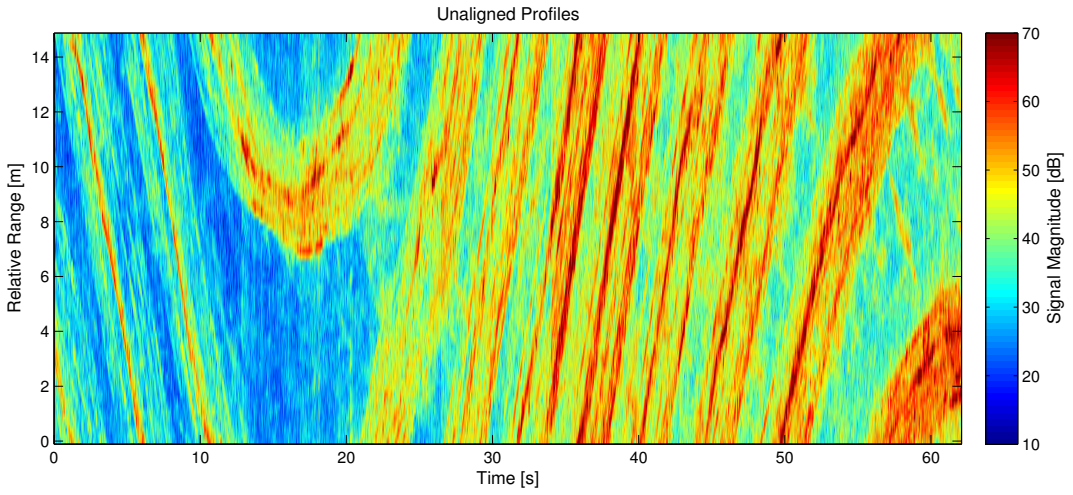

Figure G.1: Unaligned HRR data of Umoyo Omusha sailing yacht. From [1].

Figure G.2

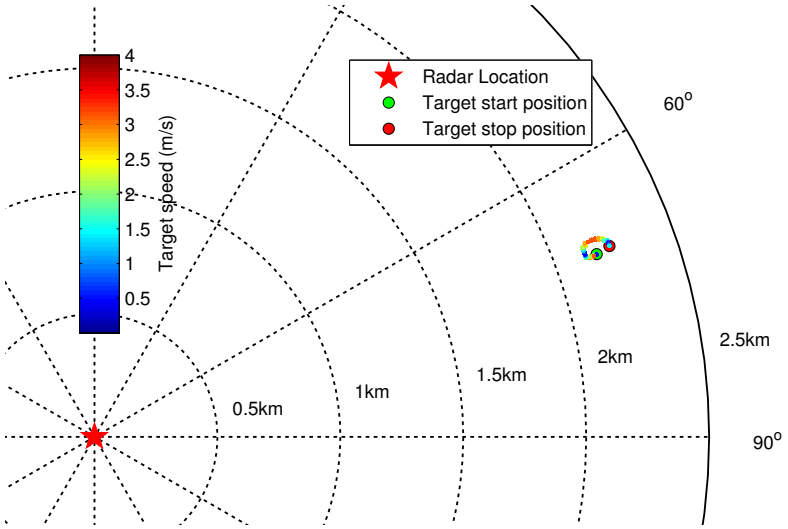

Figure G.2: Sailing path of the Umoya Omusha sailing yacht for the measurements shown in Figure G.1. From [1].

G.1 Sum Envelope Contrast

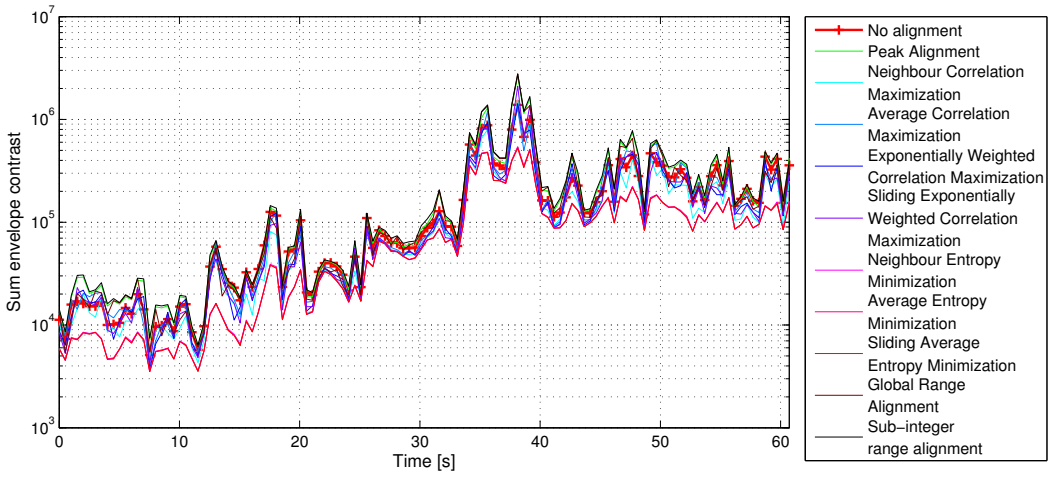

Figure G.3: Sum envelope contrast of Umoyo Omusha of aligned and unaligned data. All methods presented in Chapter 3 were applied to data sets of 0.5 seconds each.

G.2 Sum Envelope Entropy

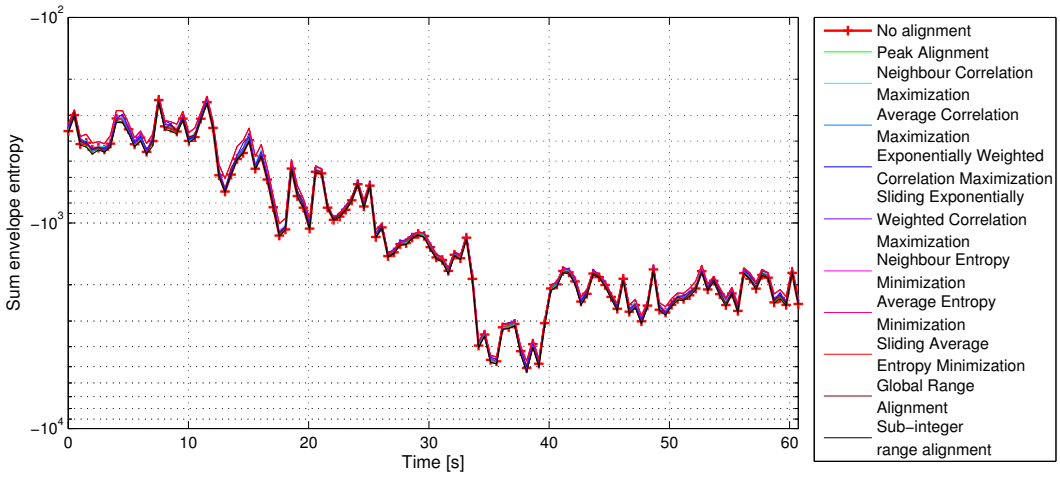

Figure G.4: Sum envelope entropy of Umoyo Omusha of aligned and unaligned data. All methods presented in Chapter 3 were applied to data sets of 0.5 seconds each.

G.3 Global Envelope Correlation

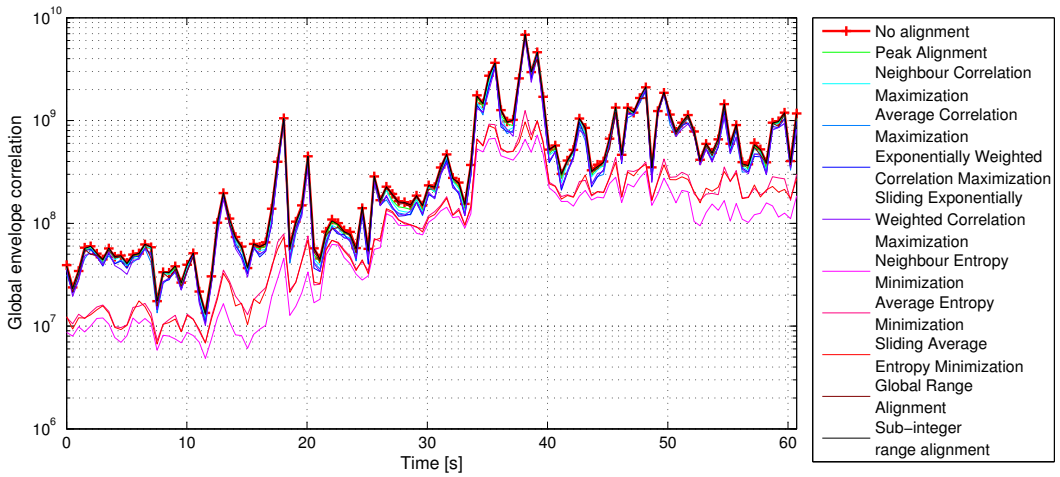

Figure G.5: Global envelope correlation of Umoyo Omusha of aligned and unaligned data. All methods presented in Chapter 3 were applied to data sets of 0.5 seconds each.

G.4 Peak Location Variance

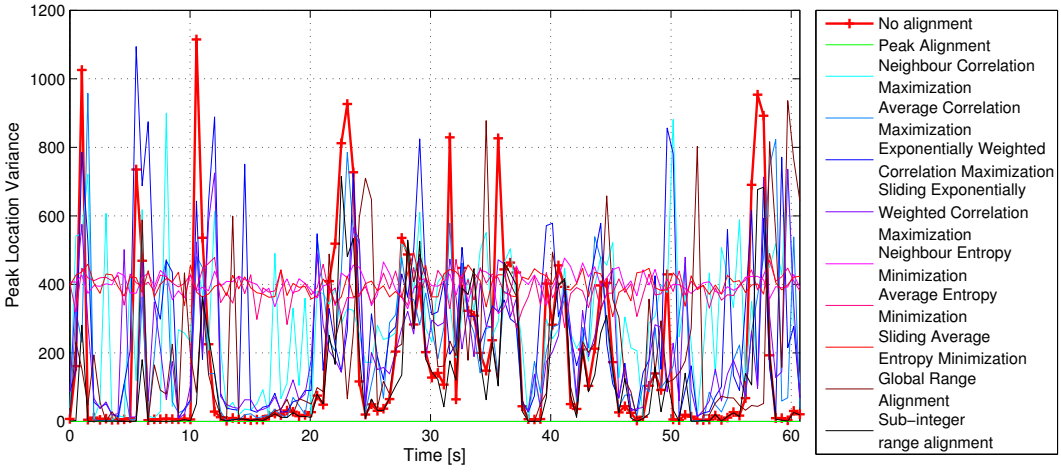

Figure G.6: Peak location variance of Umoyo Omusha of aligned and unaligned data. All methods presented in Chapter 3 were applied to data sets of 0.5 seconds each.

G.5 Mean Squared Difference

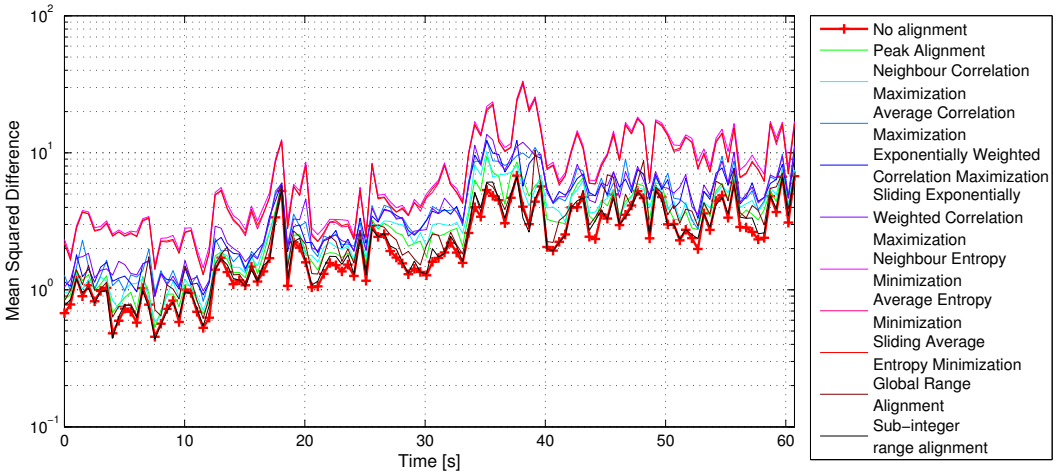

Figure G.7: Mean squared difference of Umoyo Omusha of aligned and unaligned data. All methods presented in Chapter 3 were applied to data sets of 0.5 seconds each.

G.6 Burst Derivative

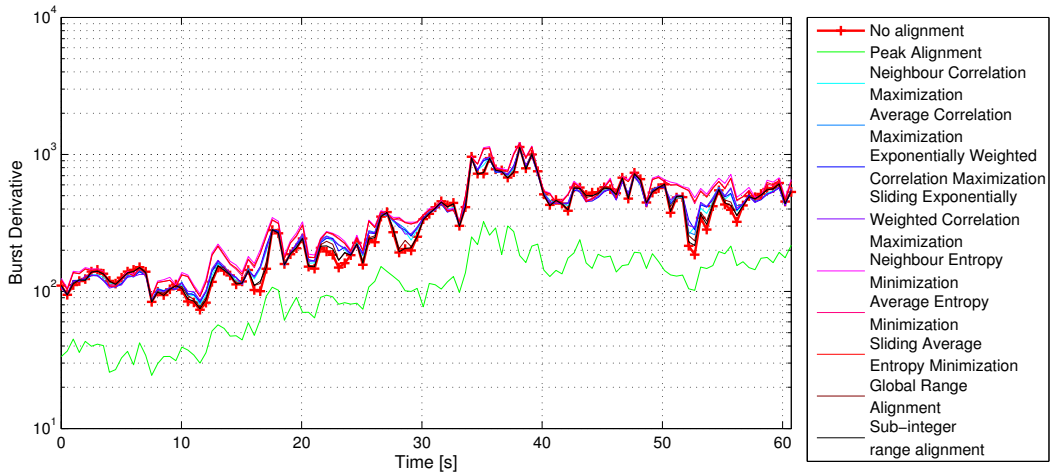

Figure G.8: Burst derivative of Umoyo Omusha of aligned and unaligned data. All methods presented in Chapter 3 were applied to data sets of 0.5 seconds each.

Appendix H

Gaussian Noise

The probability density function of the Gaussian distribution is defined in Equation H.1 and appears in Figure H.1.

$$P(x) = \frac{1}{\sqrt{2\pi}\sigma_x} exp\left(-\frac{(x-\bar{x})^2}{2\sigma_x^2}\right) \quad -\infty < x < \infty \tag{H.1}$$

where $\bar{x}$ is the *mean* of x and σ_x^2 is the *variance* of x.

As mentioned previously, the noise modelled here has *zero* mean. Figure H.1 shows the pdf for different noise variance values.

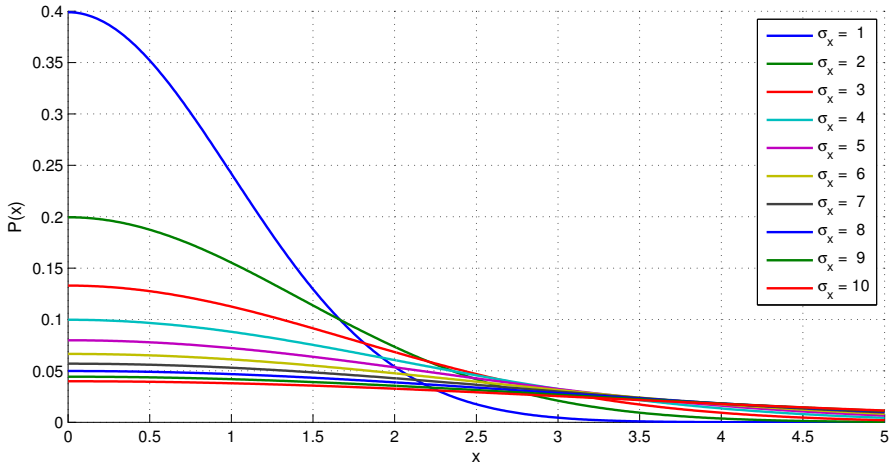

Figure H.1: The probability density function of white Gaussian noise for varying values of the standard deviation σ_x.

The probability density function shown in Figure H.1 and defined in Equation H.1 was used to generate the amplitude of noise samples to be applied to the hypothetical target return.

Appendix I

Effects of Error Accumulation

The effect of error accumulation on various quality measures is investigated in this chapter.

Sum Envelope Contrast

The effect of error accumulation on the sum envelope contrast is shown in Figure I.1. The analysis is performed similarly to the sensitivity analysis in Chapter 6.

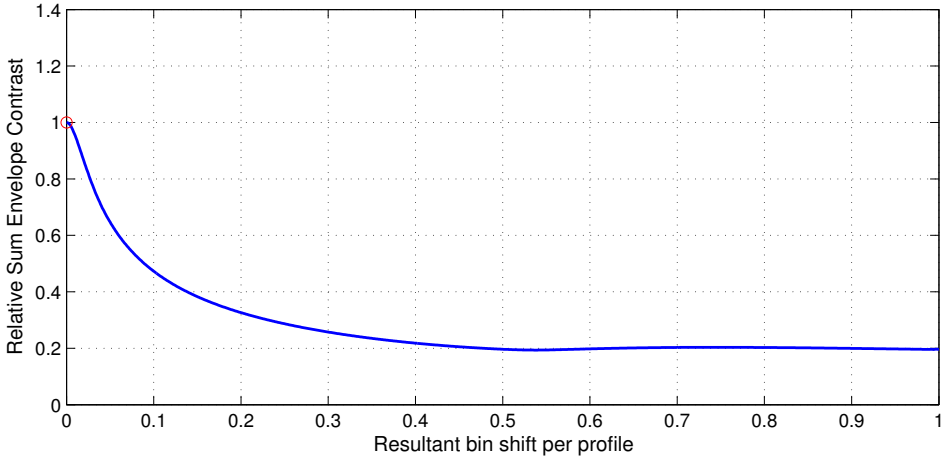

Figure I.1: The relative sum envelope contrast for envelopes shifted to simulate error accumulation.

Assuming no other factors are present that could affect the value of the sum envelope contrast, the trend of the quality measure indicates a decline until the resultant bin shift per profile value reaches 0.5 bins. For resultant bin shift profiles exceeding 0.5, the value of the sum envelope entropy settles to 20% of the optimal value.

This result indicates that if the error accumulation[1] effect if removed, the sum envelope contrast will increase by 80%.

Sum Envelope Entropy

The sum envelope entropy is influenced in a similar way to the sum envelope contrast, but increases in entropy indicate a decline in alignment quality.

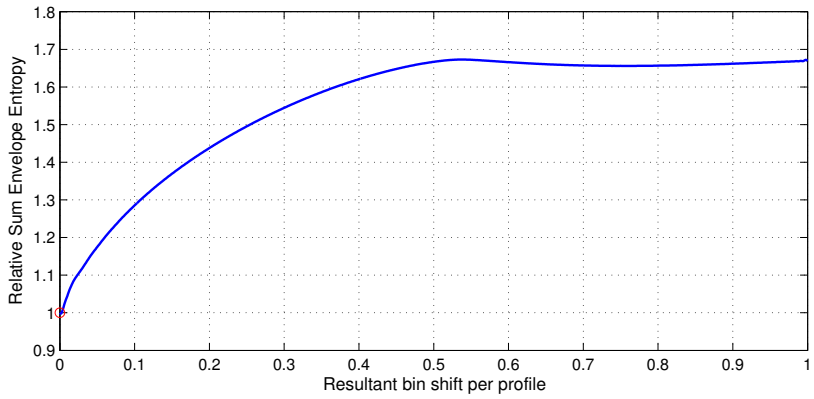

Figure I.2: The relative sum envelope entropy for envelopes shifted to simulate error accumulation.

The result in Figure I.2 indicate that a maximum decline in alignment quality, as measured by the sum envelope entropy, of 67% is encountered when the resultant range bin shifts due to error accumulation exceeds 0.5 bins. The maximum achievable improvement in sum envelope entropy when the effect of error accumulation is eliminated is 67%.

[1] Assuming linear misalignment not exceeding 1 range bin

Global Envelope Correlation

Larger values of the global envelope correlation is assumed to indicate superior alignment quality. The global envelope correlation for increasing severity of the effect of error accumulation appears in Figure I.3.

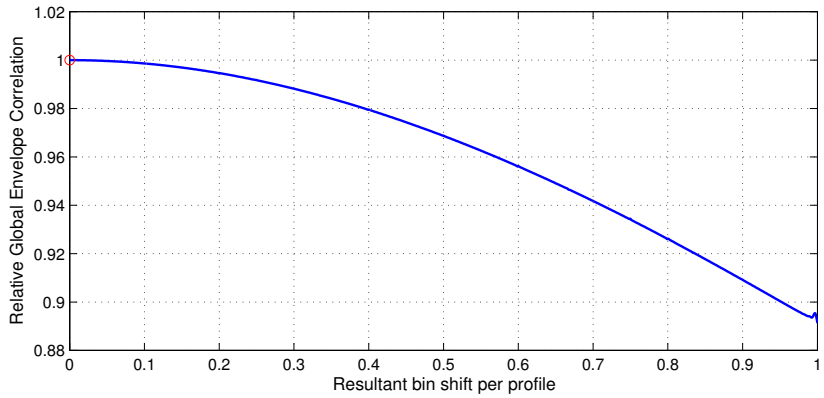

Figure I.3: The relative global envelope correlation for envelopes shifted to simulate error accumulation.

The global envelope correlation deteriorates slower than the sum envelope contrast and entropy previously considered. The maximum improvement in global envelope correlation achievable when the misalignment caused by error accumulation is eliminated, is around 11%.

Variance of the peak location

The variance in the peak location is very sensitive to the misalignment caused by the error accumulation effect. Results for the sensitivity analysis appear in Figure I.4.

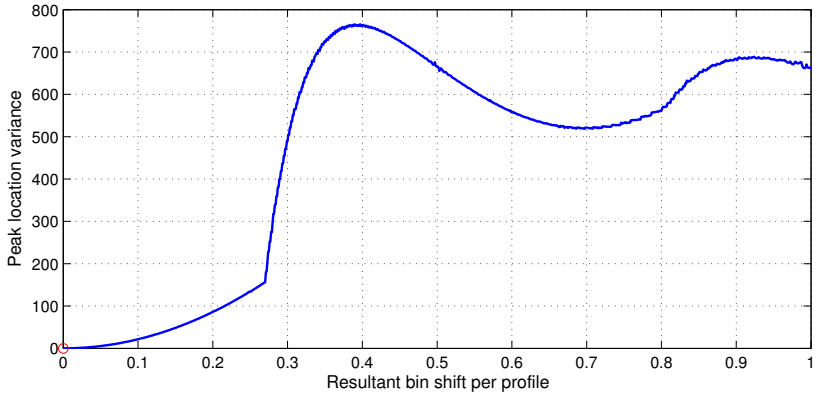

Figure I.4: The variance of the peak locations for envelopes shifted to simulate error accumulation.

The unusual transition in the peak variance position at 0.27 bin shifts can be attributed to the fact that this is the point at which the resultant bin shift causes wrapping of the dominant scatterer return from one range bin position to the position plus the total number of range bins per profile. Wrapping of dominant scatterer bin positions also appears in Figure 4.5, Chapter 4.

Envelope Mean Squared Difference

The influence of error accumulation on the envelope mean squared difference appears in Figure I.5.

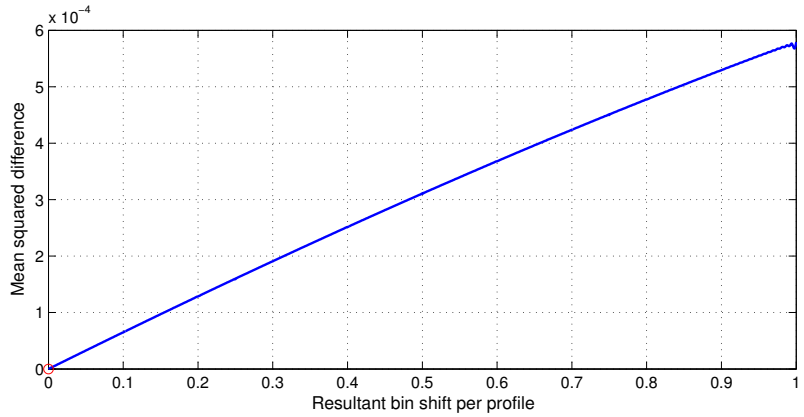

Figure I.5: The mean squared difference for envelopes shifted to simulate error accumulation.

The linear nature of the difference between adjacent profiles is translated into the linear nature of the envelope mean squared difference in data corrupted by error accumulation.

Burst Derivative

The influence of error accumulation on the burst derivative appears in Figure I.6.

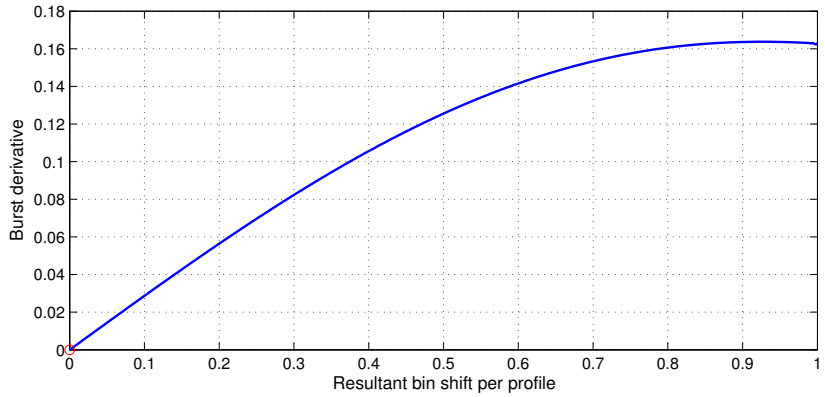

Figure I.6: The burst derivative for envelopes shifted to simulate error accumulation.

The burst derivative increases linearly with increased resultant bin shifts due to the error accumulation effect.

Appendix J

EBE Faculty: Assessment of Ethics in Research Projects

Any person planning to undertake research in the Faculty of Engineering and the Built Environment at the University of Cape Town is required to complete this form before collecting or analysing data. When completed it should be submitted to the supervisor (where applicable) and from there to the Head of Department. If any of the questions below have been answered YES, and the applicant is NOT a fourth year student, the Head should forward this form for approval by the Faculty EIR committee: submit to Ms Zulpha Geyer (Zulpha.Geyer@uct.ac.za; Chem Eng Building, Ph 021 650 4791). Students must include a copy of the completed form with the thesis when it is submitted for examination.

Name of Student:	**Vanessa Janse van Rensburg**
Department:	**Electrical Engineering**
Degree:	**M.Eng (Radar and Electronic Defence)**
Supervisors:	**Dr. Amit Mishra (UCT)**
	Willie Nel (CSIR)
Sponsorship:	**CSIR**
Research Project Title:	**High Range Resolution Profile Alignment**

Overview of ethics issues in your research project:.

Question 1: Is there a possibility that your research could cause harm to a third party (i.e. a person not involved in your project)?	YES	NO
Question 2: Is your research making use of human subjects as sources of data? If your answer is YES, please complete Addendum 2.	YES	NO
Question 3: Does your research involve the participation of or provision of services to communities? If your answer is YES, please complete Addendum 3.	YES	NO
Question 4: If your research is sponsored, is there any potential for conflicts of interest? If your answer is YES, please complete Addendum 4.	YES	NO

If you have answered YES to any of the above questions, please append a copy of your research proposal, as well as any interview schedules or questionnaires (Addendum 1) and please complete further addenda as appropriate.

I hereby undertake to carry out my research in such a way that

- there is no apparent legal objection to the nature or the method of research; and
- the research will not compromise staff or students or the other responsibilities of the University;
- the stated objective will be achieved, and the findings will have a high degree of validity;
- limitations and alternative interpretations will be considered;
- the findings could be subject to peer review and publicly available; and
- I will comply with the conventions of copyright and avoid any practice that would constitute plagiarism.

Signed by	Full name & Signature	Date
Student		

This application is approved by:

Supervisor (if applicable):		
HOD (or delegated nominee): Final authority for all assessments with NO to all questions and for all undergraduate research.		
Chair : Faculty EIR Committee For applicants other than undergraduate students who have answered YES to any of the above questions.		